ON THE USE OF HIGHER ORDER WAVEFORMS IN THE SEARCH FOR GRAVITATIONAL WAVES EMITTED BY COMPACT BINARY COALESCENCES

BY

DAVID J. A. MCKECHAN

A THESIS SUBMITTED IN PARTIAL FULFILLMENT FOR THE DEGREE OF

DOCTOR OF PHILOSOPHY
IN
PHYSICS

AT THE

SCHOOL OF PHYSICS AND ASTRONOMY
CARDIFF UNIVERSITY

APRIL 2010

ProQuest LLC
789 East Eisenhower Parkway
P.O. Box 1346
Ann Arbor, MI 48106-1346

'I ran a LIGO search for gravitational waves and all I got was a lousy chapter in my thesis...'

The Author.

DECLARATION OF AUTHORSHIP

- DECLARATION:
  This work has not previously been accepted in substance for any degree and is not concurrently submitted in candidature for any degree.

  Signed: .... (candidate) Date: 13/4/10

- STATEMENT 1:
  This thesis is being submitted in partial fulfillment of the requirements for the degree of Doctor of Philosophy (PhD).

  Signed: .... (candidate) Date: 13/4/10

- STATEMENT 2:
  This thesis is the result of my own independent work/investigation, except where otherwise stated. Other sources are acknowledged by explicit references.

  Signed: .... (candidate) Date: 13/4/10

- STATEMENT 3
  I hereby give consent for my thesis, if accepted, to be available for photocopying and for inter-library loan, and for the title and summary to be made available to outside organisations.

  Signed: .... (candidate) Date: 13/4/10

SUMMARY OF THESIS

Doctor of Philosophy
School of Physics and Astronomy
Cardiff University

On the use of higher order waveforms in the search for
gravitational waves emitted by compact binary coalescences

by David J. A. McKechan

This thesis concerns the use, in gravitational wave data analysis, of higher order waveform models of the gravitational radiation emitted by compact binary coalescences. We begin with an introductory chapter that includes an overview of the theory of general relativity, gravitational radiation and ground-based interferometric gravitational wave detectors. We then discuss, in Chapter 2, the gravitational waves emitted by compact binary coalescences, with an explanation of higher order waveforms and how they differ from leading order waveforms; we also introduce the post-Newtonian formalism. In Chapter 3 the method and results of a gravitational wave search for low mass compact binary coalescences using a subset of LIGO's 5th science run data are presented and in the subsequent chapter we examine how one could use higher order waveforms in such analyses. We follow the development of a *new* search algorithm that incorporates higher order waveforms with promising results for detection efficiency and parameter estimation. In Chapter 5, a new method of windowing time-domain waveforms that offers benefit to gravitational wave searches is presented. The final chapter covers the development of a game designed as an outreach project to raise public awareness and understanding of the search for gravitational waves.

ACKNOWLEDGEMENTS

I must begin by thanking my supervisor, Bangalore Sathyaprakash, for all of his considered advice, patience and directorship that has been of great benefit to me over the past three and a half years here at Cardiff. It has truly been a pleasure to work with Sathya and I am still unsure which is greater: his passion for gravitational waves and physics, or his knowledge. Both attributes are inspiring and I wish that there had been more time to hear Sathya talk with great enthusiasm about his favourite subjects.

I gratefully acknowledge those that have directly contributed to the projects presented in this thesis. I would first like to thank Chris Van Den Broeck, whom I regarded as my higher harmonics mentor; and Craig Robinson, who was always at hand to help me squash bugs in various analysis codes (not always mine). Both Chris and Craig were able to fill in the gaps of my mathematical knowledge and explain 'what Sathya meant' whenever I was confused (as I often was). I am grateful to Stephen Fairhurst, whom I have considered as my vice-supervisor, for his invaluable advice and insight, particularly regarding the 12-to-18 analysis. I also thank the 12-to-18 monthers who made it very easy for me to 'lead' the project and who all did such a great job: Collin Capano, Ian Harry, Chris, Lucia Santamaria, Michele Vallisneri, Sukanta Bose, Andrew Lundgren and Duncan Brown. Oh, and thanks for putting up with 'Dictator Dave'.

I have thoroughly enjoyed working with all the members of the Cardiff Gravitational Physics group, past and present. Thomas Cokelaer, Anand Sengupta, Jack Yu, Deepak Baskaran, Patrick Sutton, Leonid Grishchuk, Laura Nuttall, Thomas Dent, Duncan MacLeod, John Veitch, James Clark, Gerald Davies, Devanka Pathak, Alexander Dietz, Gareth Jones, Wen Zhao, Ioannis Kamaretsos, Mark Edwards, Valeriu Predoi, Chris, Craig, Ian, Steve and Sathya: thank you all for being easy to work with, willing to help whenever asked and for the interesting conversations (of varying sobriety) we have had over the years. Leo - thanks for never letting me believe I had any talent at football. I also acknowledge Louise Winter, Nicola Hunt, Philip Treadgold and all other staff in the school office for their friendly administrative support.

I wish to thank everyone in the CBC group for all their help. I am sure to forget a few names here, for which I apologise, but I would like to mention a few in particular who have helped me on various occasions: Alan Weinstein, Fredrique Marion, Gabriella Gonzales, Drew Keppel, Jessica Clayton, Ruslan Vaulin, Patrick Brady, Gianluca Guidi, Scott Koranda, Jolien Creighton, Nickolaus Fotopoulos, Marie Ann Bizourd, John Whelan, and Adam Mercer.

I am also grateful to the LSC, for permitting the use of LIGO S4 data, and to the STFC for my studentship (PPA/S/S/2006/4330).

On a personal level I thank my friends from home: Steve, Adam, Sarah, Jonny, Soph, Chris, Steve, Rob, Emily and Will. They may not realise it, but the times that we have shared during the holidays have just about preserved my sanity (particularly Christmas 2009). I also thank my family for all their support over the years, Nan, Wendy, Nigel; Laura and Paul for their helpful advice, even whilst busy looking after my baby niece Ella.

I am indebted to my beautiful girlfriend Amanda; for her unending love and support, especially over the past six months where I have done little but write this thesis, moan about writing this thesis, go running and complete job applications.

Finally, I dedicate this work to my parents who have given me everything.

COAUTHORED PAPERS

Sections of this thesis include collaborative work published in the following papers:

1. Chapter 3: *'Search for Gravitational Waves from Low Mass Compact Binary Coalescence* [sic] *in 186 Days of LIGO's fifth Science Run'* [1].

   The author analysed one month of data and was the corresponding author for the publication. The author also contributed to tuning the pipeline, the development of ihope and the ihope results page.

   DISCLAIMER: Although this chapter presents results previously published, the views expressed in the chapter are the author's own and are in no way endorsed by the LIGO Scientific Collaboration (LSC).

2. Chapter 5: *'A tapering window for time-domain templates and simulated signals in the detection of gravitational waves from coalescing compact binaries.'* [2].

   The author developed the implementation of the new window and conducted the majority of the corresponding studies.

3. Chapter 6: *'Black Hole Hunter: The game that lets YOU search for gravitational waves.'* [3].

   The author developed the code that produced the audio and image files used in the game.

Contents

List of figures

List of tables

List of acronyms

ACTD	Amplitude Corrected Time-Domain.
BBH	Binary black hole.
BNS	Binary neutron star.
NSBH	Neutron star-black hole binary.
CBC	Compact binary coalescence.
DAG	Direct acrylic graph.
DFT	Discrete Fourier transform.
EFE	Einstein Field Equations.
EOB	Effective one-body.
ET	Einstein Telescope.
FAR	False alarm rate.
FD	Frequency domain.
FBLO	First beyond leading order.
FLSO	Frequency of last stable orbit.
FT	Fourier transform.
FWF	Full waveform.
HIPE	Hierarchical Inspiral Pipeline Executable.
IFAR	Inverse false alarm rate.
IFO	Interferometer.
IFT	Inverse Fourier transform.
IMBBH	Intermediate mass binary black hole.
IMR	Inspiral-merger-ringdown.
ISCO	Innermost stable circular orbit.
LIGO	Laser Interferometic Gravitational-Wave Observatory.
LHS	Left hand side.
LSC	LIGO Scientific Collaboration.
PN	Post-Newtonian.
PSD	Power spectral density.

RWF	Restricted waveform.
S4	LIGO's 4th science run.
S5	LIGO's 5th science run.
S51YR	S5 first year.
SNR	Signal-to-noise ratio.
SPA	Stationary-phase approximation.
RHS	Right hand side.
TD	Time domain.
TT3	Taylor-T3.
VSR1	Virgo Science Run 1.

List of constants and variables

c	Speed of light in a vacuum.
G	Gravitational constant.
$M_\odot$	Mass of the Sun.
η	Symmetric mass ratio. (Also Minkowski metric in Chapter 1.)
$F_{+,\times}$	Detector response functions.
$\mathcal{M}$	Chirp mass.
ρ	Signal-to-noise ratio (SNR).
$S_n(f)$	Power spectral density.

Conventions

1. Unless stated otherwise, Greek indices run from $0, \ldots, 3$ and Latin indices from $1, \ldots, 3$.

2. The mass of the Sun is $M_\odot = 1.99 \times 10^{30}\,\mathrm{kg}$.

3. The speed of light is $c = 3 \times 10^8\,\mathrm{ms}^{-1}$.

4. Unless stated otherwise, natural units will be used where the gravitational constant and the speed of light are unity, i.e., $G = c = 1$.

5. Three component spatial vectors will be represented as bold and non-italic text, e.g.,
$$\mathbf{F} = m\mathbf{a}\,.$$

6. An overhead dot represents the derivative with respect to time, e.g.,
$$\mathbf{F} = m\mathbf{a} = m\frac{d\mathbf{v}}{dt} = m\dot{\mathbf{v}} = m\frac{d^2\mathbf{x}}{dt^2} = m\ddot{\mathbf{x}}\,.$$

7. The derivative is represented by a comma, e.g.,
$$A^{\nu}{}_{,\mu} = \frac{\partial A^{\nu}}{\partial x^{\mu}}\,.$$
and the covariant derivative is represented by a semi-colon, e.g.,
$$A^{\nu}{}_{;\mu} = \frac{\partial A^{\nu}}{\partial x^{\mu}} + \Gamma^{\nu}_{\mu\alpha}A^{\alpha}\,.$$
where $\Gamma^{\nu}_{\mu\alpha}$ is the Christoffel symbol.

8. The Einstein summation convention is used,
$$a_i x^i = \sum_i a_i x^i\,. \tag{1}$$

9. The expectation value is represented by an overline,

$$\overline{f(x)} = \int f(x)P(x)dx\,, \tag{2}$$

where $P(x)$ is the probability density function.

10. The abbreviation for the full waveform (FWF) refers to any post-Newtonian (PN) waveform that is greater than 0PN in amplitude. For instance a waveform that is 0.5PN in amplitude and 2PN in phase may still be referred to as the FWF. Where the amplitude order is specified it is written in brackets, e.g., a waveform at 2PN in amplitude will be written as FWF (2PN). N.B.: this does not necessarily indicate the phase order.

11. The LIGO interferometers are denoted by their location, H for Hanford and L for Livingston; and by their arm length, 1 for 4 km and 2 for 2 km. The initial LIGO configuration consisted of two interferometers at Hanford, H1 and H2 and a single interferometer at Livingston, L1. Data collected by all three detectors were called triple time or H1H2L1 time, alternatively there were the double times, H1L1 and H2L1, when only one of the Hanford interferometers was operating [1]. Triggers that are coincident between the sites may be labelled in the same manner, e.g., a trigger coincident between H1 and L1 during triple time could be described as an H1L1 trigger in H1H2L1 time.

---

[1] H1H2 double time data are not considered.

For Mum and Dad.

Prologue

Nicolaus Copernicus was the first to develop a thorough and detailed Heliocentric theory of the Universe, with the Sun at the centre and, perhaps more importantly, the Earth in orbit around the Sun. Observation and appreciation of celestial mechanics was the first step on the path towards understanding gravity.

Just 200 years later Kepler had developed his laws of planetary motion and Newton, in turn, his universal law of gravitation. In a short time gravity had developed from insignificance to a simple inverse-square law, explaining the motion of all the stars and all the planets, and why objects fall to the Earth...nearly.

Another 200 years later, Einstein completed his theory of general relativity. With the advent of relativity, gravitational field information, like everything else, was bound to the universal speed limit of light. Thereafter, any theory of gravity obeying the principles of special relativity, was obliged to permit gravitational waves.

Today, approaching the centenary of general relativity, we are on the cusp of direct gravitational wave detection that will open a new window from which to view the Universe, illuminating our understanding.

Chapter 1

Introduction

We begin with an introduction to relativity that gently introduces the fundamental concepts and an idea of curved spacetime before quickly progressing on to the theory of gravitational waves by understanding how they propagate and interact with free particles. The chapter concludes with an overview of ground-based interferometric detection of gravitational waves with an introduction to the LIGO detectors and their operation.

1.1 A very brief course in relativity

1.1.1 The Principle of relativity

The *principle of relativity* is the simple requirement that the *the laws of physics are the same in every inertial frame.* A passenger inside a train moving at a constant velocity can perform no experiment to determine the *absolute* speed of the train, measuring the same physical constants etc., as his or her companion waiting at rest on the station platform. Under Newtonian physics their frames of reference are related by a *Galilean transformation*, which applies to the spatial dimensions with both observers measuring the same *absolute time.* However, Galilean transformations do not work when applied to light emitted from objects moving relative to one another. When doubts of the existence of a luminiferous aether arose, it became clear that Galilean transformations were not entirely consistent with the principle of relativity.

Einstein abandoned the concept of absolute time. He introduced a second postulate to the principle of relativity, that *the speed of light is the same in all inertial reference* *frames regardless of their relative motion.* In fact if Maxwell's equations, which reveal the nature of light as electromagnetic radiation, are the same in all inertial frames, then the second postulate is implied by the principle of relativity regardless. Einstein had developed his theory of *special relativity*, where the coordinates of two inertial frames are related by a *Lorentz transformation*, which applies to the three spatial coordinates *and* the time-coordinate.

From this simple construct, all the popular wonders of special relativity arise: time-dilation, length-contraction and mass-energy equivalence. However, special relativity does not account for non-inertial frames of reference, i.e., it can not be applied in an accelerating frame[1]. Furthermore, Newton's law of gravity is not consistent with special relativity.

The *general* principle of relativity requires that *the laws of physics are the same in all reference frames* - both inertial and non-inertial - and forms the basis of Einstein's theory of *general relativity*, a theory of gravity that is consistent with special relativity.

1.1.2 Tidal forces and the curvature of spacetime

An astonishing coincidence of nature is the equivalence of gravitational and inertial mass, i.e., the property of matter that determines the force an object experiences due to gravity is the same property that determines its resistance to an applied external force. Einstein realised that a person at rest on the Earth's surface, where the gravitational acceleration is $\mathbf{g}_E$, is indistinguishable from another person, inside a spaceship accelerating at $\mathbf{a} = \mathbf{g}_E$, far away from any gravitational field. Moreover, a person in free-fall, over a *short-period of time*, is equivalent to another in a spaceship, also far away from any gravitational field, but undergoing no acceleration. Thus the equivalence principle is defined: *In a freely falling laboratory, in a small region of spacetime, the laws of physics are those of special relativity.*

Consider a pair of identical sky-diving twins, who have jumped simultaneously from a plane using doors on either side of an aircraft and who are now in free-fall. Initially, they are at the same distance from the centre of the Earth, but separated by a short horizontal distance. As each twin is falling on a path that extends radially from the centre of the Earth, they will gradually drift towards each other. Had they jumped one after the other, so that they were separated by a short vertical distance, the first twin to jump would undergo a slightly stronger acceleration and their vertical separation would

---

[1] Accelerating frames can be studied in special relativity by using an *instantaneous rest frame.*

gradually increase. The effect on the twins' horizontal or vertical separation is tidal acceleration; due to a non-uniform gravitational field which gives the *tidal force.*

Einstein concluded that an object in free fall is *not* subjected to a gravitational force, i.e., although the sky divers' horizontal separation decreases, there is no horizontal force acting upon them. Rather, spacetime is curved due to the Earth's mass and energy - the sky divers are instead following separate *geodesic* paths, the 'straight lines' of a curved space.

1.1.3 The geometry of spacetime and the Einstein Field Equations

In relativity, the geometry of spacetime is defined as a pseudo-Riemannian manifold. In special relativity the interval, ds^2, between two events on the spacetime manifold is given by the Minkowski metric, η, where

$$ds^2 = \eta_{\mu\nu} dx^\mu dx^\nu \,, \tag{1.1}$$

$$x^\mu = (t, x, y, z) \,, \tag{1.2}$$

and

$$\eta_{\mu\nu} = \begin{pmatrix} -1 & 0 & 0 & 0 \\ 0 & 1 & 0 & 0 \\ 0 & 0 & 1 & 0 \\ 0 & 0 & 0 & 1 \end{pmatrix} . \tag{1.3}$$

If the Minkowski metric is that of flat spacetime geometry, then in general relativity the interval between two events in spacetime is defined by a general metric, g,

$$ds^2 = g_{\mu\nu} dx^\mu dx^\nu \,. \tag{1.4}$$

The metric g contains the information about the curvature of spacetime. Our sky diving twins are experiencing a tidal force, their horizontal separation is decreasing. Under gravitational free-fall, both are following geodesic paths that were initially parallel to each other but are converging due to the curvature of spacetime. The curvature is quantified by the Riemann tensor, $R^\mu{}_{\nu\rho\sigma}$. The Riemann tensor is defined entirely by the spacetime metric and its first and second derivatives; it is equal to zero in a flat spacetime.

Einstein linked the curvature of spacetime to the energy-momentum tensor, $T_{\mu\nu}$, which contains the momentum and energy densities and their fluxes in a region of spacetime (see A.1), in the form of ten second order PDEs known as the Einstein Field Equations (EFE)[2],

$$G_{\mu\nu} = R_{\mu\nu} - \frac{1}{2} g_{\mu\nu} R = \kappa T_{\mu\nu}\,, \tag{1.5}$$

where

$$R_{\mu\nu} = R^{\alpha}{}_{\mu\alpha\nu}\,, \tag{1.6}$$

$$R = R^{\mu}{}_{\mu}\,, \tag{1.7}$$

and

$$\kappa = \frac{8\pi G}{c^2}. \tag{1.8}$$

The EFE have the important properties that:

- energy and momentum are conserved,

$$T^{\mu\nu}{}_{;\mu} = 0\,; \tag{1.9}$$

- Newtonian gravity is recovered in the correct limits, i.e., where $v \ll 1$ and the internal stresses are small;
- they are tensor equations and are manifestly *invariant* under coordinate transformations!

1.2 The weak field approximation

The EFE are difficult, if not impossible, to solve in all but the most simple of situations. One approach is that of the weak field approximation where the spacetime metric is expressed simply as Minkowski spacetime plus a small perturbation,

$$g_{\mu\nu} = \eta_{\mu\nu} + h_{\mu\nu}\,, \tag{1.10}$$

where

$$|h_{\mu\nu}| \ll 1\,. \tag{1.11}$$

As the perturbation $h_{\mu\nu}$ and its derivatives are very small, one can retain only their first order terms, i.e., terms *linear* in $h_{\mu\nu}$ and $\partial h_{\mu\nu}$. In doing so, the Riemann tensor takes the simple form,

$$R_{\mu\nu\rho\sigma} = \frac{1}{2}\left(h_{\mu\sigma,\nu\rho} + h_{\nu\rho,\mu\sigma} - h_{\mu\rho,\nu\sigma} - h_{\nu\sigma,\mu\rho}\right)\,. \tag{1.12}$$

---

[2] Rather than sixteen equations due to the symmetry of the metric tensor and $R_{\mu\nu}$.

Thus we will obtain the *linearised* EFE by substituting (1.10) and (1.12) in (1.5). Before doing so we should recall that in general relativity we are free to make any coordinate transformation that we wish. Interestingly, it can be shown that under a *small* coordinate transformation the metric can remain unchanged. Given that

$$g'_{\mu\nu} = \frac{\partial x^\rho}{\partial x'^\mu}\frac{\partial x^\sigma}{\partial x'^\nu} g_{\rho\sigma}\,, \tag{1.13}$$

and

$$x'^\mu = x^\mu + \epsilon^\alpha\ , \tag{1.14}$$

the metric (1.10) will transform as

$$\begin{aligned} g'_{\mu\nu} &= \frac{\partial x^\rho}{\partial x'^\mu}\frac{\partial x^\sigma}{\partial x'^\nu}\left[\eta_{\rho\sigma} + h_{\rho\sigma}\right]\ , &(1.15a)\\ &= \eta_{\mu\nu} + \frac{\partial x^\rho}{\partial x'^\mu}\frac{\partial x^\sigma}{\partial x'^\nu} h_{\rho\sigma}\,, &(1.15b)\\ &= \eta_{\mu\nu} + h_{\mu\nu} - \epsilon_{\mu,\nu} - \epsilon_{\nu,\mu}\,. &(1.15c)\end{aligned}$$

Hence the coordinate transformation simply re-defines the metric perturbation, $h_{\mu\nu} \rightarrow h_{\mu\nu}^{(\mathrm{new})}$. Provided the weak field condition is still met, $|h_{\mu\nu}^{(\mathrm{new})}| \ll 1$, one can make any coordinate transformation; such changes are known as gauge transformations. The freedom to choose any gauge allows us to greatly simplify the EFE.

The *trace-reverse* of the perturbation $h_{\mu\nu}$ is defined as

$$\bar{h}_{\mu\nu} = h_{\mu\nu} - \frac{1}{2}\eta_{\mu\nu}h^\alpha{}_\alpha\,. \tag{1.16}$$

If we make use of the trace-reverse of $h_{\mu\nu}$ and choose the Lorentz gauge condition,

$$\partial^\mu \bar{h}_{\mu\nu} = 0\,, \tag{1.17}$$

we find the linearised EFE can be written elegantly as

$$\Box\bar{h}_{\mu\nu} = -2\kappa T_{\mu\nu}\,. \tag{1.18}$$

1.3 Gravitational waves

1.3.1 Vacua solutions to the linearised EFE

In vacua, (1.18) reduces to

$$\Box\bar{h}_{\mu\nu} = 0\,, \tag{1.19}$$

which is a wave equation with solutions that are superpositions of plane waves of the form

$$\bar{h}_{\mu\nu} = A_{\mu\nu} \exp\left(ik_\alpha x^\alpha\right) , \tag{1.20}$$

where the equality

$$A_{\mu\nu} k^\nu = 0 , \tag{1.21}$$

must always be true to satisfy (1.17).

Let us pause for reflection here, we now understand that the perturbation of the spacetime metric, h, i.e., the gravitational field, propagates through empty spacetime as a *gravitational wave.*

The gravitational wave vector, k^α, where the wave is of frequency, ω, may be written as

$$k^\alpha = (\omega, \mathbf{k}) . \tag{1.22}$$

The magnitude of k^α is

$$k^2 = -\omega^2 + \mathbf{k}^2 . \tag{1.23}$$

The EFE imply that k^α is null, i.e., $|k|^2 = 0$. Therefore,

$$\omega = |\mathbf{k}| . \tag{1.24}$$

Recall that the general wave-vector $k = \omega/v$, therefore $v = 1 = c$ and thus gravitational waves propagate at the speed of light. Furthermore, in satisfying the Lorentz gauge condition, we conclude that the amplitude matrix, $A_{\mu\nu}$, is orthogonal to the wave vector and, therefore, gravitational waves are *transverse.*

1.3.2 The transverse-traceless gauge

Before we imposed the gauge conditions (1.17), the linear EFE consisted of ten equations, afterwards there were six. The linearised EFE are further reduced to just two equations with the *additional* choice of gauge conditions

$$\bar{h}_{0\mu} = 0 , \tag{1.25a}$$

$$\bar{h}^\alpha{}_\alpha = 0 , \tag{1.25b}$$

known as the *transverse-traceless* gauge conditions. From here on we shall indicate the transverse-traceless gauge with the superscript TT and make use of the fact that under these gauge conditions $\bar{h}^{TT}_{\mu\nu} = h^{TT}_{\mu\nu}$.

With the conditions that $h^{TT}_{\mu\nu}$ is symmetric and traceless the EFE reduce to just two components. A gravitational wave propagating in the z-direction takes the form

$$h^{TT}_{\mu\nu} = \begin{pmatrix} 0 & 0 & 0 & 0 \\ 0 & h_+ & h_\times & 0 \\ 0 & h_\times & -h_+ & 0 \\ 0 & 0 & 0 & 0 \end{pmatrix}, \tag{1.26}$$

where

$$h_+ = A^{TT}_{xx} \exp\left(ik_\alpha x^\alpha\right) \tag{1.27}$$

and

$$h_\times = A^{TT}_{xy} \exp\left(ik_\alpha x^\alpha\right) . \tag{1.28}$$

The two degrees of freedom, h_+ and $h_\times$, are known as the *plus* (+) and *cross* (×) polarisations respectively. A gravitational wave in this gauge could consist of either polarisation alone or a combination of the two.

One can now write the *time-dependent* weak field metric as

$$g_{\mu\nu} = \begin{pmatrix} -1 & 0 & 0 & 0 \\ 0 & 1 + h_+(t) & h_\times(t) & 0 \\ 0 & h_\times(t) & 1 - h_+(t) & 0 \\ 0 & 0 & 0 & 1 \end{pmatrix}. \tag{1.29}$$

Throughout this chapter we shall continue to consider gravitational waves propagating in the z-direction with respect to our chosen coordinates.

1.3.3 Effect of gravitational waves on a free particle

The motion of a test particle[3] initially at rest in our chosen coordinates is given by the geodesic equation. It can be shown that in the *TT* gauge, the effect of a passing gravitational wave will not change the particle's four-velocity, i.e., it will remain at rest. Thus in our coordinates, particles do not move due to a passing gravitational wave. However, the *proper distance*, L_x, between a particle at the origin and another at $x = L_0$ is given by

$$L_x = \int_0^{L_0} \sqrt{g_{xx} dx^2}, \tag{1.30}$$

---

[3] A small particle of negligible mass free from any external forces.

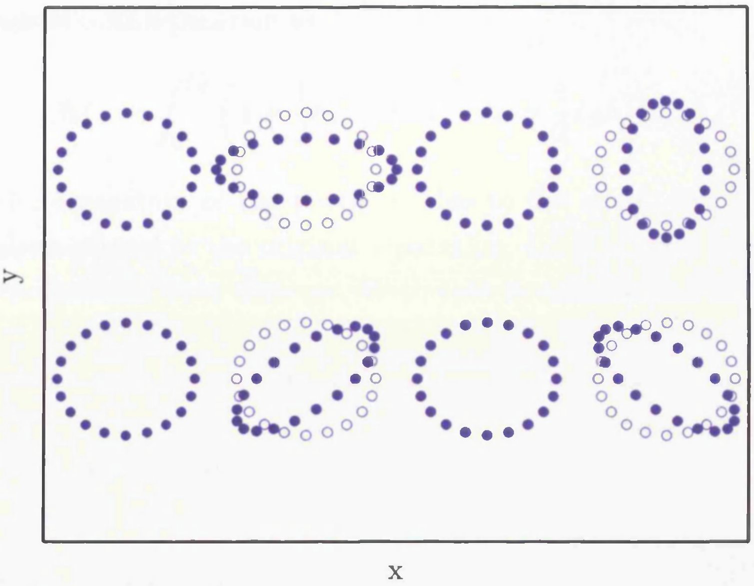

FIGURE 1.1: The displacement of a ring of test particles due to a + polarised gravitational wave (top) and a × polarised gravitational wave (bottom). The two polarisations are related by a 45° rotation. From left to right we see the $0, \pi/2, \pi, 3\pi/2$ phases of the gravitational wave, respectively. The empty circles represent the original separation of the particles.

which is *time-dependent* when a gravitational wave passes, e.g., if the wave is propagating in the z-direction, as given in (1.29), we have

$$L_x(t) = \int_0^{L_0} \sqrt{(1 + h_+(t))\, dx^2}\,. \tag{1.31}$$

Hence the effect of a passing gravitational wave can be seen by observing the change in proper distance between two test particles. Figure 1.1 shows the effect of a passing gravitational wave on a ring of particles for both polarisations. The particles experience a time-dependent tidal force. One can quantify the effect of a passing gravitational wave by comparing the original separation of the particles with the new separation.

Returning to the case of a particle at the origin and another at $x = L_0$ we can calculate the change in length, ΔL_x, due to the metric perturbation

$$\Delta L_x = L_x(t) - L_0 = \int_0^{L_0} \sqrt{1 + h_+(t)} dx - L_0\,. \tag{1.32}$$

Using the binomial expansion of the square root and keeping only first order terms, we rewrite the instantaneous separation as

$$\Delta L_x = \int_0^{L_0} \left(1 + \frac{1}{2}h_+(t)\right) dx - L_0 = \frac{1}{2}L_0 h_+(t)\,. \tag{1.33}$$

The fact that the separation of the particles, due to the effect of a passing gravitational wave, is proportional to the original separation, L_0, is of great importance when considering a gravitational wave detector. With that in mind we can rewrite (1.33) as

$$h_+ = 2\frac{\Delta L_x}{L_0}\,, \tag{1.34}$$

where we refer to h_+ as the *gravitational wave strain.*

1.3.4 Sources of gravitational waves

The generation of gravitational waves is understood by finding a general solution to (1.18) and will be discussed in appropriate detail in Chapter 2, where we will pay close attention to gravitational waves radiated by compact binary coalescences (CBCs).

The solution reveals that gravitational waves are *quadrupolar* in nature and are generated when a mass accelerates in a non-spherically symmetric manner, e.g., an inwards-spiralling binary system (inspiral) or a spinning non-axisymmetric neutron star. Other potential sources of gravitational waves include supernovae, progenitors of gamma ray bursts, flaring magnetars, pulsars glitches and a stochastic background composed of many overlapping signals from the distant Universe as well as primordial gravitational waves generated in the early Universe.

In principle, one could generate gravitational waves in the laboratory, for instance by rotating a dumb-bell which will have similar characteristics to a binary. However, even if the impracticalities of detection are neglected, the gravitational wave strain from such sources would be far too small ever to be measured [4].

1.3.5 Indirect evidence of gravitational waves

Observations of binary systems consisting of at least one pulsar provide conclusive evidence of the emission of gravitational radiation in accordance with general relativity. The most famous of these is PSR B1913+16, consisting of one pulsar with a companion neutron star. The pulsar allows for accurate measurements of the motion of the two objects, in particular the timing of the orbital period. General relativity predicts that the system will emit rotational energy of the system as gravitational radiation, causing the orbital separation and period to decrease. Observations of the binary system over nearly 40 years have shown that the evolution of the orbital period has matched that predicted by general relativity to remarkable accuracy. Hulse and Taylor, who first observed the system, were duly awarded the 1993 Nobel prize in Physics for their discovery which, for the first time, enabled general relativity to be tested in the strong field dissipative regime [5].

The gravitational waves emitted by PSR B1913+16 cannot currently be detected directly as they are very small in amplitude and are also of the wrong frequency to be detected by ground based detectors. As the binary evolves and the separation between the stars decreases, the gravitational radiation will increase in frequency and amplitude, but is not likely to be to be detectable for another three-hundred million years when the components will coalesce.

1.3.6 Direct detection of gravitational waves

To date gravitational waves have not been detected directly. Efforts began in the 1960s with resonant bar detectors, the sensitivity of which has now been surpassed by ground-based interferometric detectors [6, 7], which we will discuss below. In the future, we can look forward to space-based detectors [8, 9] that are free from some of the noise sources that inhibit ground-based experiments. Another possibility is the use of accurate pulsar timing arrays [10, 11], that could measure fluctuations, due to a passing gravitational wave, in the timings of a known set of millisecond pulsars.

1.4 Interferometric gravitational wave detectors

The concept of an interferometric detector is simple. Suppose we have an interferometer (IFO) with arms of length L_0, such that a beam splitter sends half the light from a monochromatic laser along an arm aligned with the x-axis and half along an arm aligned with the y-axis. The two beams will be reflected by the end-mirrors at coordinates $x = L_0$ and $y = L_0$, respectively, before being superposed upon returning to the beam splitter. If the mirrors are suspended such that they are freely falling, i.e., free from all external forces other than 'gravity', they will behave with respect to the origin in the same manner as the test particles shown in Figure 1.1. When a gravitational wave passes, the separation between the mirrors and the beam splitter will vary, which can be measured.

We quantify the light travel time along each arm of the interferometer using the null interval. For the x-axis we have

$$ds^2 = 0 = -dt^2 + (1 + h_+)dx^2 \,. \tag{1.35}$$

The time, τ_{x1}, of light travel along the x-axis from the beam splitter to the mirror is, therefore,

$$\int_0^{\tau_{x1}} dt \approx \int_0^{L_0} \left(1 + \frac{1}{2}h_+\right) dx = L_0 + \Delta L \,, \tag{1.36}$$

where ΔL is given by (1.33). The return time, τ_{x2}, is found by swapping the limits of integration in (1.36) and noting that the velocity is now in the negative x-direction (or, more simply, multiplying by 2), which gives a total light travel time of

$$\tau_x = 2L_0 + 2\Delta L \,. \tag{1.37}$$

Similarly, for the arm aligned with the y-axis we have a travel time

$$\tau_y = 2L_0 - 2\Delta L \,. \tag{1.38}$$

In the absence of a gravitational wave ($h_+ = 0$ and $\Delta L = 0$), the difference in the travel times between the two arms is $\Delta\tau = 0$. However, in the presence of a gravitational wave[4], the difference is

$$\Delta\tau = 4\Delta L \,. \tag{1.39}$$

Alternatively, written as the phase-shift of the laser light returning to the beam splitter:

$$\Delta\phi(t) = 4\Delta L(t)\frac{2\pi}{\lambda} = \frac{4\pi}{\lambda}L_0 h_+(t) \,, \tag{1.40}$$

where λ is the wavelength of the laser. Thus the passing of a gravitational wave may be observed by measuring the phase shift between the light beams when they are superposed at the beam splitter.

1.4.1 Sensitivity

Supposing the minimum phase difference one can measure is 10^{-9}; using laser light of wavelength 500 nm and an IFO of 4 km in length, we find the minimum gravitational wave strain measurable to be $\sim 10^{-20}$. To reach a minimum strain of $\sim 10^{-22}$, the IFO would need to be one hundred times longer. However, an effective extension in the arm

---

[4] Assuming h_+ is constant for the period of the round trip.

length can be achieved by using *Fabry-Perot* cavities that *fold* the light, i.e., reflect the light up and down the arm multiple times before it is superposed at the beam splitter.

In Section 2.3 we will estimate the gravitational wave strain that is measurable on Earth, due to gravitational radiation emitted by CBCs in the nearby Universe and see that it is greater than $\sim 10^{-22}$.

1.4.2 Antenna response functions

Thus far we have considered a gravitational wave travelling in the z-direction with the detector arms aligned with the x- and y-axes. In general, the gravitational wave strain in a detector will be a linear combination of each polarisation multiplied by the *antennae response* functions, F_+ and $F_\times$, such that

$$h(t) = F_+ h_+(t) + F_\times h_\times(t)\,. \tag{1.41}$$

The antenna response functions depend upon the orientation of the source with respect to the detector, namely the three sky angles θ, ϕ and ψ (see Figure 1.2):

$$F_+(\theta,\phi,\psi) = \frac{1}{2}\cos 2\psi \left(1+\cos^2\theta\right)\cos 2\phi - \sin 2\psi \cos\theta \sin 2\phi\,, \tag{1.42}$$

$$F_\times(\theta,\phi,\psi) = \frac{1}{2}\sin 2\psi \left(1+\cos^2\theta\right)\cos 2\phi - \cos 2\psi \cos\theta \sin 2\phi\,. \tag{1.43}$$

The angles θ and ϕ give the location of the source, where $\theta + \pi$ is the angle between the detector's zenith and the propagation direction of the gravitational wave, z', and ϕ is the azimuth angle between the detector's x-axis and the projection of z' in the x-y plane. Finally, ψ is the *polarisation* angle, which is the angle between the detector's zenith projected on the sky and x'.

1.4.3 Sources of noise

A noise source in an IFO detector is any process other than a passing gravitational wave that causes a change in the measured phase offset (1.40). There are four main sources of noise:

Seismic noise Mechanical vibrations of the mirrors (the test masses), will occur due to seismic activity that could be caused by anything from an earthquake, to the wind or a passing train. Seismic noise is typically of a low frequency and is the dominant source

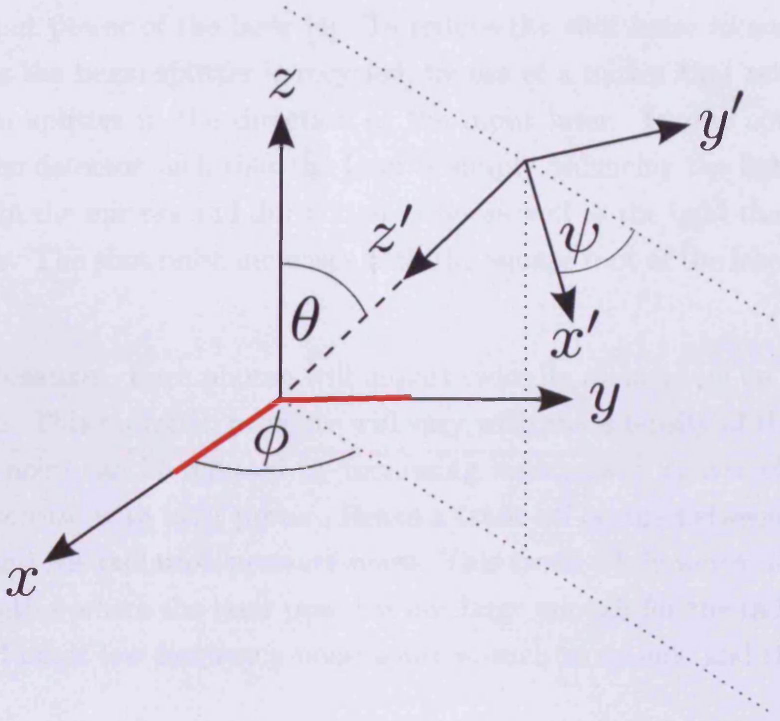

FIGURE 1.2: The sky angles θ, ϕ and ψ, between an IFO (located at the origin of the unprimed coordinates and aligned with the x-y axes) and a gravitational wave propagating in the z' direction in the TT gauge.

of noise below 40 Hz [4]. The seismic noise may be reduced by isolating the test masses using suspension systems, but becomes technically challenging, if not impossible, below ~ 1 Hz.

Thermal noise The test masses and their suspension systems will vibrate due to their thermal energy. The strain[5] induced in a detector due to thermal vibrations decreases linearly with the natural logarithm of the frequency and dominates the noise budget between 40-200 Hz [4]. Ideally, the resonant frequency of the detector materials will be outside the frequency range of interest (the gravitational wave frequency) and will have a high Q-value. Thermal noise can also be reduced by designing a cryogenic detector, e.g., LCGT [12], although detectors typically operate at ambient temperature.

Shot noise The number of photons returning from each arm of an IFO is Poisson distributed with a mean value, N, and standard deviation, $\sqrt{N}$. Fluctuations in the number of photons limits the minimum possible $\Delta\phi$ that can be measured as it appears identical to a fluctuation in phase, since the phase is estimated by measuring output power. It follows that the shot noise is inversely proportional to $\sqrt{N}$, or the square

---

[5] In units of $1/\sqrt{\text{Hz}}$.

root of the input power of the laser [4]. To reduce the shot noise to acceptable levels, light that exits the beam splitter is recycled, by use of a mirror that returns light that exits the beam splitter in the direction of the input laser. In due course the power builds up in the detector such that the laser is simply balancing the light losses due to imperfections in the mirrors and diffraction losses as well as the light that exits towards the photodiode. The shot noise increases with the square root of the laser frequency [4].

Radiation pressure Each photon will impart twice its momentum on the test masses upon reflection. This radiation pressure will vary with the intensity of the photons and, although shot noise can be reduced by increasing laser power, conversely the intensity fluctuations *increase* with laser power. Hence a trade-off occurs between improvements in shot noise and the radiation pressure noise. This trade-off, however, is not a concern for initial detectors where the laser power is not large enough for the radiation pressure noise to exceed other low frequency noise sources, such as seismic and thermal.

1.5 Operation of LIGO

The initial operation of the Laser Interferometic Gravitational-Wave Observatory (LIGO) consisted of three interferometric detectors at two sites: Hanford, WA and Livingston, LA. Each site had a 4 km IFO, but there was a second 2 km IFO at Hanford co-aligned with the 4 km detector. Indeed, the 4 km IFOs are still operating as part of Enhanced LIGO [13]. Here we shall consider one of the 4 km detectors.

Figure 1.3[6] shows a simplified layout of the LIGO optics including the Fabry-Perot cavities and power recycling mirror that were discussed above. The Fabry-Perot cavities increase the LIGO optical path length by a factor of approximately 100. Thus sensitivities of 10^{-22} can be achieved, as can be seen in Figure 1.4, which shows the design strain amplitude spectrum, i.e., the total noise, of the LIGO design [7].

1.5.1 Feedback control system - data calibration

When collecting data, the LIGO detector is configured such that the superposition of the light from each arm gives approximately null output at the photodiode. So that the detector can collect data continuously, it is kept in stable operation by use of a feedback system. The signal output at the photodiode is returned back into the Fabry-Perot

---

[6] Figure 1.3 was produced using svg files originally created by Alexander Franzen.

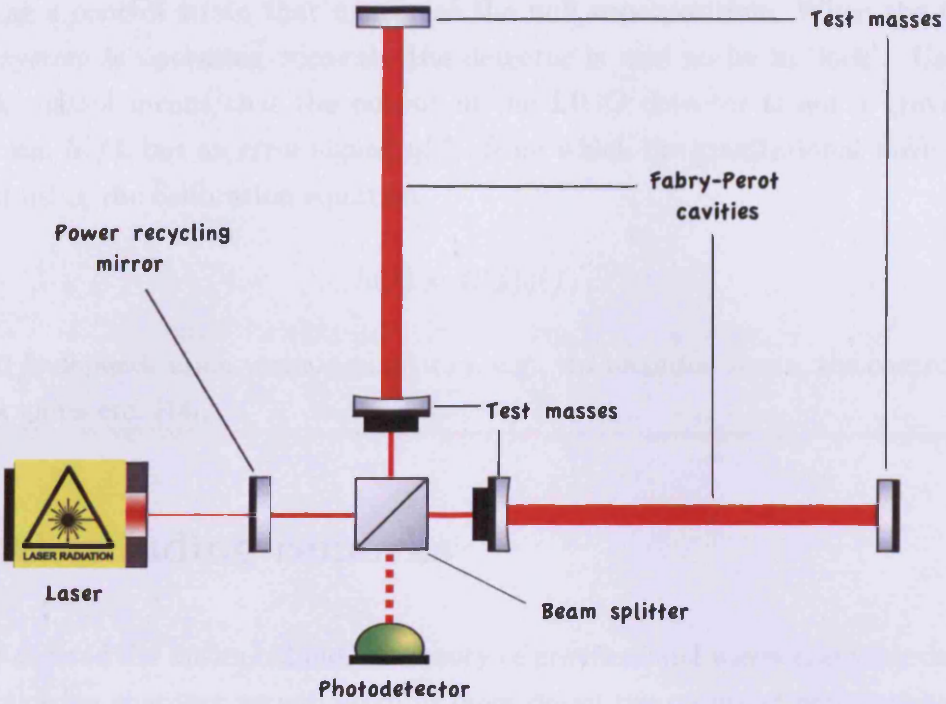

FIGURE 1.3: A simplified schematic of the LIGO optical layout (not to scale). The Fabry-Perot cavities are 4km long.

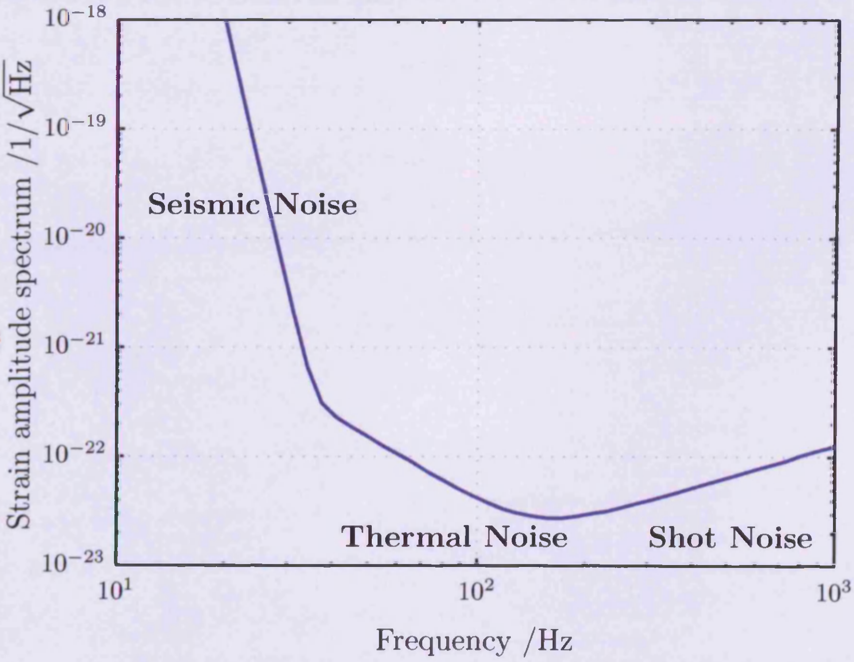

FIGURE 1.4: The design noise spectrum for LIGO 4km detectors shown as the strain in units of $1/\sqrt{\mathrm{Hz}}$. Seismic noise dominates the lower frequency range, whilst shot noise dominates the high frequency range. The frequency range of between 40 – 200Hz is dominated by thermal noise.

cavities as a control strain that maintains the null superposition. When the feedback control system is operating correctly the detector is said to be in 'lock'. Use of the feedback control means that the output of the LIGO detector is not a gravitational wave strain, $h(f)$, but an error signal, $q(f)$, from which the gravitational wave strain is obtained using the calibration equation

$$h(f) = R(f)q(f)\,, \tag{1.44}$$

where $R(f)$ depends upon various quantities, e.g., the recorded strain, the control strain, feedback gains etc. [14].

1.6 Concluding remarks

We have covered the basics behind the theory of gravitational waves and their detection. In the following chapters we will learn in more detail the nature of gravitational waves emitted by CBCs and how a search for gravitational waves using LIGO data is performed. During its fifth science run, LIGO collected data of unprecedented sensitivity and bandwidth. The results of a search for gravitational waves from low mass CBCs in a subset of LIGO's 5th science run (S5) data are presented in Chapter 3.

Chapter 2

Gravitational waves radiated from binary systems

In this chapter we study the nature of gravitational waves radiated by compact binary coalescences (CBCs), i.e., binary systems consisting of neutron stars or black holes that lose energy via gravitational wave emission, until the objects eventually merge. We consider *compact* objects, rather than say main-sequence stars, as they can be treated as point particles. Specifically, they need to be compact enough so that their surfaces are not touching when their orbital frequency is in the range of interest for detection.

We begin by finding a general solution to the linearised EFE before proceeding to the dynamics of a binary system and discussing the post-Newtonian (PN) formalism used to characterise the waveforms emitted by such objects.

N.B.: in this chapter we will closely follow the derivations of Maggiore [15].

2.1 The general solution to the linearised EFE

The linearised EFE can be solved by the method of Green's function, where the solution will depend upon the appropriate choice of boundary conditions. We recall the Lorentz gauge condition (1.17), that energy and momentum are conserved and choose the boundary condition that there is no-incoming radiation, i.e., the system that we are studying is isolated from all other bodies in the Universe. Under such conditions we use the *retarded* Green's function to solve (1.18). Since we are interested in the solutions at a distance $r \sim \infty$, i.e., in the far zone where the weak field equations are valid, we can write the solution as it is when transformed into the *TT* gauge via the Lambda tensor, $\Lambda_{ij,kl}(\hat{\mathbf{n}})$, (see Appendix B.1), giving

$$h_{ij}^{TT}(t,\mathbf{x}) = \Lambda_{ij,kl}(\hat{\mathbf{n}})\frac{\kappa}{4\pi}\int \frac{d^3x'}{|\mathbf{x}-\mathbf{x}'|}T^{kl}\left(t-|\mathbf{x}-\mathbf{x}'|,\mathbf{x}'\right) , \tag{2.1}$$

where $\hat{\mathbf{n}}$ is the unit vector in the direction to the observer from the source, the primed coordinates represent that of the source and the unprimed coordinates are of the observer in the far zone. N.B.: in the *TT* gauge, $h_{0\mu}^{TT} = 0$ and therefore we only need to use the spatial indices.

2.1.1 Low-velocity expansion

Let us consider a system whose motion, induced by gravity, consists of non-relativistic velocities, $v \ll 1$. The frequency of the emitted gravitational waves, ω, will be of the same order as the frequency of the source, ω_s, which is proportional to v,

$$\omega \sim \omega_s \sim \frac{v}{a} , \tag{2.2}$$

where a is the size of the source. In this low-velocity limit we note that the wavelength of the emitted gravitational waves will be much longer than a. When we consider solutions to (2.1) at distances $D \gg a$, we may expand

$$|\mathbf{x}-\mathbf{x}'| = D - \mathbf{x}'\cdot\hat{\mathbf{n}} + \dots , \tag{2.3}$$

but keep only the leading term in the denominator. Hence at large distances (2.1) is simplified to

$$h_{ij}^{TT}(t,\mathbf{x}) = \Lambda_{ij,kl}(\hat{\mathbf{n}})\frac{\kappa}{4\pi D}\int d^3x'\ T^{kl}\left(t-D+\mathbf{x}'\cdot\hat{\mathbf{n}},\mathbf{x}'\right) , \tag{2.4}$$

As $\mathbf{x}'\cdot\hat{\mathbf{n}} \ll D$, we can Taylor expand (2.4),

$$h_{ij}^{TT}(t,\mathbf{x}) = \Lambda_{ij,kl}(\hat{\mathbf{n}})\frac{\kappa}{4\pi D} \times \left[S^{kl} + n_m\dot{S}^{kl,m} + \frac{1}{2}n_m n_p\ddot{S}^{kl,mp} + \dots\right] , \tag{2.5}$$

where S^{kl} are the moments of T^{ij} and are related to the moments, M, of the energy density, T^{00}, as

$$S^{ij} = \frac{1}{2}\ddot{M}^{ij} , \tag{2.6}$$

(see Appendix B.3.3). The metric perturbation may also be expressed as a multipole expansion, in which case S^{kl} is proportional to the second time derivative of the *quadrupole* moment, which we define as

$$Q^{ij} = M^{ij} - \frac{1}{3}\delta^{ij} M_{kk} \tag{2.7a}$$

$$= \int d^3x \rho(t, \mathbf{x}) \left(x^i x^j - \frac{1}{3} r^2 \delta^{ij} \right) , \tag{2.7b}$$

where $\rho = T^{00}$, which in the low-velocity expansion is dominated by the rest mass of the binary. It is interesting to note that as the quadrupole moment is the leading order term there exists no monopole or dipole gravitational radiation.

The moments of the energy density and the linear moments are discussed in more detail in Appendix B, and will be used in Section 2.4. N.B.: in the TT gauge $Q^{ij} = M^{ij}$.

2.1.2 Quadrupole radiation

Physically the absence of monopole and dipole gravitational radiation are typically understood as the conservation of energy and angular momentum respectively, which is the correct explanation in linearised theory (see Appendix B.3.3), but is not true in general. Indeed it is clear that if we wish to detect gravitational waves we require energy to be emitted so that it can cause tidal forces to be imposed upon our detector. However, it is generally true that monopole and dipole gravitational radiation do not exist. The correct explanation, given in, e.g., [15], is that the graviton has helicity ±2 and therefore cannot have a total angular momentum of 0 or 1 that would correspond to the monopole and dipole, respectively.

We can now understand the nature of sources of gravitational waves. The gravitational quadrupole is a measure of the distribution of mass that is non-zero for an asymmetric system. Additionally, for radiation to be emitted, the quadrupole moment of the system must have a non-zero second time derivative, i.e., it must be accelerating. Some types of astrophysical sources that are expected to emit such gravitational radiation were briefly described in Section 1.3.4, including CBCs.

2.1.3 Calculating the polarisations

The contraction of the quadrupole moment with the lambda tensor yields the quadrupole gravitational radiation as

$$h_{ij}^{TT} = \frac{\kappa}{2\pi D} \ddot{M}_{ij}^{TT} , \tag{2.8}$$

where

$$\ddot{M}_{ij}^{TT} = \ddot{Q}_{ij}^{TT} = \Lambda_{ij,kl}\ddot{Q}_{kl} \,. \tag{2.9}$$

However, we would like to relate (2.8) to the + and × polarisations observed by a detector. It can be shown (e.g. [15]) that when the propagation direction $\hat{\mathbf{n}}$ is in the z direction, the polarisations are simply

$$h_+ = \frac{\kappa}{2\pi D}\left(\ddot{M}_{11} - \ddot{M}_{22}\right) \,, \tag{2.10a}$$

$$h_\times = \frac{\kappa}{4\pi D}\ddot{M}_{12} \,. \tag{2.10b}$$

The general solution for an observer in any direction depends upon all six moments, M_{ij}, and two angles, i and ϕ, that relate the source frame to the propagation frame. The former is the inclination angle between the z-axis of the source frame and the direction of propagation. The latter is the simply the phase offset, i.e., the angle of rotation of the binary with respect to the y-axis.

2.2 A binary system

Let us now turn our attention to the gravitational wave polarisations emitted from a binary system. We assume the binary consists of compact objects of mass m_1 and m_2, that are moving in a circular orbit with a separation distance a in the x-y plane. We model the evolution and gravitational wave emission of the binary assuming adiabatic circular motion using Newtonian orbital mechanics and the lowest order PN corrections that give the energy loss due to the gravitational radiation. Higher order corrections will be introduced in Section 2.4.

Switching to the centre-of-mass frame the binary may be represented by a single body of reduced mass

$$\mu = \frac{m_1 m_2}{m_1 + m_2} \,, \tag{2.11}$$

that moves in an effective potential and whose evolution is described with the following relative coordinates

$$x_0(t) = a\cos\left(\omega_s t\right) \,, \tag{2.12a}$$

$$y_0(t) = a\sin\left(\omega_s t\right) \,, \tag{2.12b}$$

$$z_0(t) = 0 \,, \tag{2.12c}$$

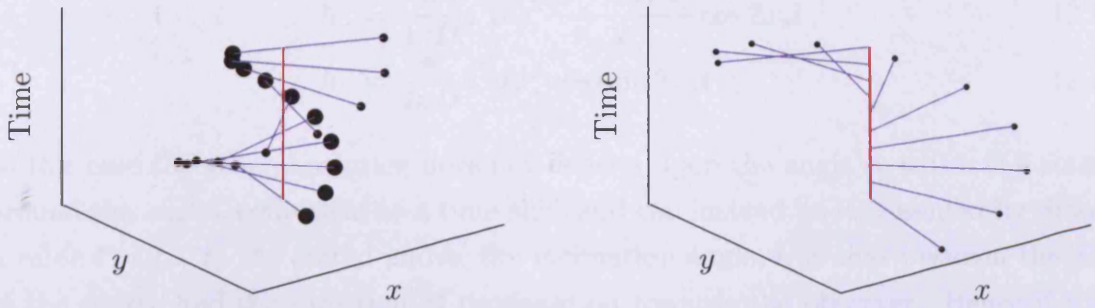

FIGURE 2.1: The left plot shows a binary system of component masses $m_1 = 2m_2$ orbiting their centre of mass, indicated by the vertical red line. The centre-of-mass, single-body representation of the same system is shown on the right. The single body is orbiting the same point as on the left with a reduced mass, μ, attracted to a 'ghost' mass $m_1 + m_2$.

that give its position relative to the centre of mass of the two bodies (see Figure 2.1). This single body approach allows us to obtain simple expressions for the mass moments (see Appendix B.2), namely,

$$M_{ij}(t) = \mu x_{i0}(t) x_{j0}(t) \,. \tag{2.13}$$

We therefore find

$$M_{11} = \mu a^2 \frac{1 + \cos(2\omega_s t)}{2} \,, \tag{2.14a}$$

$$M_{22} = \mu a^2 \frac{1 - \cos(2\omega_s t)}{2} \,, \tag{2.14b}$$

$$M_{12} = \mu a^2 \frac{\sin(2\omega_s t)}{2} \,. \tag{2.14c}$$

We can see from (2.14) that the frequency of the gravitational waves emitted from a binary system are *twice* the orbital frequency. In qualitative terms this can be understood by the symmetry of the system; if the objects are of equal mass then the binary has the same configuration twice every orbit.

Finally by calculating the second time derivatives of (2.14) and using the general solution for the polarisations as opposed to (2.10), as shown in, e.g, [15], we find the observed gravitational wave polarisations to be

$$\begin{aligned} h_+ &= \frac{\kappa}{4\pi D} a^2 \mu \omega_s^2 \frac{(1+\cos^2 i)}{2} \cos 2\omega_s t \,, && \text{(2.15a)} \\ h_\times &= \frac{\kappa}{4\pi D} a^2 \mu \omega_s^2 \cos i \sin 2\omega_s t \,. && \text{(2.15b)} \end{aligned}$$

In this case the general solution does not depend upon the angle ϕ, which is a rotation around the z-axis, equivalent to a time-shift and can instead be represented by choosing a value $t' = t + t_0$. As stated above, the inclination angle, i, is that between the z axis of the source and the direction of propagation towards the observer. Hence if $i = 0$, we see the binary 'face-on' and both polarisations are of equal amplitude, in which case the gravitational waves are said to be circularly polarised. However, if the binary is 'edge-on', $i = \pi/2$, then the gravitational waves are linearly polarised and only consist of the + polarisation. This can be qualitatively understood from Figure 1.1. Observing an edge-on binary, and recalling that gravitational waves are transverse we would only need one dimension to describe the motion of the binary. On the other hand a face-on binary requires two dimensions to describe its motion. N.B.: for inclination angles between 0 and $\pi/2$, there will be unequal contributions from the + and × polarisations; such gravitational waves are said to be elliptically polarised.

One further point of significance, seen in (2.15), is that the gravitational wave amplitude depends upon the frequency and amplitude squared, which is the same order as the square of the source velocities, i.e., $v^2 \sim a^2\omega_s^2$.

2.2.1 Energy emission

We expect a priori the emission of gravitational waves to take energy away from binary systems. The loss of energy causes the orbital separation to decrease and the bodies *inspiral* towards each other[1].

The energy carried by gravitational waves is found by calculating the energy-momentum tensor due to the gravitational wave itself, from which the gravitational wave flux in a given direction can be found. Integrating the flux over a sphere gives the total luminosity, $\mathscr{L}$, of the emitted gravitational waves. This results in the energy balance equation

$$\frac{dE}{dt} = -\mathscr{L} = -\frac{1}{5}\left\langle \dddot{Q}_{ij}^{TT} \dddot{Q}^{TTij} \right\rangle \,, \tag{2.16}$$

---

[1] Indeed, this very process has been observed [5] (see section 1.3.5).

where E is the total energy of the binary and the brackets indicate that we are averaging over several wavelengths[2]. Thus to calculate the energy loss of a binary we take the third time derivatives of (2.14)

$$\dddot{M}_{11} = -4\mu a^2 \omega_s^3 \sin(2\omega_s t) \;, \tag{2.17a}$$

$$\dddot{M}_{22} = -\dddot{M}_{11} \,, \tag{2.17b}$$

$$\dddot{M}_{12} = 4\mu a^2 \omega_s^3 \cos(2\omega_s t) \;. \tag{2.17c}$$

It can be shown that the time dependent parts average out and the energy loss is

$$\frac{dE}{dt} = -\frac{32}{5}\mu^2 a^4 \omega_s^6 \,. \tag{2.18}$$

2.2.2 Evolution of the binary

Under the assumption that the orbit is adiabatic we can use Kepler's equations to understand the dynamics of the source. Kepler's third law states that the square of the orbital period is proportional to the cube of the semi-major axis, which gives the relation between the frequency of the source and the separation

$$\omega_s^2 = \frac{M}{a^3} \,, \tag{2.19}$$

where $M = m_1 + m_2$ is the total mass. This simple relation shows us that as the binary inspirals the orbital frequency increases. We can, therefore, conclude that the gravitational wave frequency and amplitude increase as the system evolves. We can then determine the evolution of the binary system by substituting (2.19) into (2.18), giving

$$\frac{dE}{dt} = -\frac{32}{5}\frac{\mu^2 M^3}{a^5} \,. \tag{2.20}$$

The total energy of a binary system in the Newtonian limit is simply

$$E = \frac{1}{2}\mu v^2 - \frac{\mu M}{a} = -\frac{\mu M}{2a} \,, \tag{2.21}$$

from which we can obtain dE/da and subsequently

$$\frac{da}{dt} = -\frac{64}{5}\frac{\mu M^2}{a^3} \,, \tag{2.22}$$

---

[2] A detailed derivation is given in [15], a more accessible derivation can be found in [16].

which we integrate to find the evolution of the binary separation

$$a(t) = \left(\frac{256}{5}\mu M^2\right)^{\frac{1}{4}}(t_c - t)^{\frac{1}{4}}\,, \tag{2.23}$$

where t_c is the coalescence time $(a = 0)$. The evolution of the orbital frequency is found simply by substituting (2.19) into (2.23) which yields

$$\omega_s(t) = \left(\frac{256}{5}\right)^{-\frac{3}{8}}\mathcal{M}^{-\frac{5}{8}}(t_c - t)^{-\frac{3}{8}}\,. \tag{2.24}$$

where we define the *chirp mass*

$$\mathcal{M} = \eta^{\frac{3}{5}}M\,, \tag{2.25}$$

and the *symmetric mass ratio*

$$\eta = \frac{\mu}{M}\,. \tag{2.26}$$

Finally we define the orbital phase of the binary

$$\varphi(t) = \int \omega_s(t)dt\,, \tag{2.27a}$$

$$\varphi(t) = -\frac{8}{5}\left(\frac{256}{5}\right)^{-\frac{3}{8}}\mathcal{M}^{-\frac{5}{8}}(t_c - t)^{\frac{5}{8}}\,. \tag{2.27b}$$

We now have all that is required to understand the evolution of the gravitational waves radiated from a binary system. It is useful to express the polarisations in terms of their amplitude and phase evolution:

$$h_+(t) = A(t)\frac{(1 + \cos^2 i)}{2}\cos(2\varphi(t)) \tag{2.28a}$$

$$h_\times(t) = A(t)\cos i \sin(2\varphi(t))\,, \tag{2.28b}$$

where

$$A(t) = \frac{\kappa\mu M}{4\pi D a(t)}\,. \tag{2.29}$$

N.B.: the polarisations are $\pi/2$ out of phase and hence they may also be referred to as the two "phases" of the gravitational wave.

Figure 2.2 shows qualitatively the evolution of the orbital separation, the source frequency, the amplitude of the gravitational wave and its + polarisation. The amplitude and frequency increase as the waveform evolves, giving it a 'chirp' characteristic that depends upon the chirp mass (2.25). Figure 2.3 shows a cartoon evolution of the single-body representation in centre-of-mass frame.

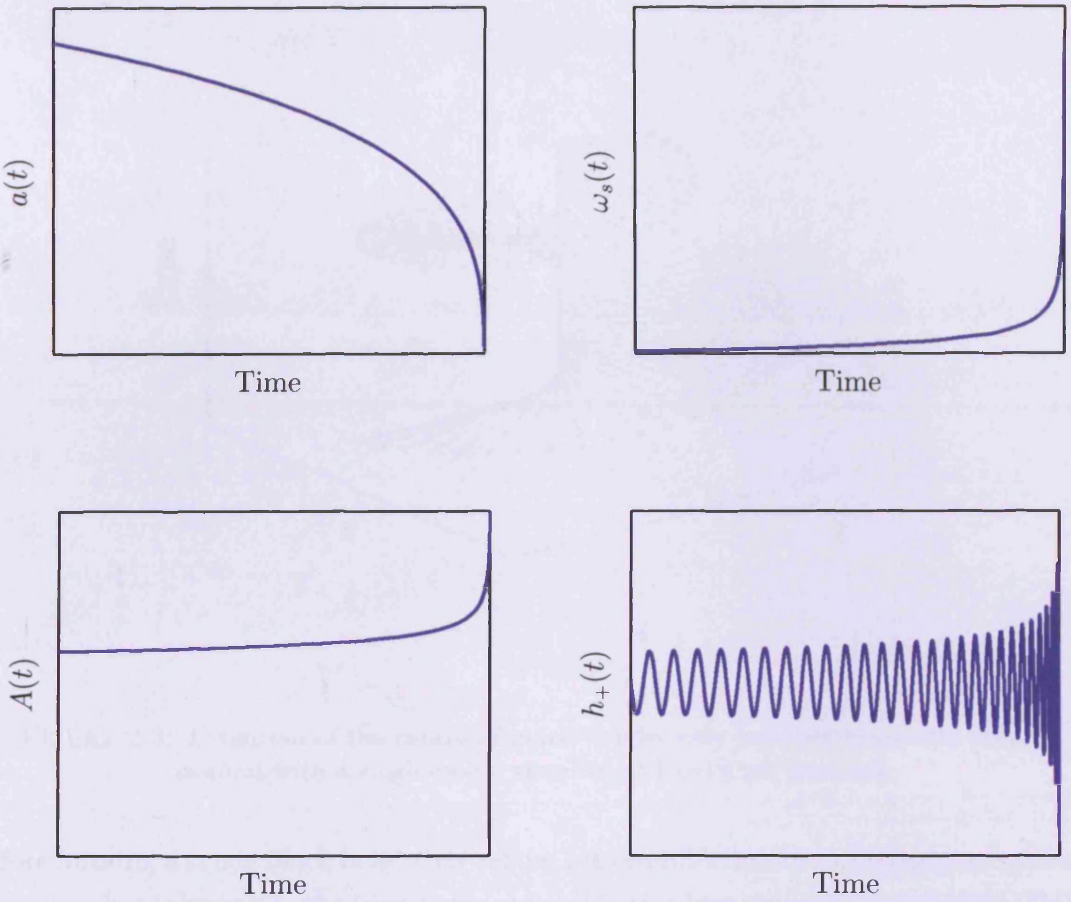

FIGURE 2.2: Evolution of the orbital separation (top left), the orbital frequency (top right), the gravitational wave amplitude (bottom left) and the + polarisation (bottom right) for a given system shown in arbitrary units.

2.2.3 Inspiral waveforms

The evolution of the binary has thus far been derived assuming adiabatic circular motion, which is only valid until the binary reaches the innermost stable circular orbit (ISCO). This period in the binary evolution is known as the 'inspiral' stage after which the above equations cannot be used to describe the system. The ISCO of the Schwarschild metric occurs at a distance of three times the Schwarschild radius ($6M$). Therefore, inspiral waveforms are usually evolved until the separation reaches that value. Inspiral waveform models are often evolved via the gravitational wave frequency and are terminated at the corresponding frequency of last stable orbit (FLSO), which is easily calculated from (2.19).

As the binary approaches merger, the two objects begin to plunge towards each other

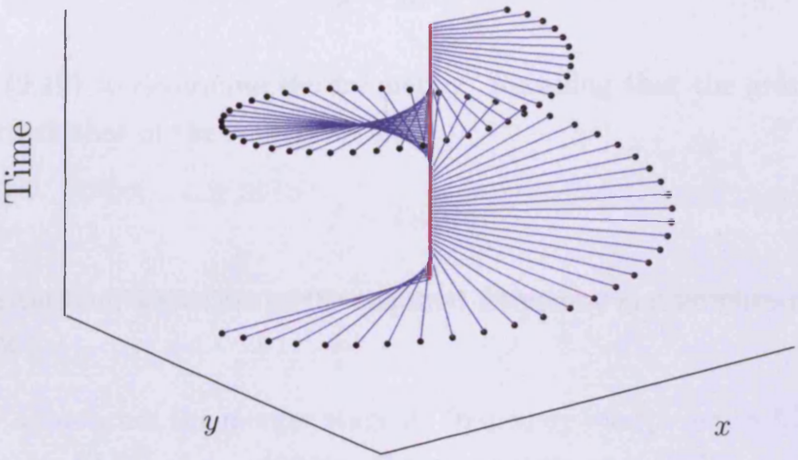

FIGURE 2.3: Evolution of the centre-of-mass, single-body representation of a binary inspiral with a single-body, sampled at fixed time intervals.

before forming a single black hole[3] that settles into equilibrium by emitting gravitational waves in what is known as the 'ringdown' stage [17, 18]. Inspiral-merger-ringdown (IMR) waveforms that include the merger and ringdown phase can be calculated by matching the inspiral stage to the merger and ringdown stages computed using numerical relativity simulations of merger dynamics [19, 20]. In this thesis, we will consider inspiral-only waveforms and not IMR waveforms, with the exception of Chapter 5.

2.3 Why are gravitational waves from CBCs of interest?

In Chapter 1 we learned that ground-based interferometric detectors can reach sensitivities of 10^{-22} in the frequency range of around 100-1000 Hz (see Figure 1.4). We now have everything we need to estimate the amplitude and frequency of gravitational waves radiated by CBCs. Let us consider a neutron star-black hole binary (NSBH), of component masses $1.4M_{\odot}$ and $10M_{\odot}$, close to its ISCO ($a = 8M$), observed at a distance of 100 Mpc (The Virgo galaxy cluster is a mere 18 Mpc from the Milky Way).

---

[3] Recall that we are considering compact objects where the minimum mass system would consist of two neutron stars.

The amplitude is given by (2.29), which, after substituting $a = 8M$, we multiply by G/c^2 to convert from natural units to standard units giving

$$h \sim 10^{-21} \,. \tag{2.30}$$

We then use (2.19) to determine the frequency. Recalling that the gravitational wave frequency is twice that of the source, we find

$$f \sim 250\,\mathrm{Hz}\,, \tag{2.31}$$

Thus the gravitational waves are of the required frequency and amplitude to be observable by LIGO!

As the binary approaches the merger stage its frequency sweeps across LIGO's sensitive band, reaching its FLSO of $f \sim 400\,\mathrm{Hz}$. Binary neutron star (BNS) systems are lower in mass and their frequency evolution sweeps across the entire sensitive band with an FLSO of $f \sim 2000\,\mathrm{Hz}$, whereas binary black hole (BBH) systems reach their FLSO[4] in the most sensitive part of the detector's band - at about 220 Hz for a $(10, 10)M_\odot$ binary. Thus all of these systems are ideal detection candidates for LIGO.

2.4 Higher order waveforms

When calculating the gravitational wave polarisations we chose[5] to keep only the leading order term in the expansion of T_{kl}. We will begin our journey into the use of higher order waveforms by considering the polarisations in linearised theory that include the first beyond leading order (FBLO) term. However, as we shall, see that is merely the tip of the iceberg.

2.4.1 First beyond leading order linearised polarisations

It can be shown, e.g., [15], using (B.8), (B.9) and (B.10), that the second term in the expansion of T_{kl} (2.5) is

$$\dot{S}^{ij,k} = \frac{1}{6}\dddot{M}^{ijk} + \frac{1}{3}\left(\ddot{P}^{i,jk} + \ddot{P}^{j,ik} - 2\ddot{P}^{k,ij}\right) \,. \tag{2.32}$$

Typically the two terms on the RHS of (2.32) are separated into the moments of the energy density and the momentum density (see Section B.3.2), respectively, where the

---

[4] The FLSO is explicitly defined in Section 4.1.1.

[5] It was not really a choice as we were working in linearised theory.

former corresponds to the mass octopole moment and the latter the current quadrupole moment[6]. However, in the approximation for non-relativistic (low-velocity) particles it is straightforward to compute $\dot{S}^{ij,k}$ directly. From (B.8b) we can write

$$S^{kl,m} = \mu \dot{x}^k \dot{x}^l x^m \,, \tag{2.33}$$

and its time derivative

$$\dot{S}^{kl,m} = \mu \left[\left(\ddot{x}^k \dot{x}^l + \dot{x}^k \ddot{x}^l \right) x^m + \dot{x}^k \dot{x}^l \dot{x}^m \right] \,. \tag{2.34}$$

We can already note two interesting things about the mass octopole and current quadrupole gravitational radiation. Firstly, the FBLO term in (2.5) depends upon the direction to the observer from the source, specifically n^m, such that if the observer is orthogonal to the orbital plane then $\hat{n} \cdot \mathbf{x} = 0$ and, hence, the FBLO term disappears. Thus we see that there must be motion of the binary components in the direction of the observer (i.e., the inclination angle must be non-zero), or there will be no gravitational radiation of this order towards the observer. Secondly, we can see that both terms in (2.34) will have a factor $(a\omega_s)^3$ in the amplitude, an extra factor of $a\omega_s$ compared with the leading order term. Recall that this is the same order as the of the velocities of the source that are small compared to unity. Therefore, an increase in the order of velocity leads to a smaller amplitude of the radiation.

For a binary system with an inclination angle, i, between the z-axis of the source coordinates and the rotational axis of the binary, the equations of motion are

$$x_0(t) = a \cos\left(\omega_s t\right) \,, \tag{2.35}$$

$$y_0(t) = a \cos i \sin\left(\omega_s t\right) \,, \tag{2.36}$$

$$z_0(t) = a \sin i \sin\left(\omega_s t\right) \,. \tag{2.37}$$

For a gravitational wave propagating along z, the polarisations are found by calculating the FBLO term in (2.5),

$$\left(h_{ij}^{TT}\right)_{\text{FBLO}} = \frac{\kappa}{4\pi D} \dot{S}_{ij,3}^{TT} \,, \tag{2.38}$$

which gives

$$\left(h_{+}^{TT}\right)_{\text{FBLO}} = \frac{\kappa}{4\pi D} \frac{1}{8} \mu a^3 \omega_s^3 \sin i \left[\left(\cos^2 i - 3 \right) \cos\left(\omega_s t\right) - 3 \left(1 + \cos^2 i \right) \cos\left(3\omega_s t\right) \right] \,, \tag{2.39a}$$

$$\left(h_{\times}^{TT}\right)_{\text{FBLO}} = \frac{\kappa}{4\pi D} \frac{1}{8} \mu a^3 \omega_s^3 \sin\left(2i\right) \left[\sin\left(\omega_s t\right) - 3 \sin\left(3\omega_s t\right) \right] \,. \tag{2.39b}$$

---

[6] The quadrupole of the angular momentum density.

Interestingly the FBLO gravitational radiation introduces a first and third harmonic of the orbital frequency.

2.5 Post-Newtonian formalism

Thus far we have described the nature of gravitational waves, in particular those radiated from CBCs, using linearised theory. The leading order term in the gravitational radiation corresponded to the mass quadrupole moment and higher order terms could be calculated as required via the Taylor expansion (2.5). However, the gravity of the source itself and the effects of energy-momentum emission on the orbital dynamics, which produce corrections to the leading order term, were not taken into account. Hence, in linearised theory, without these corrections, we cannot *correctly* calculate the terms beyond leading order, i.e., $\mathcal{O}(v^3)$, including (2.39).

The post-Newtonian (PN) formalism is an iterative, perturbative approach to solving the EFE, that gives an expansion in terms of (v^2/c^2). Hence for the rest of this chapter we shall drop the natural units to keep to the tradition of the PN formalism. PN theory can be used to provide highly accurate waveform models of the *expected* gravitational radiation emitted by CBCs. In gravitational wave data analysis it is very important [21, 22] to have accurate models of the phase evolution when using the matched filter (see Chapter 3).

The PN expansion for binary systems is typically used to calculate the energy of the binary and the luminosity, both to high order, e.g., $(v/c)^7$ [23]. The phase evolution of the binary may then be constructed by a variety of different methods using the energy balance equation.

2.5.1 Basic overview

The PN formalism is a complex subject; here a very basic overview of the process is given (see, e.g., [15]).

- The spacetime metric is written again as flat spacetime plus a perturbation $\mathrm{h}_{\mu\nu}$, where $\mathrm{h}_{\mu\nu}$ may contain non-linear terms, i.e.,

$$\mathrm{h}_{\mu\nu} = \Sigma_{n=1}^{\infty} G_n \mathrm{h}_{\mu\nu}^{n} \,. \tag{2.40}$$

- In the Lorentz gauge, the EFE are written as

$$\Box \mathrm{h}_{\mu\nu} = +\frac{16\pi G}{c^2}\tau_{\mu\nu}\,, \tag{2.41}$$

  where $\tau_{\mu\nu}$ consists of the energy-momentum tensor *and* highly non-linear terms of the perturbation.

- As before, in linearised theory, (2.41) can be integrated using the retarded Green's function. However, the result has the perturbation on both sides of the equation, for which an analytical solution cannot be found.

- Outside the source the energy-momentum tensor is zero. Writing $\mathrm{h}_{\mu\nu}$ as an expansion in powers of G one can match terms of the same order on the LHS and RHS. The process is iterative: first $\mathrm{h}_{\mu\nu}$ is found to order G, and recycled in to the solution to find the term of order G^2 etc.

- The solution outside the source is then written as a multipole expansion that depends upon two sets of moments, I and J, which are unknown.

- To determine I and J, one must use the above iterative process inside the source. In this case $\mathrm{h}_{\mu\nu}$ and $\tau_{\mu\nu}$ are expanded in terms of $(1/c)$. As before terms of the same order are matched in an iterative process.

- By re-expanding the solution outside the source in powers of (v/c) the moments I and J can be matched with the solution inside the source, which then yields the gravitational wave polarisations.

2.5.2 PN order

The results from the PN approximation differ from linearised theory, but share the same characteristics. The leading order term in the amplitude is of order v^2/c^2 and the frequency of the gravitational wave is twice the orbital frequency. The next term introduces a first and third harmonic and its amplitude is of order v^3/c^3.

The leading order term is denoted 0PN in order, whereas the FBLO term is 0.5PN in order. The next highest term has an amplitude of order v^4/c^4 and is denoted 1PN in order, etc. The PN notation is used to described other quantities, e.g., flux, acceleration, etc., where the leading, 0PN, term is of a general order $(v/c)^n$. The FBLO, 0.5PN, term is then of order $(v/c)^{n+1}$, etc.

2.6 PN phase approximants

Once the PN expressions for the binary's energy and luminosity are determined, the gravitational wave phase may be calculated using the energy-balance equation (2.16). Defining the flux as

$$F(v) = -M\frac{dE(v)}{dt}\,, \tag{2.42}$$

the energy balance equation may be written as

$$-\frac{dE}{dt} = -\frac{dE}{dv}\frac{dv}{dt} = \frac{F}{M}\,. \tag{2.43}$$

Using Kepler's laws we see that the velocity of the source, v, is related to the source frequency as

$$v = (M\omega_s)^{\frac{1}{3}}\,. \tag{2.44}$$

Therefore, (2.16) and (2.44) lead to two non-linear, ordinary differential equations

$$\frac{dv}{dt} = -\frac{1}{M}\frac{F}{dE/dv}\,, \tag{2.45}$$

and

$$\frac{d\varphi}{dt} = \frac{v^3}{M}\,. \tag{2.46}$$

The flux, $F(v)$, is calculated by the PN method [24]. Ideally we wish to find $v(t)$, by integrating (2.45), and then $\varphi(t)$ by integrating (2.46). However, the RHS of (2.45) consists of a fraction where both numerator and denominator are polynomial functions of v. There are three popular ways in which one can find $\varphi(t)$, known as the Taylor-T1, Taylor-T2 and Taylor-T3 approximants [25][7]. The Taylor-T1 approximant is found by simply integrating (2.45) numerically to find $v(t)$. To find the Taylor-T2 approximant one expresses $F/\left(dE/dv\right)$ as an infnite series in v, truncating at the appropriate order before integrating. Finally, the Taylor-T3 approximant is found by using the infinite series of the Taylor-T2 approximant and inverting it to find $v(t)$.

We know from the evolution of the binary that the phase should be monotonically increasing. When generating a waveform model for data analysis, the above approximants are considered invalid if the condition

$$\frac{df}{dt} > 0\,, \tag{2.47}$$

is violated, at which point the evolution of the waveform should be terminated. The stability of the each of the Taylor approximants will vary with the parameters of the

---

[7] There is also a Taylor-T4 approximant among others [25].

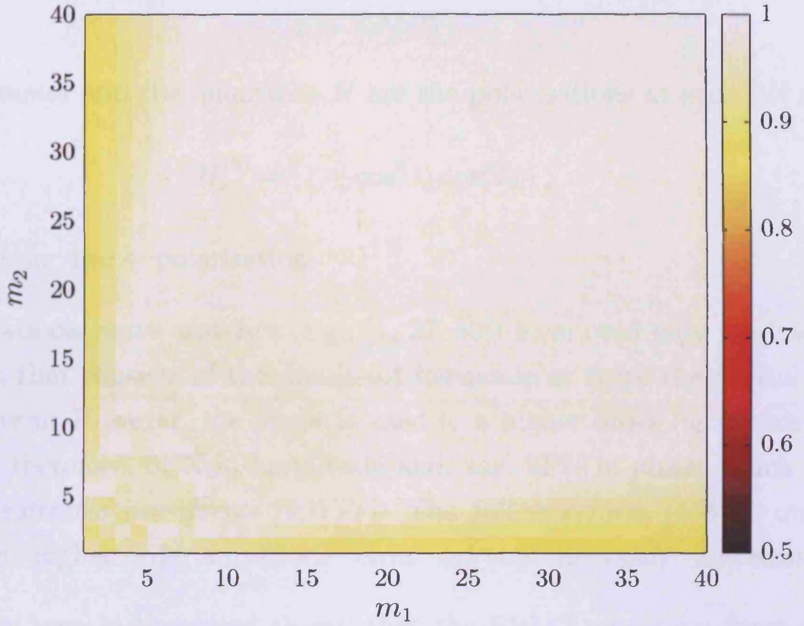

FIGURE 2.4: The ratio of the termination frequency to the FLSO for the TT3 approximant at 2PN. The ratio is typically above 0.9, which is adequate; the frequency is increasing dramatically as the binary approaches ISCO. The phase evolution will therefore be terminated at a time very close to that at which it would reach FLSO.

waveform and with the PN order at which the phase is determined. The Taylor-T3 approximant is found to be particularly stable at 2PN as shown in Figure 2.4, where the ratio of termination frequency to the FLSO is plotted for a range of binaries, characterised by their component masses.

In later chapters we shall use the Taylor-T3 (TT3) approximant at 2PN (see Appendix B.4) and also its FD analog, the stationary-phase approximation (SPA).

2.7 Restricted and full PN waveforms

The gravitational wave polarisations have been solved to 3PN order [26] and the gravitational wave phase has been solved to 3.5PN order [23]. The polarisations may be expressed as

$$h_{+,\times} = \frac{2G\mu x}{c^2 R}\left\{H^{(0)}_{+,\times} + x^{\frac{1}{2}}H^{(\frac{1}{2})}_{+,\times} + xH^{(1)}_{+,\times} + x^{\frac{3}{2}}H^{(\frac{3}{2})}_{+,\times} + x^2 H^{(2)}_{+,\times} + x^{\frac{5}{2}}H^{(\frac{5}{2})}_{+,\times} + x^3 H^{(3)}_{+,\times}\right\}, \tag{2.48}$$

where

$$x = (v^2/c^2)\,, \tag{2.49}$$

is the PN parameter and the quantities H are the polarisations at each PN order, e.g.,

$$H_+^{(0)} = (1 + \cos^2 i)\cos(2\varphi)\,, \tag{2.50}$$

is the 0PN term for the + polarisation.

To date, gravitational wave searches (e.g., [1, 27–30]) have used only the leading order amplitude term that consists of the dominant harmonic at twice the orbital frequency, i.e., the $H_{+,\times}^{(0)}$ term. However, the phase is used to a higher order (as it must be). The waveforms are, therefore, 0PN in amplitude and, say, 2PN in phase. Such waveforms are known as *restricted waveforms (RWFs).* The *full waveform (FWF),* on the other hand, retains the higher order amplitude terms and contains many interesting features.

We have already seen in linearised theory that the FBLO term introduces a first and third harmonic of the orbital frequency. Below we will discuss in more detail the differences between the RWF and the FWF, including the higher order terms that contain other harmonics of the orbital frequency and *amplitude corrections* to the existing harmonics.

2.7.1 Harmonics and amplitude corrections

Table 2.1 shows how the higher order amplitude terms contribute to the polarisations. As we know, the FBLO term introduces a first and third harmonic of the orbital frequency. The 1PN amplitude term consists of a correction to the, dominant, second harmonic and a fourth harmonic. Each of the remaining higher order terms contain corrections to existing harmonics and introduce a new harmonic.

The + and × polarisations, of course, have different coefficients and they are generally out of phase by $\pi/2$, e.g.,

$$H_+^{(0.5)} = -\Delta \sin i \left[\left(\frac{5}{8} + \frac{1}{8}\cos^2 i\right)\cos\varphi - \left(\frac{9}{8} + \frac{9}{8}\cos^2 i\right)\cos(3\varphi)\right]\,, \tag{2.51a}$$

$$H_\times^{(0.5)} = -\Delta \sin i \cos i \left[-\frac{3}{4}\sin\varphi + \frac{9}{4}\sin(3\varphi)\right]\,, \tag{2.51b}$$

where

$$\Delta = \frac{m_1 - m_2}{m_1 + m_2}\,. \tag{2.52}$$

An arbitrary binary (both polarisations)									
PN order	$\mathcal{O}$	φ	2φ	3φ	4φ	5φ	6φ	7φ	8φ
0	v^2/c^2	·	●	·	·	·	·	·	·
0.5	v^3/c^3	●	·	●	·	·	·	·	·
1	v^4/c^4	·	●	·	●	·	·	·	·
1.5	v^5/c^5	●	●	●	·	●	·	·	·
2	v^6/c^6	●	●	●	●	·	●	·	·
2.5	v^7/c^7	●	●	●	●	●	·	●	·
3	v^8/c^8	●	●	●	●	●	●	·	●

TABLE 2.1: The harmonics/amplitude corrections present in each of the PN amplitude terms. N.B.: this table is for the general case and some of the above contributions may be zero for particular binary systems and/or source orientations.

However, some of the higher order terms are 'mixed', i.e., they have amplitude corrections at both phases, e.g., $H_+^{(2)}$ contains *apparent* amplitude corrections of the first and third harmonic of the $H_\times^{(0.5)}$ term, (2.51b).

The polarisations up to 2PN are listed in Appendix B.5.

N.B.: as expected the 0.5PN polarisations (2.51) differ from the FBLO term in linearised theory (2.39).

2.7.2 Dependence on inclination angle and mass difference

The polarisations h_+ and $h_\times$ describe the gravitational wave propagating in the direction of the observer. We saw in linearised theory, (2.39), that the first and third harmonic only propagate towards the observer if the binary is inclined with respect to the propagation direction, i.e., if the inclination angle is non-zero. The result is the same in the PN approximation, as can be seen in (2.51). In fact, none of the higher order terms contribute to the polarisations in the direction of the observer if the binary is face-on, except for the amplitude corrections to the second harmonic of the orbital phase, as summarised in Table 2.2. However, if the binary is observed 'edge-on' ($i = 90°$) then the contributions are the same as given in Table 2.1, except that the gravitational wave is linearly polarised and only consists of the + polarisation.

A result of the PN expansion is that the odd harmonics also depend upon the mass difference, Δ, such that if the binary components are of equal mass the odd harmonics at all orders vanish, see, e.g., (2.51). This may be understood qualitatively by returning to the argument as to why the gravitational wave frequency is twice that of the orbital frequency. We argued that the binary returns to its start position twice every orbit, due

Binary observed face-on ($i = 0$)									
PN order	$\mathcal{O}$	φ	2φ	3φ	4φ	5φ	6φ	7φ	8φ
0	v^2/c^2	·	●	·	·	·	·	·	·
0.5	v^3/c^3	·	·	·	·	·	·	·	·
1	v^4/c^4	·	●	·	·	·	·	·	·
1.5	v^5/c^5	·	●	·	·	·	·	·	·
2	v^6/c^6	·	●	·	·	·	·	·	·
2.5	v^7/c^7	·	●	·	·	·	·	·	·
3	v^8/c^8	·	●	·	·	·	·	·	·

TABLE 2.2: The harmonics/amplitude corrections present in each of the PN amplitude terms, for a binary observed face-on.

An equal mass binary ($i \neq 0$)									
PN order	$\mathcal{O}$	φ	2φ	3φ	4φ	5φ	6φ	7φ	8φ
0	v^2/c^2	·	●	·	·	·	·	·	·
0.5	v^3/c^3	·	·	·	·	·	·	·	·
1	v^4/c^4	·	●	·	●	·	·	·	·
1.5	v^5/c^5	·	●	·	·	·	·	·	·
2	v^6/c^6	·	●	·	●	·	●	·	·
2.5	v^7/c^7	·	●	·	●	·	·	·	·
3	v^8/c^8	·	●	·	●	·	●	·	●

TABLE 2.3: The harmonics/amplitude corrections present in each of the PN amplitude terms, for equal mass binary systems.

to the symmetry of the system. However, the system is less symmetric when the masses are unequal and so one might expect odd harmonics in that case. Table 2.3 summarises the contributions to the polarisations of an equal mass binary.

2.7.3 Influence of the amplitude corrections on the structure of the waveform

Although the higher order terms are much smaller in amplitude they can lead to considerable differences between the RWF and the FWF in the time domain (TD). Figure 2.5 shows the difference for a variety of systems as observed by LIGO, where the FWF is at 2PN in amplitude. As expected the differences are greater for non-zero inclination angles and larger mass ratios.

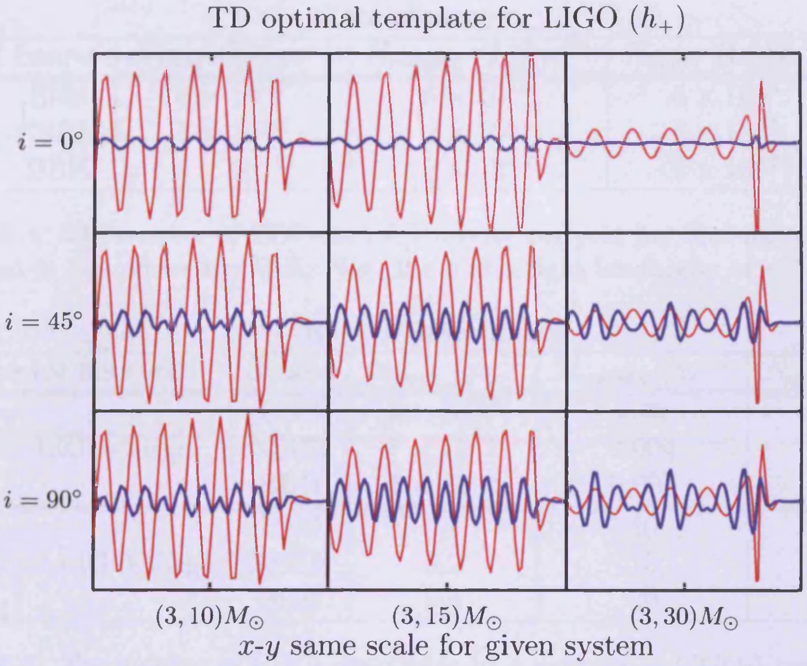

FIGURE 2.5: The RWF is plotted in the background and the *difference* between the RWF and the FWF (2PN) is plotted in the foreground (bold). The waveforms are as observed by LIGO for a variety of inclination angles and mass ratios.

Considering that FWF should be regarded a closer representation of nature's gravitational waves, we have a clear motivation for investigating the use of higher order waveforms in the search for gravitational waves. We will discuss this further in Chapter 4, where the spectra of the RWF and FWF are compared in Section 4.1.2.

2.8 Predicted rates of observable CBCs

Here we briefly outline recent work by Abadie et al. [31], who produced a summary of the expected rates of CBCs observable by current and future ground-based interferometric detectors. The detection rates were predicted using various sources of information including observations of GRBs and radio binary pulsars, the results of previous gravitational-wave searches, and galaxy catalogs that provide population information of the local Universe. The predicted rates, of course, vary for the different types of binaries, i.e., the component masses. Here we shall be interested in BNS, BBH, and NSBH[8].

---

[8] These binary systems are precisely defined in Chapter 3.

Rate of mergers

Source	$N_{\text{lower}}\ /\mathrm{L}_{10}^{-1}\mathrm{yr}^{-1}$	$N_{\text{realistic}}\ /\mathrm{L}_{10}^{-1}\mathrm{yr}^{-1}$	$N_{\text{upper}}\ /\mathrm{L}_{10}^{-1}\mathrm{yr}^{-1}$
BNS	6×10^{-7}	6×10^{-5}	6×10^{-4}
NSBH	3×10^{-8}	2×10^{-6}	6×10^{-5}
BBH	6×10^{-9}	2×10^{-7}	2×10^{-5}

TABLE 2.4: The number of CBCs in the Universe per year per blue-light luminosity, measured in L_{10}, where the Milky Way has a blue-light luminosity of $\sim 1.7\ \mathrm{L}_{10}$ [33].

Rate of detections

Detector network	Source	$N_{\text{lower}}\ /\mathrm{yr}^{-1}$	$N_{\text{realistic}}\ /\mathrm{yr}^{-1}$	$N_{\text{upper}}\ /\mathrm{yr}^{-1}$
Initial LIGO-Virgo	BNS	2×10^{-4}	0.02	0.2
	NSBH	7×10^{-5}	0.004	0.1
	BBH	2×10^{-4}	0.007	0.5
Advanced LIGO-Virgo	BNS	0.4	40	400
	NSBH	0.2	10	300
	BBH	0.4	20	1000

TABLE 2.5: The number of CBCs observable by a network of LIGO-Virgo detectors per year for the initial and Advanced detector networks [31].

There are large uncertainties in the predicted rates due to small statistics of the observations, unknown parameters in astrophysical models etc. The rates are, therefore, given with quite a large range between the lower and upper bounds. Table 2.4 gives the rates of coalescences, whereas Table 2.5 quotes the subsequent detection rates, predicted for initial and advanced LIGO-Virgo [32] detector networks, giving the lower and upper bounds and a 'realistic' estimate [31].

The detection rates correspond to a signal-to-noise ratio (SNR) of 8 in each detector of the network, assuming the signal is a RWF. In practice, differences between the true signal and the RWF, such as sub-dominant harmonics, could lead to a loss in SNR (and, hence, detection rates) if the search relies on RWF models.

A network of initial LIGO and Virgo detectors could be expected to detect inspirals from coalescing BNS systems at a rate of one every five years (optimistic rate) to one every five-thousand years (pessimistic rate). However, with a network of advanced detectors we can be confident of making the first direct gravitational wave detections within ten years. Advanced detectors should herald a new era by opening the gravitational window for observational astronomy. Observations with advanced detectors should answer many questions in relativistic astrophysics such as direct evidence for the existence of black holes, strong field tests of general relativity, black hole no-hair theorem, progenitors of gamma-ray bursts, precursors of magnetar flares, etc. It may be the gravitational window that will one day reveal what happened shortly after the big bang by detecting primordial gravitational waves.

Chapter 3

How to search for gravitational waves from compact binary coalescences

In essence, the search for gravitational waves from CBCs is a simple affair. The expected waveforms are accurately modelled and once gravitational wave strain data are available (which is of course a huge task for experimenters) a correlation integral is performed over a set of signal templates that cover the parameter space of the search. In practice, however, data analysis pipelines become quite complicated once all the considerations of a running a search, such as data reduction, coincidence analysis, background estimation, detection efficiency, and dealing with non-stationary noise etc., are taken into account.

We begin with an introduction to the concept of signal processing before presenting a detailed derivation of the matched filter, closely following that of Wainstein and Zubakov [34]. The latter parts of the chapter include the results of a search for gravitational waves from low mass CBCs in 186 days of LIGO's 5th science run (S5) data, beginning with an overview of the data analysis pipeline, which makes use of the matched filter, followed by close attention to the analysis of 20 days of data.

3.1 Signal processing and filters

Signal processing refers to the act of performing *useful* mathematical operations upon a continuous or discrete time series. There are many useful applications of signal processing, e.g., radar that was developed during the first half of the 20th century and famously used by the RAF to win the Battle of Britain in World War II.

Here, we are interested in processing *input data* that may consist of only noise or *both* signal and noise. A *filter* will perform operations on the input data, producing *output data.* When the signal is present in the input data, the output data will ideally consist of the transformed signal, i.e., *the filter extracts the signal from noise.* In practice, the output data will consist partly of the transformed noise and partly the transformed signal. Thus we wish to use a filter that maximises the SNR.

Where the expected signal is known, as it is in the search for gravitational waves from CBCs, the filter that provides the largest SNR is the *matched filter.*

3.2 The matched filter

Before we derive the matched filter it is useful to understand the following:

1. The matched filter is a *linear* filter, i.e., the output data result from linear operations of the filter on the input data. The output, $y(t)$, of a filter, $\mathcal{K}$, acting on the input, $x(t)$, takes the form

$$y(t) = \mathcal{K}x(t)\,, \tag{3.1a}$$

$$y(t) = \int_{-\infty}^{\infty} k(\tau)x(t-\tau)d\tau\,, \tag{3.1b}$$

   where $k(\tau)$ is the *impulse response* function of the filter, i.e., the response of the filter to a unit impulse (the delta function),

$$k(\tau) = \int_{-\infty}^{\infty} k(\tau - t)\delta(t)dt\,. \tag{3.2}$$

2. The *transfer function,* $K(f)$, of the filter is the Fourier transform (FT) of the impulse response function.

3. The matched filter is only the optimum filter where the noise is a stationary and normal random process, i.e., a stationary random process obeying a Gaussian distribution. It is often convenient to use the power spectral density (PSD) of the noise, $S_n(f)$, defined as the FT of the auto-correlation function, $R_n(\tau)$,

$$S_n(f) = \int_{-\infty}^{\infty} R_n(\tau)e^{-2\pi i f\tau}d\tau\,, \tag{3.3}$$

where

$$R_n(\tau) = \overline{n(t)n(t-\tau)}\,. \tag{3.4}$$

The noise is said to be stationary if the auto-correlation function depends upon only the value of the time offset, τ, and not the time, t. At $\tau = 0$, the auto-correlation function reduces to the mean-square value of the noise,

$$R_n(\tau) = R_n(0) = \overline{n^2}\,. \tag{3.5}$$

3.2.1 Derivation of the matched filter

Let us apply a linear filter, $\mathcal{K}$, to some data, $x(t)$, that gives the output data

$$y(t) = \mathcal{K}x(t)\,. \tag{3.6}$$

If the data is a linear combination of noise, $n(t)$, and a known signal, $m(t)$, i.e.,

$$x(t) = n(t) + m(t)\,, \tag{3.7}$$

the output of the filter is simply,

$$\begin{align} y(t) &= \mathcal{K}n(t) + \mathcal{K}m(t)\,, \tag{3.8a} \\ &= \nu(t) + \mu(t)\,, \tag{3.8b} \end{align}$$

where $\nu(t)$ and $\mu(t)$ are the filtered values of the noise and the signal respectively,

$$\nu(t) = \int_{-\infty}^{\infty} k(t')n(t-t')dt'\,, \tag{3.9}$$

and

$$\mu(t) = \int_{-\infty}^{\infty} k(t')m(t-t')dt'\,. \tag{3.10}$$

Under the assumption that the noise is Gaussian and stationary with a mean value of zero ($\overline{n} = 0$), we will find it easier to work with the PSD using the relation (3.3). The mean square of the output of the filter with the noise $\nu(t)$ is then

$$\overline{\nu^2} = \int_{-\infty}^{\infty} |K(f)|^2 S_n(f) df\,, \tag{3.11}$$

where $K(f)$ is the transfer function. Applying the convolution theorem to (3.10) allows us to write the filtered signal as the inverse Fourier transform (IFT) of the filtered value in the frequency domain (FD),

$$\mu(t) = \int_{-\infty}^{\infty} e^{i2\pi ft} K(f)\widetilde{m}(f)df\,. \tag{3.12}$$

The SNR, $\rho^2(t_0)$, is then defined as

$$\rho^2(t_0) = \frac{\mu^2(t_0)}{\overline{\nu^2}} = \frac{\left|\int_{-\infty}^{\infty} e^{i2\pi ft_0} K(f)\widetilde{m}(f)df\right|^2}{\int_{-\infty}^{\infty} |K(f)|^2 S_n(f)df}\,. \tag{3.13}$$

The filter, $K(f)$, is a *matched filter* if it is the best at extracting the signal from the noise, i.e., it must maximise the SNR.

Multiplying $\mu(t_0)$ by $\sqrt{S_n(f)/S_n(f)}$ and using the *Cauchy-Schwarz* inequality we have

$$\left|\int_{-\infty}^{\infty} e^{i2\pi ft_0} K(f)\widetilde{m}(f)df\right|^2 \leq \int_{-\infty}^{\infty} |K(f)|^2 S_n(f)df \int_{-\infty}^{\infty} \frac{|\widetilde{m}(f)|^2}{S_n(f)}df \tag{3.14}$$

or

$$\left|\int_{-\infty}^{\infty} e^{i2\pi ft_0} K(f)\widetilde{m}(f)df\right|^2 \leq \overline{\nu^2} \int_{-\infty}^{\infty} \frac{|\widetilde{m}(f)|^2}{S_n(f)}df\,. \tag{3.15}$$

If we now divide both sides of (3.15) by $\overline{\nu^2}$, we can rewrite the SNR as

$$\rho^2(t_0) \leq \int_{-\infty}^{\infty} \frac{|\widetilde{m}(f)|^2}{S_n(f)}df\,, \tag{3.16}$$

where the RHS is the expected value. Comparing (3.13) and (3.16) we can see that ρ^2 is maximised with the filter that has the transfer function

$$K(f) = \gamma e^{-i2\pi ft_0} \frac{\widetilde{m}^*(f)}{S_n(f)}\,, \tag{3.17}$$

where γ is an arbitrary constant. Thus the matched filter is defined.

3.2.2 Application of the matched filter

To understand how the filter is applied in a search for gravitational waves from CBCs, we must consider the signal as seen in the detector, i.e., (1.41). Here we will consider a RWF signal. We recall (1.41):

$$h(t) = F_+ h_+ + F_\times h_\times\,.$$

Suppose

$$h_{+} = h_0 \cos\left(2\varphi(t)\right) , \tag{3.18a}$$

$$h_{\times} = h_{\frac{\pi}{2}} \sin\left(2\varphi(t)\right) . \tag{3.18b}$$

The resulting expression can be simplified as

$$h(t) = A(t) \cos\left(2\varphi(t) - \Phi_0\right) , \tag{3.19}$$

where

$$A(t) = \left[F_{+}^{2} h_0^{2} + F_{\times}^{2} h_{\frac{\pi}{2}}^{2}\right]^{1/2} , \tag{3.20a}$$

$$\cos\Phi_0 = \frac{F_{+} h_0}{A} , \tag{3.20b}$$

$$\sin\Phi_0 = \frac{F_{\times} h_{\frac{\pi}{2}}}{A} . \tag{3.20c}$$

$$\tag{3.20d}$$

The angle Φ_0 in (3.19) contains the information about the two polarisations and depends upon the sky position and the inclination of the source relative to the detector. These angles cannot be known *a priori* and therefore must be maximised over.

Now that the matched filter is derived, we can search data, x, with a *template* of the expected signal, h, by defining the following *inner product* as the output of matched filtering x with h. Choosing $\gamma = 1$ we have

$$\langle x, h\rangle := 4\mathrm{Re} \int_0^{\infty} e^{-i2\pi f t_0} \frac{\tilde{h}^{*}(f)\tilde{x}(f)}{S_n^1(f)} df , \tag{3.21}$$

where we have used the *one-sided* PSD, $S_n^1(f)$[1]. The expected value of the SNR, in the presence of a signal that exactly matches the template, is given by $\langle h, h\rangle$.

Signal-to-noise ratio The SNR is given by normalising the matched filter so that the recovered signal can be scaled by its amplitude in the noise,

$$\rho = \frac{\langle x, h\rangle}{\langle h, h\rangle^{\frac{1}{2}}} . \tag{3.22}$$

---

[1] The PSD, as defined before, is an even function, i.e., $S_n(f) = S_n(-f)$. The one sided PSD uses only the positive frequencies and introduces a factor of 2.

If the template is normalised, such that the inner product with itself[2] is equal to unity, i.e.,

$$\langle \bar{h}, \bar{h} \rangle = 1 \,, \tag{3.23}$$

where

$$\bar{h} = \frac{h}{\langle h, h \rangle^{\frac{1}{2}}} \,, \tag{3.24}$$

then the SNR may be written as

$$\rho = \langle x, \bar{h} \rangle \,. \tag{3.25}$$

If we consider a two-phase template of the form (3.19), we can define the following two phases as

$$h_c = A(t) \cos 2\varphi(t) \,, \tag{3.26a}$$

$$h_s = A(t) \sin 2\varphi(t) \,. \tag{3.26b}$$

If we then filter the data we have [35],

$$\langle x, \bar{h} \rangle = \langle x, \bar{h}_c \rangle \cos \Phi_0 + \langle x, \bar{h}_s \rangle \sin \Phi_0 \,, \tag{3.27}$$

which we can rewrite as,

$$\langle x, \bar{h} \rangle = \left[\langle x, \bar{h}_c \rangle^2 + \langle x, \bar{h}_s \rangle^2 \right]^{1/2} \cos \left(\Phi_0 - \alpha \right) \,, \tag{3.28}$$

where

$$\alpha = \tan^{-1} \frac{\langle x, \bar{h}_s \rangle}{\langle x, \bar{h}_c \rangle} \,. \tag{3.29}$$

We cannot know the angle, $\Phi_0 - \alpha$, a priori, but can assume it has a uniform distribution between 0 and 2π. It is clear that the maximum value of (3.28) will occur when

$$\Phi_0 = \alpha \,. \tag{3.30}$$

Therefore, we can write the maximum output of the *two-phase* matched filter as

$$\langle x, \bar{h} \rangle = \left[\langle x, \bar{h}_c \rangle^2 + \langle x, \bar{h}_s \rangle^2 \right]^{1/2} . \tag{3.31}$$

---

[2] The square root of the inner product of two normalised quantities is known as the *overlap*.

3.3 The LIGO search pipeline

The pipeline described here is similar to that used in several LIGO searches [27–30] and also [1], for which the results are presented later in this chapter. Each stage of the pipeline will be described in detail, but we begin with a basic overview:

1. A template bank is generated covering the parameters of the search.
2. The data is matched filtered with each template generating *first-stage single-detector triggers.*
3. The first stage single detector triggers from the two LIGO sites are compared to see if coincident events exist, producing a list of *first-stage coincident triggers.*
4. The data is matched filtered using only the templates associated with first-stage coincident triggers. The new triggers are subjected to signal-based vetoes, producing a list of *second-stage single-detector triggers.*
5. The second stage single-detector triggers are checked for coincidence between the LIGO sites, producing a list of *second-stage coincident triggers.*
6. The second-stage coincident triggers are ranked according to their FAR when compared with background trials.

3.3.1 Generating a template bank

A signal model of n parameters will form a manifold of n dimensions on which templates are placed discretely to construct a template bank. If spin and higher harmonics are neglected and the sky angles are maximised over as in (3.31), then the templates can be placed on a two-dimensional manifold corresponding to the component masses of the binary.

The discreteness of the template bank will cause a loss in SNR for signals whose parameters do not exactly match any of the templates in the bank. This loss can be limited by setting a threshold known as the minimum match, M_{min}, of the bank, e.g, $M_{min} = 0.95$ (recall the maximum overlap is unity). The match, M, between two nearby templates, $h(\lambda^\mu)$ and $h(\lambda^\mu + \Delta\lambda^\mu)$, where λ^μ are the intrinsic parameters[3] (e.g., the component masses as opposed to the sky location), is given by

$$M = \langle h(\lambda^\mu), h(\lambda^\mu + \Delta\lambda^\mu) \rangle \ , \tag{3.32}$$

---

[3] The Greek indices run from $1, \ldots, n$, where n is the number of parameters.

which can be Taylor expanded:

$$M = \langle h(\lambda^\mu), h(\lambda^\mu)\rangle + \frac{\partial M}{\partial \Delta\lambda^\mu}\Delta\lambda^\mu + \frac{1}{2}\frac{\partial^2 M}{\partial\Delta\lambda^\mu \partial\Delta\lambda^\nu}\Delta\lambda^\mu\Delta\lambda^\nu + \dots . \tag{3.33}$$

The first term in the expansion is equal to unity by definition; the second term will be neglected as it will tend to zero around the maxima of M at $\Delta\lambda^\mu = 0$; terms beyond the second derivative will be discarded as they are negligible. The resulting expression for the match becomes

$$M = 1 + \frac{1}{2}\frac{\partial^2 M}{\partial\Delta\lambda^\mu \partial\Delta\lambda^\nu}\Delta\lambda^\mu\Delta\lambda^\nu . \tag{3.34}$$

If we define the metric tensor of the template manifold as [36]

$$g_{\mu\nu} = -\frac{1}{2}\frac{\partial^2 M}{\partial\lambda^\mu \partial\lambda^\nu}\Delta\lambda^\mu\Delta\lambda^\nu , \tag{3.35}$$

we can rewrite the *mismatch* between two nearby templates in terms of the metric tensor:

$$1 - M = g_{\mu\nu}\Delta\lambda^\mu\Delta\lambda^\nu . \tag{3.36}$$

Thus templates are then placed such that the *maximum* distance between one template and another in the direction of each parameter, x^μ, is

$$\Delta\lambda^{\mu 2} = \frac{2(1-M)}{g_{\mu\mu}} . \tag{3.37}$$

Therefore, a signal that is of the same family as the templates, but without exactly matching parameters, would suffer a loss in SNR of no greater than 5% for a minimum match of 0.95. N.B.: In practice, placing templates using the spacing in the direction of single parameters will leave some areas of the parameter space uncovered and, therefore, the actual placement algorithm may use a smaller spacing [37].

The optimum template placement is obtained using a hexagonal template placement algorithm [37] in the (τ_0, τ_3) parameter space, where τ_0 and τ_3 are the chirp times[4] of the 0 and 1.5PN contributions to the phase. The chirp time parameters are used because their metric is approximately flat, as opposed to that of the component masses (m_1 and m_2). Therefore, the metric distance between templates can be considered constant across the entire parameter space, reducing the computational cost of template placement.

---

[4] The duration of the signal evolution from the initial to the final frequency.

3.3.2 First stage analysis

The data from each interferometer are matched filtered independently over the *entire* template bank resulting in a SNR time series for each template. A 'trigger' is generated when the SNR time series exceeds a given threshold, ρ_*, which is a tunable parameter. A low SNR threshold will produce a large number of triggers, i.e., have a high false alarm probability. On the other hand a high SNR threshold will reduce the sensitivity of the search. Therefore, the threshold is typically set low enough so that the search remains as sensitive as possible, whilst still being computationally manageable. Given a large trigger rate, where many triggers may be associated with a single template at adjacent values in the SNR time series, the data is reduced by clustering over the duration of the template. For each template, the trigger with the largest value of the SNR time series within that time window is recorded, whilst the others are discarded.

Furthermore, a single noise transient (or a signal!) will cause many *different* templates to register triggers at the same time. Therefore, the triggers are further reduced by clustering those that are adjacent in the template bank. A three dimensional metric is generated, (τ_0, τ_3, t), that is used to cluster the triggers over time as well as the template bank parameters. Starting with a seed trigger on the metric, an error ellipsoid of constant metric distance, ϵ_f, is constructed. Further error ellipsoids are then generated for all the surrounding triggers within a time window, $\pm T_t$, of the seed trigger[5]. Any trigger with an error ellipsoid that overlaps with the seed trigger's ellipsoid, is clustered with the seed trigger. This process is repeated for each trigger within the original cluster until no further triggers can be added, at which point the trigger with the greatest SNR in the cluster is saved whilst all the others are discarded.

3.3.3 First stage coincidence

Due to a considerable amount of environmental background noise, a trigger cannot be considered as a gravitational wave detection candidate unless it is observed in coincidence by detectors at different locations. Therefore, we require triple or double coincidence between the two LIGO sites, i.e., an H1H2L1 trigger in all three detectors or an H1L1/H2L1 trigger. However, since H1 is twice as sensitive as H2 and colocated, triggers that are *only* found in H2, when H1 is operating normally, are rejected. This will be discussed in more detail in section 3.3.6. Triggers can also be found in H1H2 coincidence, but are not analysed (see Section 3.3.8).

---

[5] The time window T_t is simply twice the maximum value that an error ellipsoid can extend in the t direction, i.e., error ellipsoids are not drawn for triggers so far away in time that they cannot be clustered.

The coincidence algorithm [38] is similar to the first stage data reduction algorithm. First the triggers from each interferometer are time ordered. Then an error ellipsoid is defined around the first trigger in the list. The size of the error ellipsoid depends upon the template's location on the metric, but cannot be greater than a tunable parameter, ϵ_t, known as *e-thinca*. Further metric-dependent error ellipsoids of the same maximum size are then defined for all the triggers from each of the interferometers within a time window $\pm T_c$. In this case the time window is set in the same manner as T_t, but also accounts for the light-travel time between the LIGO sites (i.e., there could be a time delay of up to the distance between the sites divided by the speed of light). If any of the additional triggers' ellipsoids overlap with the original trigger then they are recorded together as a coincident trigger. This process is repeated for all the remaining triggers in the list. Triggers that are not found to be in coincidence are discarded. The final list may contain coincident triggers that are duplicated, i.e., an H1L1 trigger that also exists as part of an H1H2L1 trigger, in which case the H1L1 trigger is removed from the list.

3.3.4 Template bank reduction

The second stage of the analysis introduces signal-based vetoes and consistency checks. The checks are potentially computationally expensive and would considerably increase the latency of the pipeline if used when the entire template bank is matched filtered. Instead, the template bank is reduced to a subset known as the 'trigbank'. The trigbank consists of all the templates that were part of a coincident trigger at the end of the first stage. This process can dramatically reduce the number of templates used to analyse a segment of data. For example, the template bank in Figure 3.5 was reduced from 7477 templates to 1851.

3.3.5 Second stage analysis with signal vetoes

The second stage analysis is similar to the first stage, but uses the trigbank for matched filtering rather than the template bank and introduces two signal-based vetoes, namely χ^2 and r^2.

The χ^2 veto For a given trigger, the χ^2 discriminator measures the consistency of power distribution between the data and the template. The template, h, is divided into

n bins that provide equal contribution to the expected SNR,

$$\langle h_k, h_k\rangle = \frac{\langle h, h\rangle}{n}, \tag{3.38}$$

for all values of the index $k = 1, \ldots, n$. The χ^2 statistic computes the SNR for each of the bins and compares with the expected value; taking into account the power distribution from both phases of the filter (3.31), it is defined as

$$\chi^2 = \sum_{k=1}^{n} \left[\left(\langle x, h_{0k}\rangle - \frac{\langle h_0, h_0\rangle}{n} \right)^2 + \left(\langle x, h_{\frac{\pi}{2}k}\rangle - \frac{\langle h_{\frac{\pi}{2}}, h_{\frac{\pi}{2}}\rangle}{n} \right)^2 \right]. \tag{3.39}$$

It is clear that if the data and template match exactly, the χ^2 value is zero by definition. More realistically, if the data consists of Gaussian noise, plus a signal exactly matching the template, the function (3.39) follows a classic χ^2 distribution with $2n-2$ degrees of freedom [39]. The χ^2 veto is useful because transient sources of noise are very unlikely to have the same power distribution as the template and will therefore have large values of χ^2.

Before setting the threshold, a few things must be taken into consideration. Firstly, real detector noise is not Gaussian and there will be more excess power than expected from the noise. Additionally the template and signal parameters are unlikely to match exactly because of the discreteness of the bank and the models used to generate templates will not be exact matches of nature's gravitational wave signals. Consequently, a genuine signal with a large SNR can be expected to have a large χ^2. Therefore, the χ^2 veto is weighted by the SNR, defining a new quantity

$$\xi^2 = \frac{\chi^2}{n + \delta\rho^2}. \tag{3.40}$$

Triggers are vetoed when

$$\xi^2 > \xi_*^2, \tag{3.41}$$

where ξ_*, δ and the number of bins, n, are tunable parameters.

A combination of the χ^2 value and the SNR, called the *effective SNR*, ρ_{eff}, is used to rank triggers at the second stage of the pipeline. The effective SNR weights the SNR of a trigger by its χ^2 value and is defined as

$$\rho_{\text{eff}}^2 = \frac{\rho^2}{\left[\left(\frac{\chi^2}{2n-2} \right) \left(1 + \frac{\rho^2}{m} \right) \right]^{1/2}}, \tag{3.42}$$

where m is a tunable parameter. The effective SNR reduces the ranking of triggers with high values of χ^2, which are more likely to originate from noise glitches than a signal.

The r^2 veto An additional quantity, r^2, is defined by renormalising χ^2 such that it has an expectation value of ~ 2,

$$r^2 = \frac{\chi^2}{n} . \tag{3.43}$$

For a given trigger, the veto is constructed by measuring the r^2 value in a time window that precedes the time of the trigger[6] A trigger will be vetoed if the r^2 value exceeds a threshold, r_*^2, for a duration $\Delta t > \Delta t_*$, where r_*^2 and Δt_* are tunable parameters.

In practice, two r^2 thresholds are set; one that is constant for low SNR triggers ($\rho < 10$), and another that increases linearly with SNR to account for the fact that these triggers will have a larger χ^2.

3.3.6 Second stage coincidence with signal consistency checks

At the second stage coincidence analysis, two further checks are made between the consistency of what is seen in the co-aligned and co-located detectors, H1 and H2. The effective distance cut compares the amplitude of a trigger recorded in both detectors, whereas the amplitude consistency check rejects triggers that were seen in only one detector that *should* have been seen in both.

The effective distance cut The effective distance, D_{eff}, is the distance attributed to a trigger under the assumption that it is directly overhead the detector and optimally orientated or, in other words, it is the furthest distance (up to Gaussian fluctuations) at which a source could have produced a trigger of a given SNR. The effective distance is, therefore, independent of detector sensitivity and a gravitational wave detected in H1 and H2, in principle, should have the same effective distance,

$$D_{\text{eff}} = \frac{\langle h_{1\,\text{Mpc}}, h_{1\,\text{Mpc}} \rangle}{\langle x, h_{1\,\text{Mpc}} \rangle} , \tag{3.44}$$

where the template $h_{1\,\text{Mpc}}$ was generated at a distance of 1 Mpc so that the effective distance has units of Mpc.

---

[6] Recall that inspiral-only waveforms model up to the coalescence time and we cannot know the expected χ^2 in the time following the trigger.

The effective distance cut sets a threshold on the allowed difference between the effective distance of triggers measured coincidently between H1 and H2, defined as

$$\kappa = \frac{2\left|D_{\mathrm{eff,H1}} - D_{\mathrm{eff,H2}}\right|}{D_{\mathrm{eff,H1}} + D_{\mathrm{eff,H2}}}. \tag{3.45}$$

The cut will be applied when κ is greater than a tunable parameter, κ_*.

The amplitude consistency check The effective distance cut can also be applied when a trigger is present in only one of two co-aligned detectors. The range, R, (also known as the horizon distance) of a detector for a given template, h, is defined as the distance at which an optimally orientated source (that exactly matches the template) has an expectation value of the SNR equal to 8, i.e.,

$$R = \frac{\langle h, h\rangle^{\frac{1}{2}}}{8}. \tag{3.46}$$

The range of the detector and the effective distance of a trigger are related by the SNR, allowing the effective distance cut to be rewritten in terms of the ranges. In the absence of a trigger in H2, the maximum expected SNR in H1 is then defined as

$$\rho_{\mathrm{max\ H1}} = \frac{R_{\mathrm{H1}}\left(2+\kappa_*\right)}{R_{\mathrm{H2}}\left(2-\kappa_*\right)}\rho_*. \tag{3.47}$$

Thus any triggers present in H1 only, when H2 is operating, will be discarded if $\rho > \rho_{\mathrm{max\ H1}}$.

3.3.7 Data quality vetoes

The behaviour of the LIGO detectors varies due to environmental factors that affect the quality of the data, e.g., periods of seismic activity may cause a high rate of triggers. When the data are analysed, as many of the known environmental factors as possible must be taken in to account and periods of corrupt data may be vetoed, i.e., removed from the analysis. There are four categories of vetoes, for which the analysis requires a list of times when they are active. The vetoes are typically identified by studying *auxiliary channels*, i.e., channels that monitor the state of the detector.

The vetoes are categorised in the following order:

- Category 1: The data is known to be severely corrupted, or even missing.

- Category 2: An auxiliary channel exhibits anomalous behaviour and a known coupling between the channel and the gravitational wave strain channel exists.
- Category 3: An auxiliary channel exhibits anomalous behaviour, but a less well established coupling between the channel and the gravitational wave strain channel exists.
- Category 4: An auxiliary channel exhibits anomalous behaviour, but there is little knowledge of the coupling between channels, although a correlation is known to exist.

When running an analysis, the pipeline is usually run first with no vetoes applied, then repeated with category 1 vetoes, then category 2 etc. The information obtained from each run may be useful for characterising the detectors[7]. The remaining data after application of category 1 and 2 vetoes are usually considered good enough to search for gravitational wave candidates. However, often category 3 vetoes are also applied. Category 4 vetoes may later be used to scrutinise any potential gravitational wave candidates.

3.3.8 Background estimation

To estimate the background the pipeline is run multiple times using time-slide data, i.e., the data of the two LIGO sites are time shifted by a time greater than the light-travel time between the detectors. Therefore, any coincident triggers that occur in the time shifted analyses cannot be from a gravitational wave signal and indicate the background rate. The time-shifted data are known as the background data whereas the non-time-shifted data are known as the foreground or zero-lag data. Typically one-hundred time slides are performed and the number of coincident triggers of a given *ranking* present in the foreground are compared with the average number of coincident triggers of equivalent or higher ranking present in the background.

3.3.9 Detection statistic - false alarm rate (FAR)

The detection statistic compares the zero-lag data with the average of the time-shifted data. At the first stage of the analysis, a simple approach was to rank triggers by their effective SNR. However, higher mass waveforms have fewer gravitational wave cycles in the detectors' sensitive band and the signal based vetoes are not as effective. Thus the

---

[7] This does not affect the need for a blind analysis (see Section 3.4).

rate of background triggers is expected to be higher. If the loudest foreground trigger is a BNS template it could be hidden due to equally loud high mass BBH template triggers in the background.

When computing a detection statistic, one can divide up the parameter space into different mass regions. For each of the foreground triggers a FAR can be defined by comparing with the number of equally loud background triggers in that region of the parameter space. The FAR then allows triggers from different regions of the parameter space to be compared and ranked together. One must also consider that different types of coincidences (H1L1 or H1H2L1) will have different background rates and should also be compared independently.

When the different categories from each observation time are recombined to give the final detection statistic, the FAR of each trigger needs to be renormalised by the number of trials (i.e., the number of categories), such that the expected FAR of the loudest trigger is $1/T$ where T is the observation time.

As H1 and H2 are co-located, their noise is correlated and the time-shift method cannot be used to measure the background. Therefore, a FAR cannot be calculated for H1H2 triggers and they are not included in the final trigger ranking or the upper limit calculation. H1H2 triggers in H1H2 time may be looked at in case a gold-plated detection candidate exists, but as it is not known how to estimate the background it would be difficult to attribute a level of significance to them.

3.3.10 Upper limits

Once the search is completed an upper limit on the rate of CBCs can be calculated for the nearby Universe. The procedure for calculating upper limits is described in detail in [40–42] and requires the following: the sensitivity of the search, the loudest event and the background probability.

Brief description of the upper limit calculation For a given rate, R, of CBCs, the probability of obtaining no triggers 'louder' than a given FAR, x, due to the background *or* a signal, is defined as

$$P\left(x|B,R,T\right) = P_B(x)e^{-RC_L(x)T}\,, \tag{3.48}$$

where B is the background rate, $P_B(x)$ is the probability of obtaining no background triggers louder than x, T is the duration of the search and $C_L(x)$ is the sensitivity of the search, defined as the cumulative luminosity to which the search can see a trigger of ranking x[8]. Given that no triggers were louder than the loudest event, one can define a posterior rate distribution based on the FAR of the loudest event, x_m:

$$p\left(R|x_m, T, B\right) \propto p(R) \left[\frac{1 + \Lambda R C_L(x_m)T}{1+\Lambda}\right] e^{-RC_L(x_m)T}\,, \tag{3.49}$$

where $p(R)$ is the prior probability distribution on the rates, usually the result of the previous search, and Λ is the likelihood that the loudest event is due to a gravitational wave as opposed to a background event, which depends upon the background and sensitivity distributions:

$$\Lambda = \frac{C_L'(x_m)}{|P_B'(x_m)|}\frac{P_B(x_m)}{C_L(x_m)}\,, \tag{3.50}$$

where $C_L'(x_m) = dC_L/dx$, etc. One can then compute the rate upper limit, R_*, for a given confidence level, α,

$$\alpha = \int_0^{R_*} p\left(R|x_m, T, B\right)\,. \tag{3.51}$$

The search sensitivity In describing the upper limit calculation above, the search sensitivity, C_L, was introduced, which is the *cumulative luminosity*: the blue-light luminosity, measured in units of L_{10}[9] , of all the local galaxies that may contain CBCs to which the search is sensitive to. To calculate C_L one must know the efficiency of the search as a function of distance and chirp mass, $\epsilon(D_{\mathrm{eff}}, M_c)$ and the luminosity of the local Universe, also as a function of distance and chirp mass, $L(D_{\mathrm{eff}}, M_c)$. The cumulative luminosity is then defined as

$$C_L = \int \epsilon(D_{\mathrm{eff}}, M_c) L(D_{\mathrm{eff}}, M_c) dD_{\mathrm{eff}} dM_c\,. \tag{3.52}$$

The blue-light luminosity is used as it is assumed that the rate of CBCs is proportional to the star formation rate, which is in turn proportional to the blue-light luminosity [43].

The efficiency function is calculated by adding simulated signals (injections) to the data and evaluating the fraction of detected signals, louder than x_m, for a given set of parameters. The luminosity function is calculated by multiplying the efficiency of signal recovery for the search as a function of distance by the physical luminosity as a function of distance and integrating their product over distance.

---

[8] When using the FAR as a detection statistic, a lower value is louder, e.g., a one-false-alarm-per-year event is louder than a two-false-alarm-per-year event.

[9] L_{10} is 10^{10} times the blue solar luminosity (the Milky Way contains $\sim 1.7\ \mathrm{L}_{10}$ [33]).

Uncertainties in calculating the rate upper limit There are a number of uncertainties which affect the upper limit calculation, including Monte Carlo statistics, detector calibration, distances and luminosities of galaxies listed in the galaxy catalog [43] and differences between the templates used to evaluate the efficiency of the search and the true waveforms of nature. All of these uncertainties may be marginalised over when computing the posterior rate distribution [40].

3.4 The S5 low mass CBC search

The fifth science run of LIGO began in November 2005 and concluded in September 2007, with all three detectors operating at design sensitivity. A search for gravitational waves from low mass CBCs was performed on the data, with the analysis divided into three epochs. The S5 first year (S51YR) search consisted of data collected between November 4th, 2005 and November 14th, 2006 [29]. Towards the end of S5, as of May 18th 2007, the Virgo detector collected Virgo Science Run 1 (VSR1) data in coincidence with LIGO. The analysis pipeline of the joint search using both LIGO and Virgo data required significant changes from that used in the S51YR search, thus defining the third epoch [44]. The so-called '12-to-18 month' search, described in this chapter, used the 186 days of S5 data recorded after the S51YR search concluded, but before VSR1 began [1]. In total there were $\sim 0.3\,\mathrm{yr}$ of data analysed as opposed to $\sim 0.7\,\mathrm{yr}$ in the S51YR search.

Unlike the S51YR search that analysed all of the data in one instance of the pipeline, the 12-to-18 search analysed each 'month'[10] of data independently. The detector behaviour varied over the course of the search, hence, analysing the data monthly allowed foreground triggers to be compared with background triggers that better reflected the behaviour at the time of the candidates. The results of 'month 1'[11] are described in detail in this section, along with the final results of the complete search.

Blind analysis and search tuning In order to avoid any biases that may be introduced by the data analysts, all tunable parameters, such as the SNR threshold, minimum match, the metric distance used for clustering etc. must be chosen before the foreground data is analysed. This process prevents the data analysts tuning the search on the basis of a trigger found in the foreground and is known as a blind analysis. However, roughly ten percent of the data is marked as 'playground' data, which are analysed at zero-lag to check that the pipeline performs as expected, produces reasonable results and that

---

[10] Four weeks of data.

[11] Month 1 was not the first month of the search, but the second. Sometimes, as in this case, physicists count from zero.

Parameter	Symbol	Value
Lower cut-off frequency	f_l	40.0 Hz
SNR threshold	ρ_*	5.5
Minimum match	M	0.97
Effective distance threshold	κ_*	0.6
Single IFO error ellipsoid	ϵ_f	0.06
e-thinca	ϵ_t	0.5
χ^2 veto threshold	ξ_*^2	10
number of χ^2 bins	n	16
r^2 threshold	r_*^2	16

TABLE 3.1: A selection of the tuned parameters used in the 12-to-18 search.

the data quality procedures are adequate. Alongside the playground data, the analysts are able to look at time-shifted data, as any coincident triggers cannot be true signals. The time shifted data can be used to check background rates and the playground analysis can be compared with these. The tuning of the signal based vetoes is achieved by performing the analysis with simulated signals added to the data, known as 'injection runs'.

As the pipeline used for the 12-to-18 search was nearly identical to the first year search, the playground analysis used the parameters as tuned for the first year search. There were no anomalies in the playground analysis or injection runs and therefore the tuned parameters were not altered. Figure 3.1 shows the separation of the software injections from the background using the χ^2 discriminator. The figure was made after the analysis was un-blinded and so also includes the foreground triggers, which are consistent with the background. Table 3.1 lists a selection of the tuned parameters.

3.4.1 Month 1: Data information and first stage analysis

Month 1 of the 12-to-18 search began on December 12th, 2006 and finished on January 9th, 2007 (849974770-852393970 GPS time). The quantity of data analysed, before and after the application of the vetoes, is listed in Table 3.2.

The data were divided into segments of length 2048 s for analysis. Each segment had a different PSD, according to the varying detector behaviour and the noise environment at the time the data was recorded. Thus the sensitivity of the search varied for each segment and can be expressed as the range (3.46), e.g., of a BNS system. Figures 3.2, 3.3 and 3.4 indicate the sensitivity of the detectors during month 1.

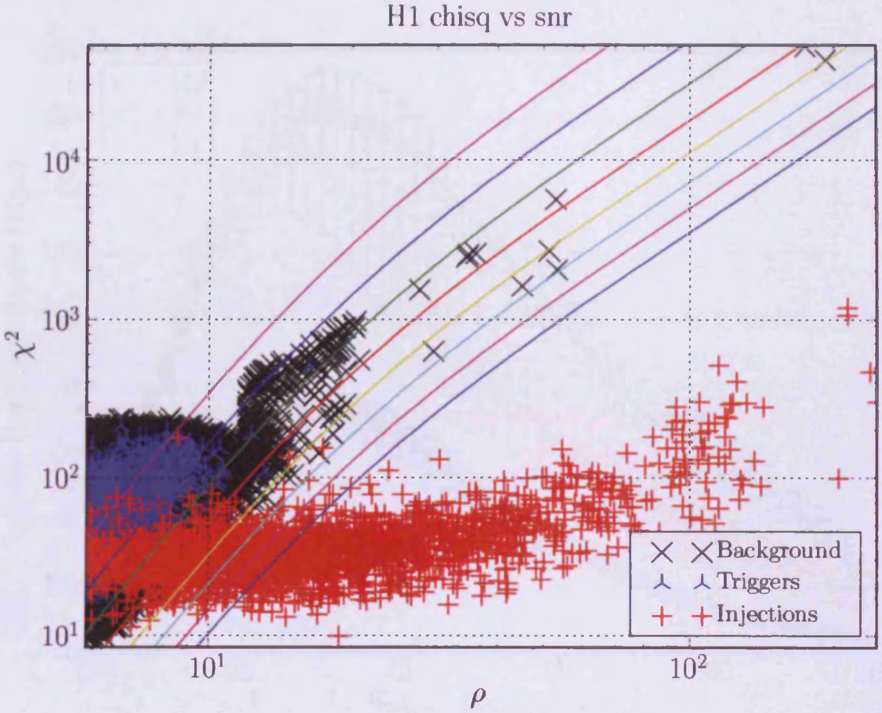

FIGURE 3.1: This plot of χ^2 vs. SNR shows how the effective SNR can be used to separate software injections from background triggers in H1. The coloured lines show contours of constant effective SNR. The sharp cutoff in the background triggers reflects the fact that there are two r^2 thresholds.

Interferometer	Science Segments (days)	After Cat 1	Cat 1,2	Cat 1,2,3	Cat 1,2,3,4
H1	19.8171	19.8156	19.1730	18.8534	14.2322
H2	21.5143	21.5125	19.8991	18.0748	13.4888
L1	21.0350	21.0254	20.8062	19.3211	18.8299

TABLE 3.2: The LIGO data recorded during month 1 of the 12-to-18 search. The duration is shown in days before and after data quality vetoes have been applied.

The data were initially sampled at 16384 Hz, but were reduced by down-sampling to 4096 Hz for analysis. Frequencies below 30 Hz are limited by the 'seismic wall' of LIGO's noise curve and are high pass-filtered during this process.

The data segments were chosen to overlap by 256 s, allowing the first and last 64 s of each segment to be discarded when matched filtering. Hence all of the data can be searched, without any corruption occurring due to the edge effects of wrapping the SNR time series.

The data were analysed in different categories according to which detectors were operating, denoted triple time (H1H2L1) when all three detectors are operating and double

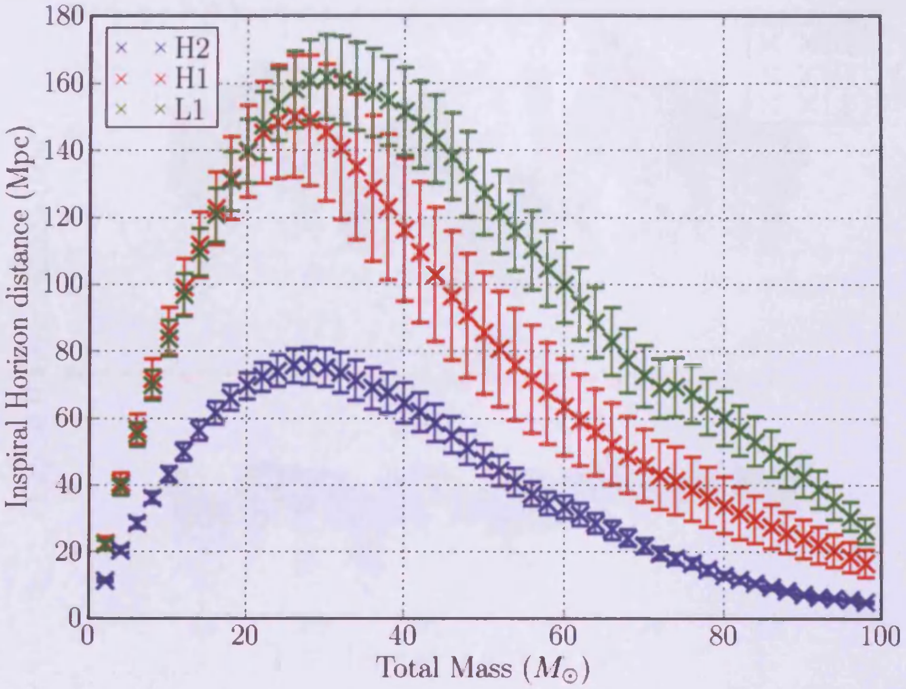

FIGURE 3.2: The inspiral-range (3.46) vs. mass for equal mass systems for each of the interferometers averaged over the course of month 1.

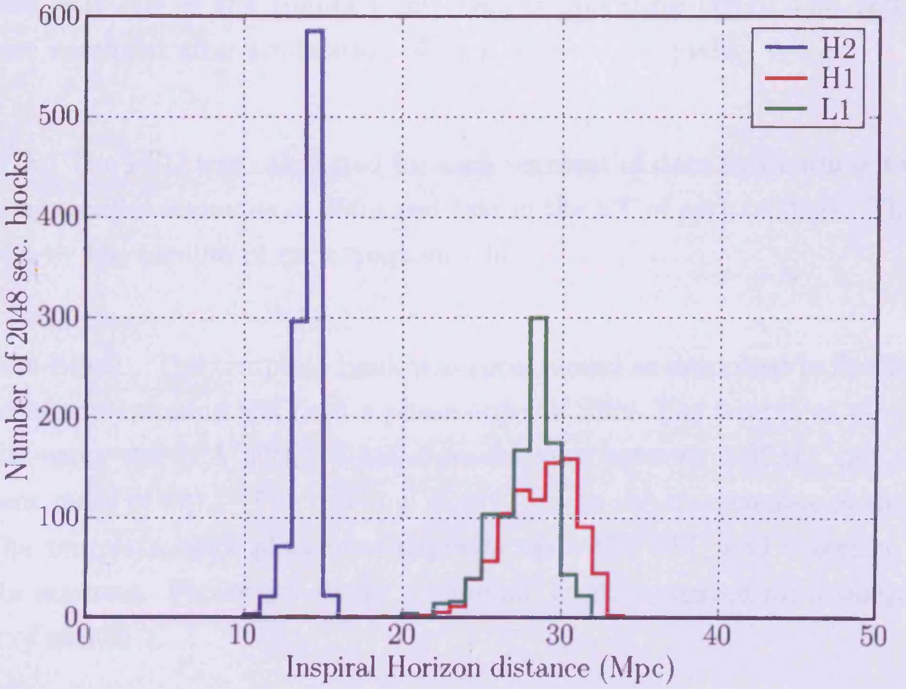

FIGURE 3.3: Histograms of the inspiral-range of a BNS system in each detector for month 1.

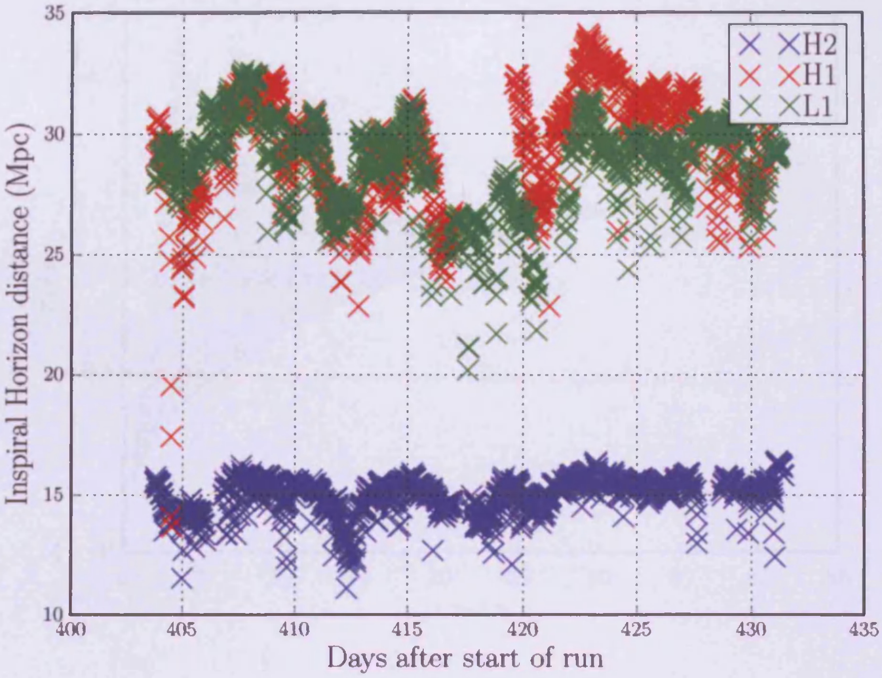

FIGURE 3.4: The inspiral-range of a BNS system plotted for each segment of data for month 1 of the 12-to-18 month search. N.B.: days after start of run refers to the start of S5.

time when only one of the Hanford detectors is operating (H1L1 and H2L1). These times were redefined after application of each of the data quality vetoes.

The PSD The PSD was calculated for each segment of data by dividing it into fifteen overlapping smaller segments of 256 s and taking the FT of each of these. The PSD was then given by the median of each frequency bin.

Template bank The template bank was constructed as described in Section 3.3.1. It consisted of non-spinning RWFs at a phase order of 2PN. The templates were generated in the FD using the SPA with a total mass range of between 2-35$M_\odot$ and a minimum component mass of $1M_\odot$. The minimal match due to the discreteness of the bank was 0.97. The template bank placement depends upon the PSD and therefore varied for each data segment. Figure 3.5 shows a template bank generated for a sample L1 data segment of month 1.

First stage triggers Figure 3.6 shows the number of triggers in H1 plotted against SNR after application of first stage trigger clustering. Figure 3.7 shows the number

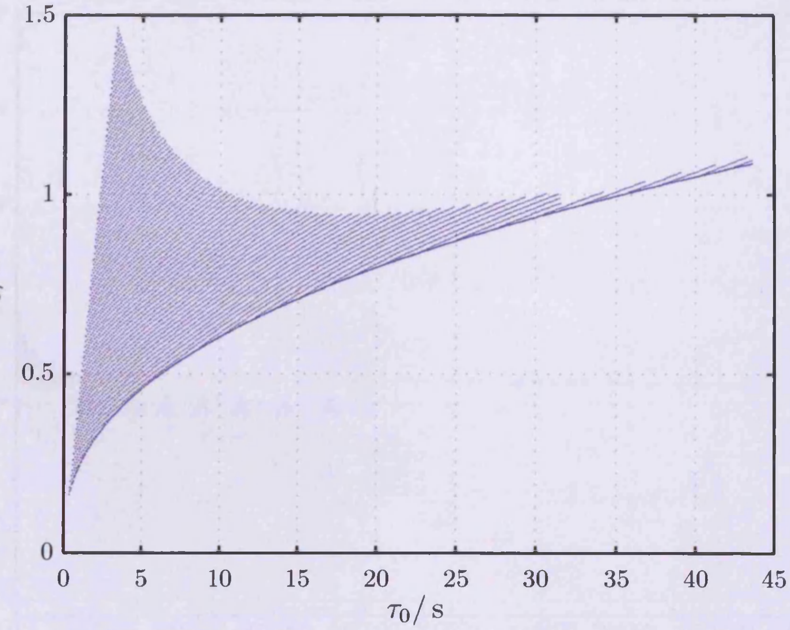

FIGURE 3.5: The template bank generated for a 2048 s L1 segment starting at 852351639 GPS time. There were 7477 templates in this bank.

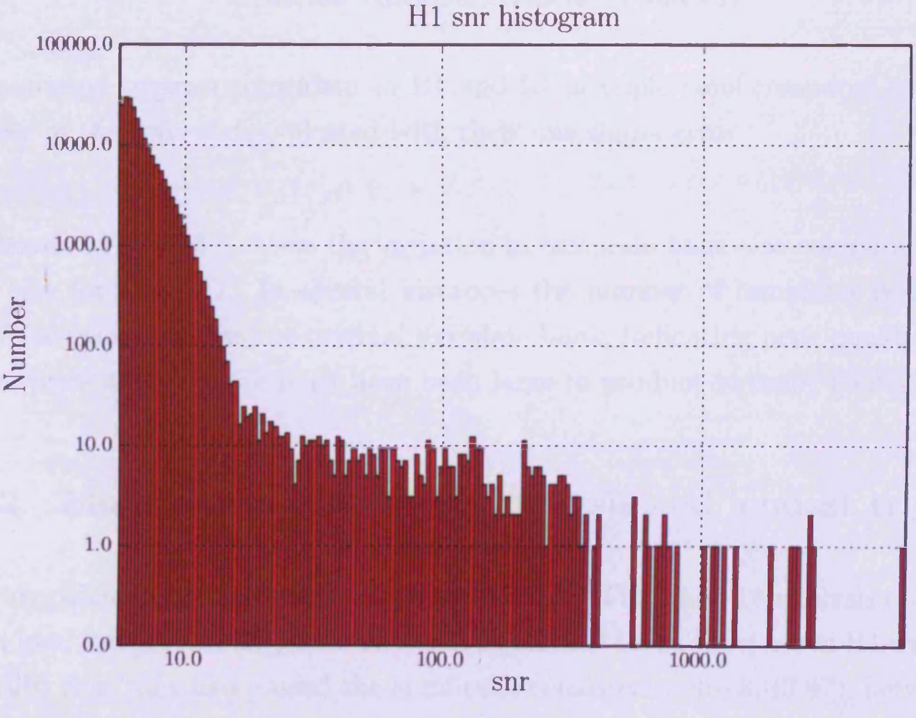

FIGURE 3.6: A histogram of the number of triggers vs. SNR for H1.

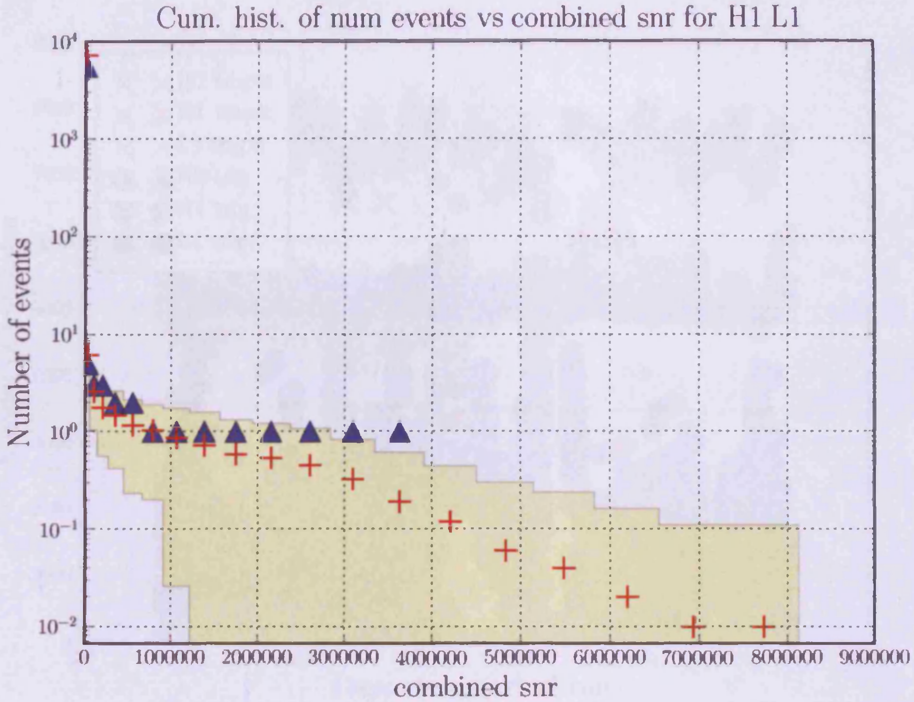

FIGURE 3.7: Histogram comparing foreground and background triggers coincident in H1 and L1 after the first stage analysis in triple time. The blue triangles show the foreground triggers, whereas the red crosses show the background triggers (with their one sigma errors shown as the yellow area. The combined SNR is the sum of squares of the individual SNRs in H1 and L1.

of foreground triggers coincident in H1 and L1 in triple time compared to the average number in the time-slides, plotted with their one sigma error.

Trigbank Figure 3.8 shows the variation in template bank size compared to the trigbank size for month 1. In several instances the number of templates in the trigbank are of the same value as the original template bank, indicating poor quality data as the trigger rates at first stage must have been large to produce so many coincident events.

3.4.2 Month 1: Second stage analysis and loudest triggers

The amplitude consistency check revisited The 12-to-18 analysis originally produced loud foreground triggers coincident in H2 and L1 at times when H1 was operating normally, thus they had passed the amplitude consistency check, (3.47), between H1 and H2. However, as H1 was typically twice as sensitive as H2, the maximum SNR for a trigger to be present in H2, but not H1, $\rho_{\max \text{H2}}$, was only just above threshold in H2. Using

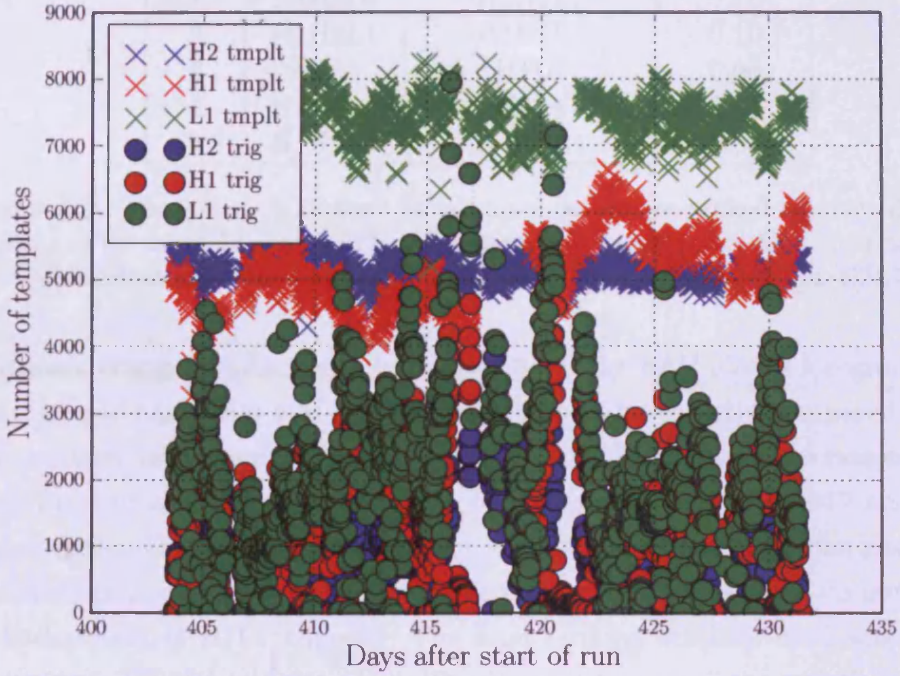

FIGURE 3.8: Template bank size compared to trigbank size for the data segments in month 1.

the horizon distances of each segment it was shown that $\rho_{\max\ \mathrm{H2}} > (\rho_* = 5.5)$, for just 12.9%, of the triple time during month 1. Further analysis showed that $\rho_{\max\ \mathrm{H2}} > 5.7$ for 3.7% of the time and $\rho_{\max\ \mathrm{H2}} > 6.0$ for 0.2%[12]. Hence we see that for an H2 trigger to pass the consistency check, it can only just be above the threshold. As H1 was operating normally it is intuitive to believe that the H2 triggers were due to the background and happened to be quiet enough to pass the consistency check whilst having similar parameters to an L1 trigger, or in other words, they were not due to a gravitational wave!

Furthermore, the percentages of times when an H2L1 trigger could occur in triple time varied for each of the time-slides (due to the L1 vetoes) producing poor background estimation and in some cases potentially elevating the ranking of an H2L1 trigger. The 12-to-18 analysis was rerun, but with a new cut that rejected *all* H2L1 triggers in triple time. This decision was made after the analysis was un-blinded, as it was considered to be changing a mistake with the original analysis rather than re-tuning the search. Hence in triple time, only H1H2L1 and H1L1 coincident triggers are considered.

---

[12] These times were calculated before the application of data quality vetoes. This means that the true percentages would differ.

Rank	IFO Time	Coincident Type	IFAR /yr
1	H1H2L1	H1H2L1	0.16
2	H1H2L1	H1H2L1	0.10
3	H1L1	H1L1	0.08
4	H1H2L1	H1L1	0.03
5	H1H2L1	H1H2L1	0.03

TABLE 3.3: The 5 loudest triggers for all mass categories ranked by their IFAR for month 1 of the 12-to-18 search. The coincident type refers to whether the trigger was coincident in all three detectors (H1H2L1) or in just two (H1L1/H2L1)

The loudest triggers As stated in Section 3.3.9 the FAR allows foreground triggers of different mass categories and IFO combinations to be directly compared. In the 12-to-18 search templates were categorised by their chirp mass into three ranges defined by the chirp mass of *equal* mass systems of a total mass between 2-8, 8-17 and 17-35$M_{\odot}$. When calculating the detection statistic for triple time data, triple coincidence triggers are separated from double coincidence triggers, i.e., H1H2L1 triggers do not contribute to the background of H1L1 triggers. The final ranking statistic used was the inverse false alarm rate (IFAR) in units of yr. The loudest trigger of the month had an IFAR of 0.16 yr, meaning that a trigger equally as loud can be expected due to background in every 0.16 years of data[13]. A summary of the loudest triggers in month 1 is listed in Table 3.3.

Figure 3.9 shows the cumulative number of foreground triggers in H1H2L1 time against IFAR for month 1. The triggers are marked as blue triangles. The dashed black line is the expected background plotted with one and two sigma error regions. The expected background is simply the IFAR normalised to one year, i.e., in one year we would expect one event in the background with an IFAR of 1. After application of category vetoes 1-3 there were 10.5 days of H1H2L1 data in month 1. Therefore one would expect the loudest background event to have an IFAR of $10.5/365.25 \sim 0.03$ yr. The background events from the time slides are also plotted as grey lines. The loudest event was above the expected background for month 1, although not significantly enough so to be of any interest; it is within the 2-sigma background errors and quieter than several of the background trials. Moreover it was also the loudest event of the entire 12-to-18 search in which there were 0.21yr of H1H2L1 data[14], which places the loudest trigger slightly below the expected background of the complete search and within one sigma.

---

[13] Equivalent livetime.

[14] Therefore the IFAR of the loudest expected background event is 0.21 years.

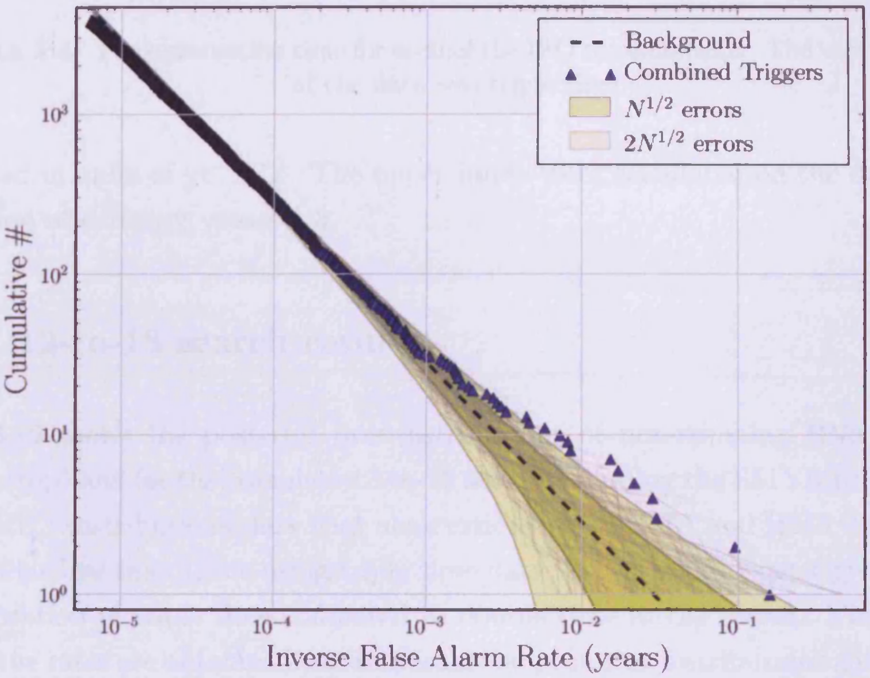

FIGURE 3.9: The loudest triggers of month 1 analysed after application of data quality vetoes 1,2 and 3.

3.5 Upper limits

The 12-to-18 search calculated rate upper limits for coalescing binaries consisting of neutron stars and/or black holes assuming BNS systems of $m_1 = m_2 = (1.35 \pm 0.04)\,M_\odot$; BBH systems consist of $m_1 = m_2 = (5 \pm 1)\,M_\odot$; and NSBH systems consist of $m_1 = (5 \pm 1)\,M_\odot$ and $m_2 = (1.35 \pm 0.04)\,M_\odot$. For BBHs the upper limits were also calculated as a function of the total mass of the binary and, for NSBH binaries, as a function of the black hole mass. The effects due to the spin of the sources visible to LIGO are expected to be negligible for BNS waveforms [45, 46], and limited for black holes. The main results of the search were therefore presented assuming non-spinning sources, however, the upper limits were also calculated for spinning black holes, assuming their spin is uniformly distributed between zero and a maximal value of m^2, in accordance with theoretical limitations.

The posterior rate distributions were calculated for each month of the 12-to-18 search separately using a uniform prior. These results were then combined to produce final posterior rate distributions, using the S51YR search results as the prior, from which the 90% confidence rates were calculated. As described in section 3.3.10, the sensitivity of the search is measured using the cumulative luminosity, hence the rate upper limits

IFO combination	H1H2L1	H1L1	H2L1
Observation time / yr	0.21	0.02	0.01

TABLE 3.4: The observation time for each of the IFO combinations. The vast majority of the data was triple time.

are quoted in units of $\mathrm{yr}^{-1}\mathrm{L}_{10}^{-1}$. The upper limits were calculated on the data after the application of category vetoes 1-3.

3.5.1 12-to-18 search results

Figure 3.10 shows the posterior rate distributions of non-spinning BNS systems for month 1 (top) and for the complete 12-to-18 search including the S51YR prior (bottom). The month 1 distributions show that observations using H1L1 and H2L1 data constrain the rates far less than those using triple time data, as we would expect given the much larger duration of triple time compared to double time in the search. The 90% upper limit on the rates are obtained by normalising the posterior distributions and integrating to 0.9. However, Figure 3.10 shows the non-normalised distributions so that each curve can be compared qualitatively. In the bottom plot of Figure 3.10, each month is listed in the legend in the order that it appears from top to bottom, or rather in the order of least constraining to most constraining. We see that month 1 was in fact the 'worst' month of the search, due to poorer data quality. The latter months are the most constraining on the rates as they consisted of the best quality LIGO data of S5 (prior to VSR1). It is interesting to see that although the S51YR result is far better than any of the months individually, the combined upper limit is considerably improved with the additional 12-to-18 data.

Table 3.4 shows the quantity of data for each of the IFO times and Table 3.5 shows the marginalised 90% rate upper limits, the range (averaged over the time of the search) and the cumulative luminosity to which the search was sensitive above the loudest event for times when all three LIGO detectors were operational. The first set of upper limits are those obtained for binaries with non-spinning components. Finally, as the rates for systems containing black holes vary considerably depending on the mass choice, Figure 3.11 shows the marginalized 90% rate upper limits as a function of mass for BBH (top) and NSBH systems (bottom). In the former case, the 90% upper limits on the rates are plotted against the total mass of the system, whereas for the latter the neutron star mass is assumed to be $1.35M_{\odot}$ and the 90% upper limits are plotted against the black hole component mass. The mass dependent upper limits were calculated using only H1H2L1 data since the relatively small amount of H1L1 and H2L1 data made it difficult to evaluate the cumulative luminosity in the individual mass bins. Therefore,

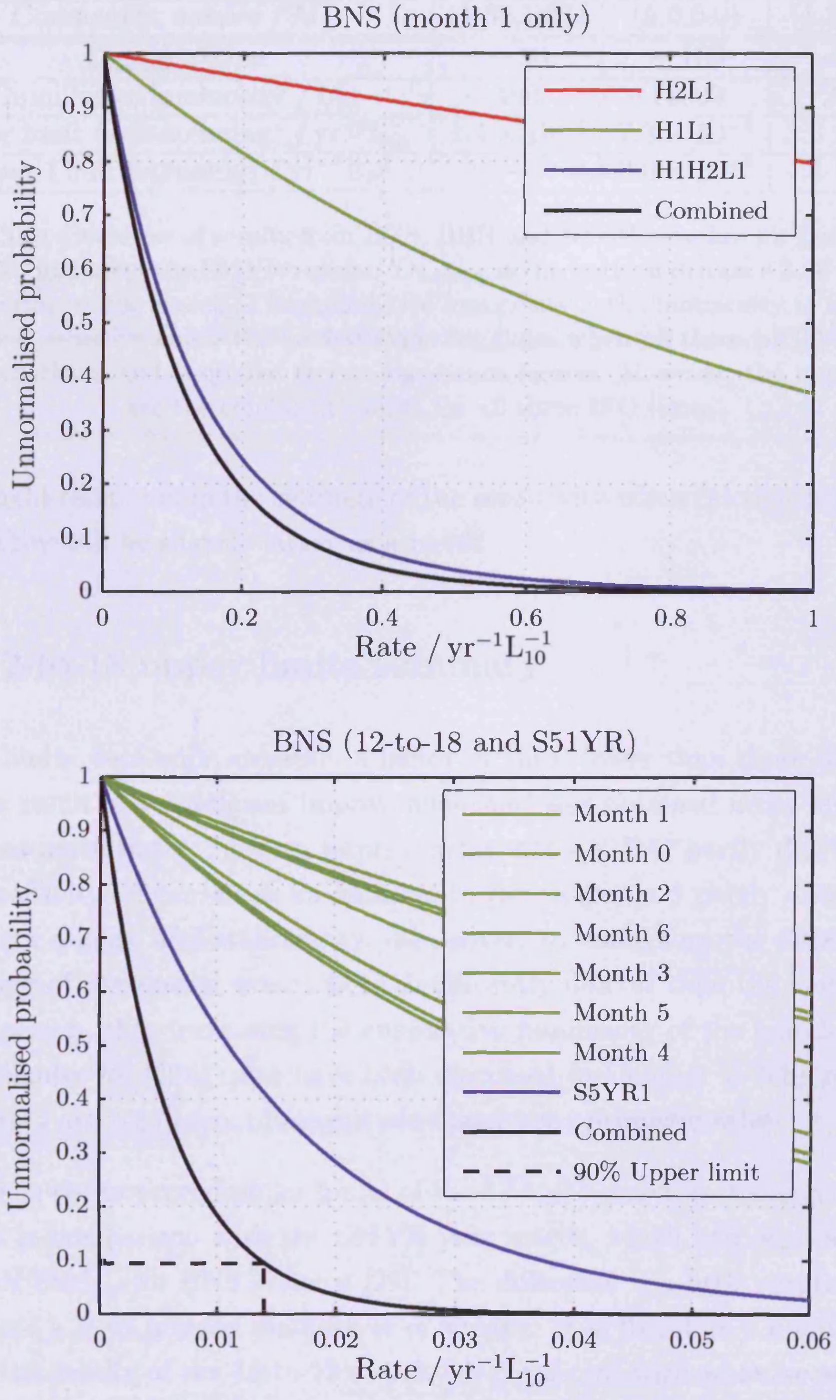

FIGURE 3.10: The BNS posterior distribution of the rates of coalescing BNS systems, neglecting spin, for month 1 (top) and for the entire 12-to-18 search (bottom). In the top figure we see that H1H2L1 data constrains the rates better than double time data. The bottom plot shows the contributions of each of the months (green - listed in the legend in the order that they appear from top to bottom on the plot). We see that month 4 was the 'best' and that month 1 was the 'worst'. The S5YR1 result is shown in blue and the complete S5 result is shown in black.

Component masses / $M_\odot$	(1.35,1.35)	(5.0,5.0)	(1.35,5.0)
D_{horizon} / Mpc	~ 30	~ 100	~ 60
Cumulative luminosity / L_{10}	490	11000	2100
Upper limit (non-spinning) / $\mathrm{yr}^{-1}\mathrm{L}_{10}^{-1}$	1.4×10^{-2}	7.3×10^{-4}	3.6×10^{-3}
Upper Limit (spinning) / $\mathrm{yr}^{-1}\mathrm{L}_{10}^{-1}$	–	9.0×10^{-4}	4.4×10^{-3}

TABLE 3.5: Overview of results from BNS, BBH and NSBH searches for the 12-to-18 search [1], including the S51YR results. D_{horizon} is the horizon distance 3.46 averaged over the time of the search. The cumulative luminosity is the luminosity to which the search was sensitive above the loudest event for times when all three LIGO detectors were operational and is quoted to two significant figures. However, the upper limits are the combined results for all three IFO times.

there is a slight reduction in the estimate of the sensitivity when calculating these upper limits and they will be slightly larger as a result.

3.5.2 12-to-18 upper limits summary

The upper limits were approximately a factor of three lower than those of the S51YR search. The result is a significant improvement and was obtained using approximately two thirds as much data. Such an improvement was possible partly due to improved detector sensitivity, measured as an increase in the range, and partly due to improvements in data quality and stationarity. Moreover, by analysing the data in separate months, many of the loudest events were significantly quieter than the loudest event of the S51YR search, thus increasing the cumulative luminosity of the search. The astrophysical estimates for CBC rates have been discussed in Chapter 2. The results of the 12-to-18 search are 1-2 orders of magnitude above the optimistic rates.

A key factor in the improved upper limits of the 12-to-18 search is the larger cumulative luminosities in comparison with the S51YR year search, which had, e.g., a cumulative luminosity of 250 L_{10} for BNS systems [29]. The difference is a little surprising as both searches quote a BNS horizon distance of ~ 30 Mpc. It is therefore a useful exercise to verify that the results of the 12-to-18 search are consistent with what we would expect given the duration of the search, the range and the loudest events.

We will first estimate the cumulative luminosity using the horizon distance. We note that the horizon distances given in Table 3.5 are quoted to one significant figure. In fact many of the months of the search had a horizon distance of ~ 33 Mpc. For a given month, we use that slightly larger range to approximate a distance, D_c, up to which the

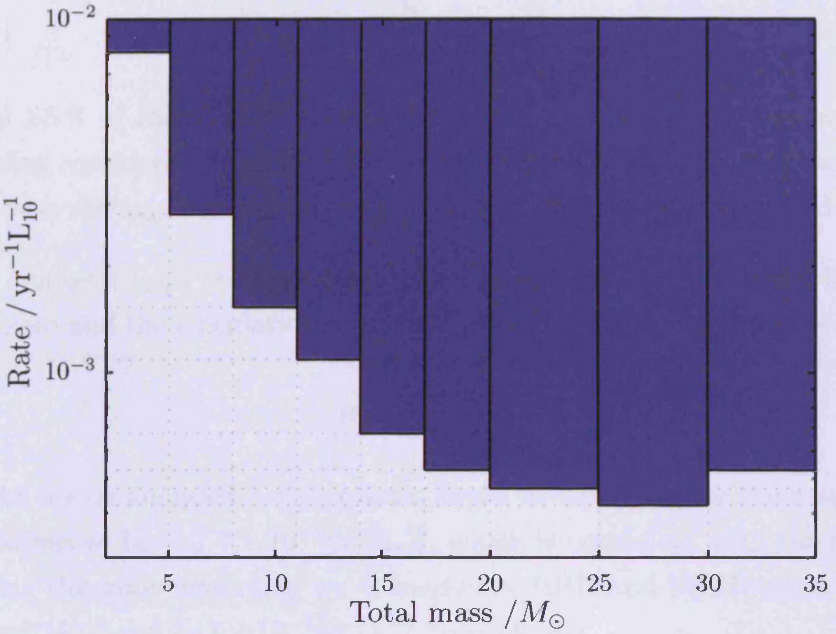

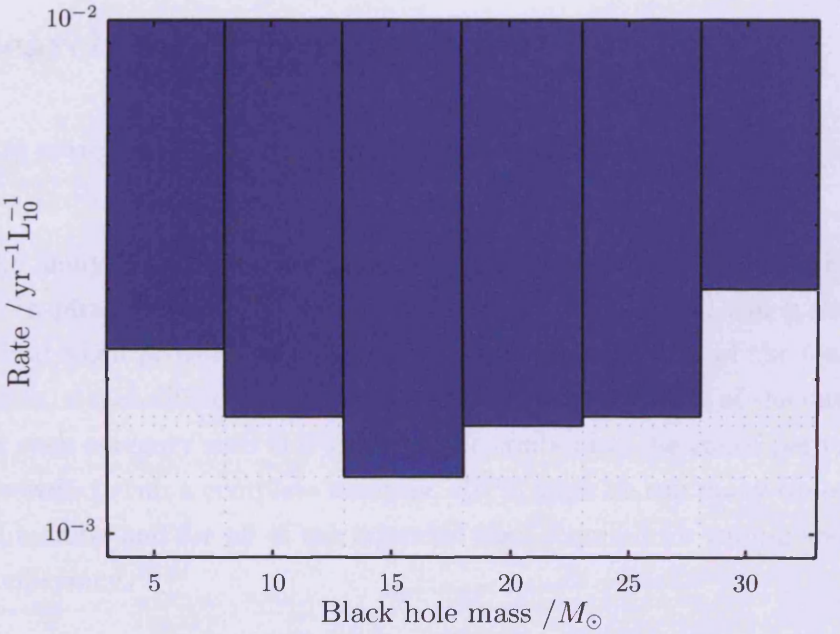

FIGURE 3.11: Top: The 90% upper limit for non-spinning BBH systems vs. total mass. Bottom: The 90% upper limit for non-spinning NSBH systems vs. black hole component mass assuming a neutron star mass of $1.35M_\odot$

search was sensitive using the SNR of the loudest event, ρ_m,

$$D_c = \frac{8}{\rho_m} D_{\text{horizon}}\,. \tag{3.53}$$

The typical SNR of the loudest event in each month was ~ 6.5, thus we find $D_c \sim 40\,\text{Mpc}$. Using equations (4) and (5) of [31] we find the cumulative luminosity for BNS systems to be $\sim 460\,\text{L}_{10}$, which is a reasonable match with the result quoted in Table 3.5.

Where the loudest trigger is demonstrably due to background, the signal likelihood, Λ, is equal to zero and the calculation of the 90% upper limit on the rates is simplified to

$$\alpha_{90} = \frac{2.303}{C_L T}\,. \tag{3.54}$$

The 12-to-18 search analysed $\sim 0.3\,\text{yr}$ data, hence we approximate the rate upper limit for BNS systems to be $\sim 1.7 \times 10^{-2}\text{yr}^{-1}\text{L}_{10}^{-1}$, which is consistent with the results of the search. Using the same reasoning, we estimate the BBH and NSBH upper limits to be $\sim 6 \times 10^{-4}\text{yr}^{-1}\text{L}_{10}^{-1}$ and $\sim 3 \times 10^{-3}\text{yr}^{-1}\text{L}_{10}^{-1}$ respectively.

3.6 Search automation: ihope

The 12-to-18 search used an automated pipeline called ihope - *"I hope it works"*.

ihope The analysis pipeline (see Section 3.3) was run with an executable called the Heirachical-Inspiral-Pipeline-Exectuable (HIPE) [47]. HIPE will run a single instance of the pipeline when provided with the GPS start and end time of the search, a list of data segments, a cache file containing information of the location of the data files, a list of times for each category veto and an input file containing the tuned parameters of the search. However, to run a complete analysis, HIPE must be run many times to generate playground results, and for all of the injection runs required for tuning and calculating the search efficiency.

ihope was designed to automate the entire process, enabling a search to be run just by providing the GPS times and the input options. ihope is under constant development, but at the time of the 12-to-18 search it did the following:

1. Downloaded a list of GPS containing information regarding when data category vetoes should be applied from a provided server.
2. Generated lists of data segments to be analysed.

3. Set up all the required instances of HIPE.
4. Set up instances of other executables to produce tuning and result plots.
5. Created a direct acrylic graph (DAG) file that allows all of the data analysis jobs to be run in parallel using Condor[15] [48].

Automation of the pipeline allowed the analysis to be broken into months with the confidence that each month was run in the same way, without human error. Dividing the search into months meant that foreground triggers were compared to background triggers that better reflected the behaviour of the interferometers at the time, as opposed to the S51YR search where the entire year of the search was used to estimate the background. Indeed, the behaviour of the detectors did vary over the search, which is why the analysis of month 4 constrained the upper limit more than that of month 1 (see Figure 3.10).

ihope results page In order to collate all of the results ihope generates an automated web page that catalogs all of the relevant information about a run and all of the tuning and results plots[16]. ihope was first run with playground and injections only to check the tuning of the parameters. The analysis group then used the web pages to decide whether the analysis should be un-blinded. Figure 3.12 shows the ihope results page for month 1. On the left there are links for all relevant information, including the injection runs. This page was made after the analysis was un-blinded and, therefore, includes the 'Full Data' result plots.

3.7 Concluding remarks - is this the best way to search for gravitational waves?

The title of this chapter, 'How to search for gravitational waves from CBCs', may lead the reader to believe that he/she is in possession of an authoritative instruction manual. Yet it cannot be claimed that the search method presented here is optimal. For instance, the core of the search lies with the matched filter, but that is derived under the assumption that the noise is stationary and Gaussian, which is simply not the case with real detector data. How much of an impact does that have on the search? We also see the use of binning the template bank into different mass regions that are then treated

---

[15] A management program for scheduling and managing distributive computing tasks.

[16] At the time the IFAR detection statistic was not included in ihope and the final results available on the web page were ranked by the effective SNR.

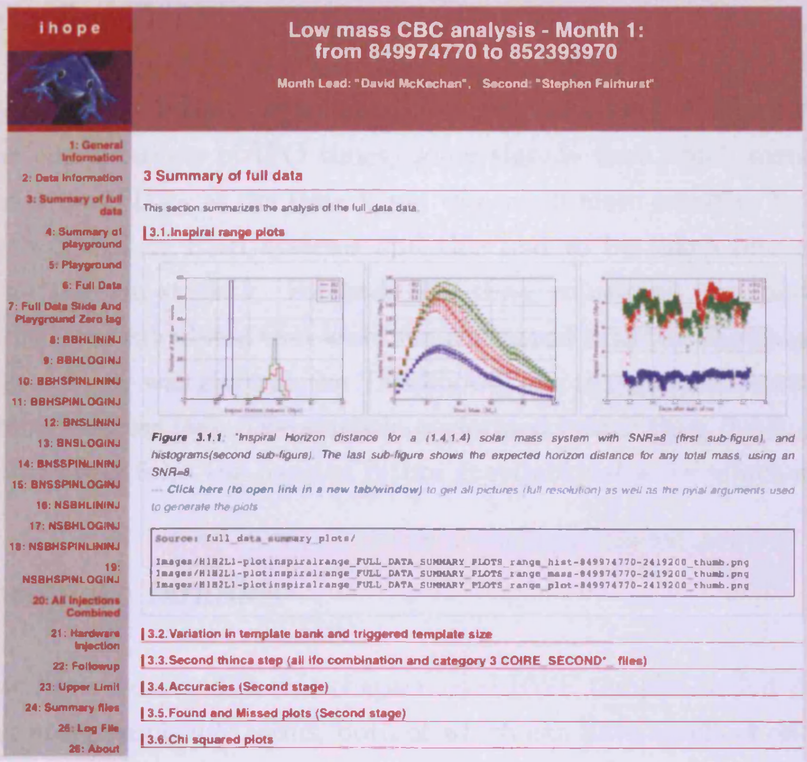

Low mass CBC analysis - Month 1:
from 849974770 to 852393970

Month Lead: "David McKechan", Second: "Stephen Fairhurst"

3 Summary of full data

This section summarizes the analysis of the full_data data.

3.1.Inspiral range plots

Figure 3.1.1: "Inspiral Horizon distance for a (1.4,1.4) solar mass system with SNR=8 (first sub-figure), and histograms(second sub-figure). The last sub-figure shows the expected horizon distance for any total mass, using an SNR=8.

--- Click here (to open link in a new tab/window) to get all pictures (full resolution) as well as the pylal arguments used to generate the plots

```
Source: full_data_summary_plots/

Images/H1H2L1-plotinspiralrange_FULL_DATA_SUMMARY_PLOTS_range_hist-849974770-2419200_thumb.png
Images/H1H2L1-plotinspiralrange_FULL_DATA_SUMMARY_PLOTS_range_mass-849974770-2419200_thumb.png
Images/H1H2L1-plotinspiralrange_FULL_DATA_SUMMARY_PLOTS_range_plot-849974770-2419200_thumb.png
```

3.2.Variation in template bank and triggered template size

3.3.Second thinca step (all ifo combination and category 3 COIRE_SECOND*_ files)

3.4.Accuracies (Second stage)

3.5.Found and Missed plots (Second stage)

3.6.Chi squared plots

FIGURE 3.12: The automated ihope results page for month 1.

as equally likely when compared with their own backgrounds. Does that really account for the likelihoods of detection of different templates or the various combinations of IFO times? Furthermore, the templates do not include the effects of spin or higher order amplitude terms, how does that affect detection efficiencies? What are the limitations of the search pipeline presented here and what can be done to improve it?

3.7.1 Gaussian data

Although it is known that real detector data are non-Gaussian (see Section 3.3.7 for instance), the effects have not been quantified before. Recently, Robinson et al. have compared a week of LIGO data (month 4 of the 12-to-18 search) post category 4 vetoes with Gaussian data by running the pipeline on both [49]. The results promise to be interesting and show that although in many stages of the pipeline, e.g., template reduction, first stage triggers etc., the LIGO data is clearly far from Gaussian in behaviour, the pipeline performs reasonably well in comparison. This suggests that if data quality methods, e.g., vetoes and detector characterisation, are highly robust the non-Gaussian aspect of real data may not be too much of a hindrance in the search for gravitational waves. However, month 4 consisted of some of the best data of S5.

3.7.2 Likelihood

In the first joint LIGO-Virgo search, the differences between the detectors meant that for particular combinations of IFO times, some signals were much more likely to be detected than others. E.g., at the time Virgo was much more sensitive to BNS systems than it was to NSBH or BBH systems and this had to be taken into account when formulating a detection statistic. For each IFO time, coincident type and mass bin an 'efficiency factor' was calculated that was then compared with the background rate. The final detection statistic was given as the 'Likelihood' of a trigger based on its background rate and efficiency factor [44]. The statistic performed better than IFAR and a method of this kind will likely form the basis of future gravitational wave searches.

3.7.3 Template families

The search we have described in this chapter used RWF templates that do not include spin or higher order amplitude terms, both of which can have an effect on the detection efficiency and parameter estimation. The use of higher order waveforms is discussed in the following chapter. Upper limits were calculated for spinning black holes and are not significantly larger than for the non-spinning case, so it is not clear how much an improvement can be gained by incorporating spin. However, spin has been included in LIGO data analysis previously [50] and there are several studies on the inclusion of spin and its benefits [51–53].

Chapter 4

Higher order waveforms in data analysis

In this chapter, we will study the use of the FWF in gravitational wave data analysis. In Chapter 3 we saw that waveform models may be used as both injections and templates in the search for gravitational waves from CBCs. The use of the FWF for injections presents no complications and, indeed, it has been shown that using the RWF for injections, rather than FWF, can significantly overestimate the SNR [54], which could arguably lead to artificially lower upper limits on the rate of CBCs[1]. On the other hand, the use of the FWF for templates when matched filtering is not straightforward. One can no longer use the matched filter as presented in (3.31), since the maximisation is derived for templates of the form (3.19).

We begin with a brief overview of the motivations behind using FWF templates in gravitational wave searches, whilst the rest of the chapter presents in detail the development and results of a matched filtering algorithm that uses FWF templates of 0.5PN in amplitude.

N.B.: throughout this chapter we shall drop the convention that Latin indices run over $1, \ldots, 3$.

---

[1] If nature's gravitational waves are better represented by the FWF then one would overestimate the search efficiency and consequently the cumulative luminosity would also be overestimated, hence reducing the upper limit.

4.1 Motivations

4.1.1 Mass reach

When considering inspiral-only waveforms, the mass reach of a detector, in terms of the total mass of the binary, *may* be determined by the FLSO and the detector's lower cut-off frequency. For example, LIGO is dominated by seismic noise below 40 Hz [7] and therefore is not considered sensitive to binary systems with an FLSO below that frequency. Using the FLSO, the theoretical mass reach of LIGO, is $\sim 100M_\odot$; such a system has an FLSO of ~ 43 Hz. However, when the binary reaches its ISCO, the higher harmonics contain power at frequencies greater than the FLSO, albeit at lower amplitudes. Nevertheless, including higher harmonics can still be significant, particularly for advanced detectors. The FLSO scales linearly with the PN order, k, of the waveform,

$$f_{LSO} = (k+1)\, f_0(M_T)\,, \tag{4.1}$$

where f_0 is the FLSO of the dominant harmonic. It can be shown that the detector's mass reach scales in the same manner. Thus if waveforms of 0.5PN in amplitude are considered, LIGO's mass reach extends to $\sim 150M_\odot$; at 3PN it theoretically extends to $400M_\odot$ [2].

The expectation value of the SNR for a signal in stationary Gaussian noise, where the signal and template match exactly, may be calculated as

$$\langle h, h\rangle = 4\int_{f_L}^{f_{ny}} \frac{|\tilde{h}(f)|^2}{S_n(f)} df\,, \tag{4.2}$$

where f_{ny} is the nyquist frequency and f_L is the lower cut-off frequency chosen, such that the contribution to the SNR from frequencies $f < f_L$ would be negligible. Figure 4.1 shows $\langle h, h\rangle$, calculated using the Advanced LIGO PSD [56], assuming a lower cut-off frequency of 20 Hz, plotted against total mass for both the RWF and the FWF (2PN). The SNRs of the two waveforms agree until $\sim 40M_\odot$, but thereafter the contribution of the higher harmonics leads to a larger SNR for the FWF. In this example the SNRs are well above any realistic detection threshold, but, because the SNR scales linearly with effective distance, one can chose any value of ρ_* to see how the mass reach is extended:

---

[2] N.B.: we are considering inspiral-only waveforms with which it would not be appropriate to study CBC systems of such high mass, as the inspiral stage would contain only a few cycles in the LIGO's sensitive band; essentially the template may look like a glitch. To study high mass systems, IMR waveforms, that include the merger and ringdown of the CBC, should be used. Indeed, a recent study indicates that IMR waveforms should be used in data analysis for systems as low as $12M_\odot$ [55]. However, the motivation that including higher harmonics extends a detector's mass reach also applies to IMR waveforms.

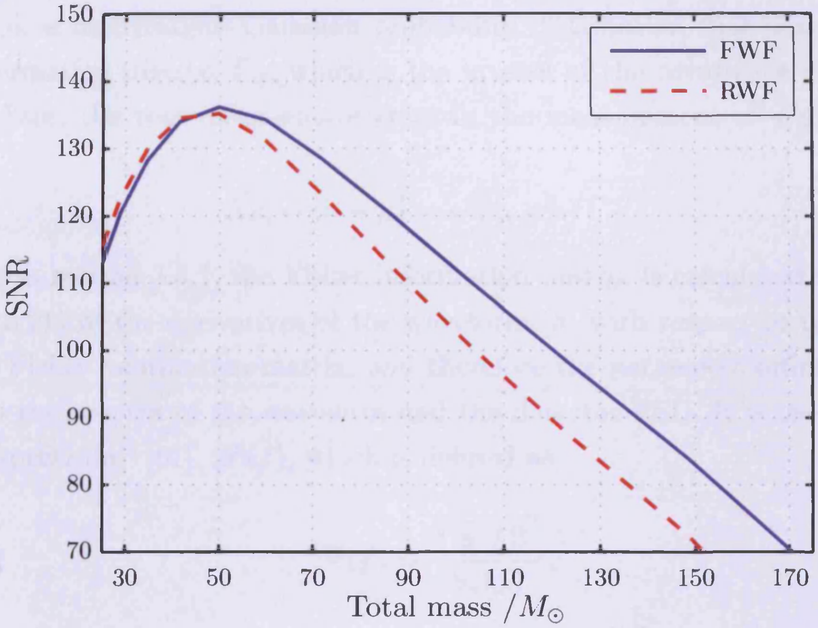

FIGURE 4.1: SNR vs. mass for both the RWF and FWF in Advanced LIGO The signals are overhead the detector at a distance of 100 Mpc, with a constant mass ratio of 1 : 4 and inclination angle of 45°.

here, at an SNR of 70, the mass reach of Advanced LIGO is extended from $\sim 150M_\odot$ to $\sim 170M_\odot$. The expected SNR for the FWF is slightly less than that of the RWF at lighter values of total mass. This effect is due to the contributions from the different amplitude orders in the FWF interfering with each other. As the total mass increases, the RWF has less power in the detector's sensitive frequency band. Hence, the higher harmonics in the FWF lead to a greater SNR.

4.1.2 Parameter estimation

When performing a gravitational wave search, one has a family of templates defined by a set of parameters μ_i. In the case of detection, the signal will have parameters $\widetilde{\mu}_i$, which will differ from the measured parameters, $\hat{\mu}_i$. The measurement error is caused by differences between the templates and nature's gravitational waves and the discreteness of the template bank. Moreover, the presence of noise will cause a measurement error even if the signal exactly matches one of the templates. There have been several studies that compare the ability to recover the intrinsic and extrinsic parameters of CBC when using FWF templates as opposed to RWF [57–61]. The usual approach to estimate the uncertainty in the measured parameters is to use the covariance matrix formalism, first applied in this context by Finn and Chernoff [62]. At large SNRs, the measurement errors follow a multivariate Gaussian probability distribution that depends upon the Fisher information matrix, Γ_{ij}, which is the inverse of the covariance matrix, C_{ij}. In this formalism, the root-mean-square error in the measurement of a parameter μ_i is given by,

$$\Delta\mu_i = \tilde{\mu}_i - \hat{\mu}_i = \sqrt{C_{ii}} = \sqrt{\Gamma_{ii}^{-1}}\,. \tag{4.3}$$

As we saw in section 3.3.1, the Fisher information matrix is calculated from the inner products (3.21) of the derivatives of the waveform, h, with respect to the parameters. Hence the Fisher information matrix, and therefore the parameter estimation, will depend upon the spectra of the waveform and the detector PSD. It is useful to plot the 'observed spectrum'[3] [61], $\mathscr{P}(f)$, which is defined as

$$\mathscr{P}(f) = \frac{f|\tilde{h}(f)|^2}{S_h(f)}\,, \tag{4.4}$$

and bears a direct relation to the way that a waveform is seen by a detector, dependent on the sensitivity and the waveform itself. Figure 4.2 shows the observed spectra for the RWF and the FWF (2PN), overhead Advanced LIGO for two different choices of total mass. In both cases it is clear that the spectra of the FWF contains more structure, which is due to the interaction of the different harmonics. This structure leads one to expect an improvement in parameter estimation under the covariance matrix formalism when using the FWF.

Van Den Broeck and Sengupta calculated measurement errors using (4.3) for various intrinsic and extrinsic parameters using the SPA FWF at 2.5PN in amplitude and phase, with promising results [61]. E.g., they found that in Advanced LIGO the error in time-of-coalescence (arrival-time) may reduce by a factor of five compared to the RWF at low masses and by a much larger factor at high masses. Furthermore, the individual component masses of the binary are expected to be found with errors as low as a few percent in Advanced LIGO, as opposed to being poorly determined by the RWF.

In the lower plot of Figure 4.2, the FWF contains significant power at frequencies beyond the FLSO of the RWF (40 Hz), demonstrating how the mass reach of a detector may be extended with the FWF.

---

[3] The SNR contribution per logarithmic frequency bin for a given PSD.

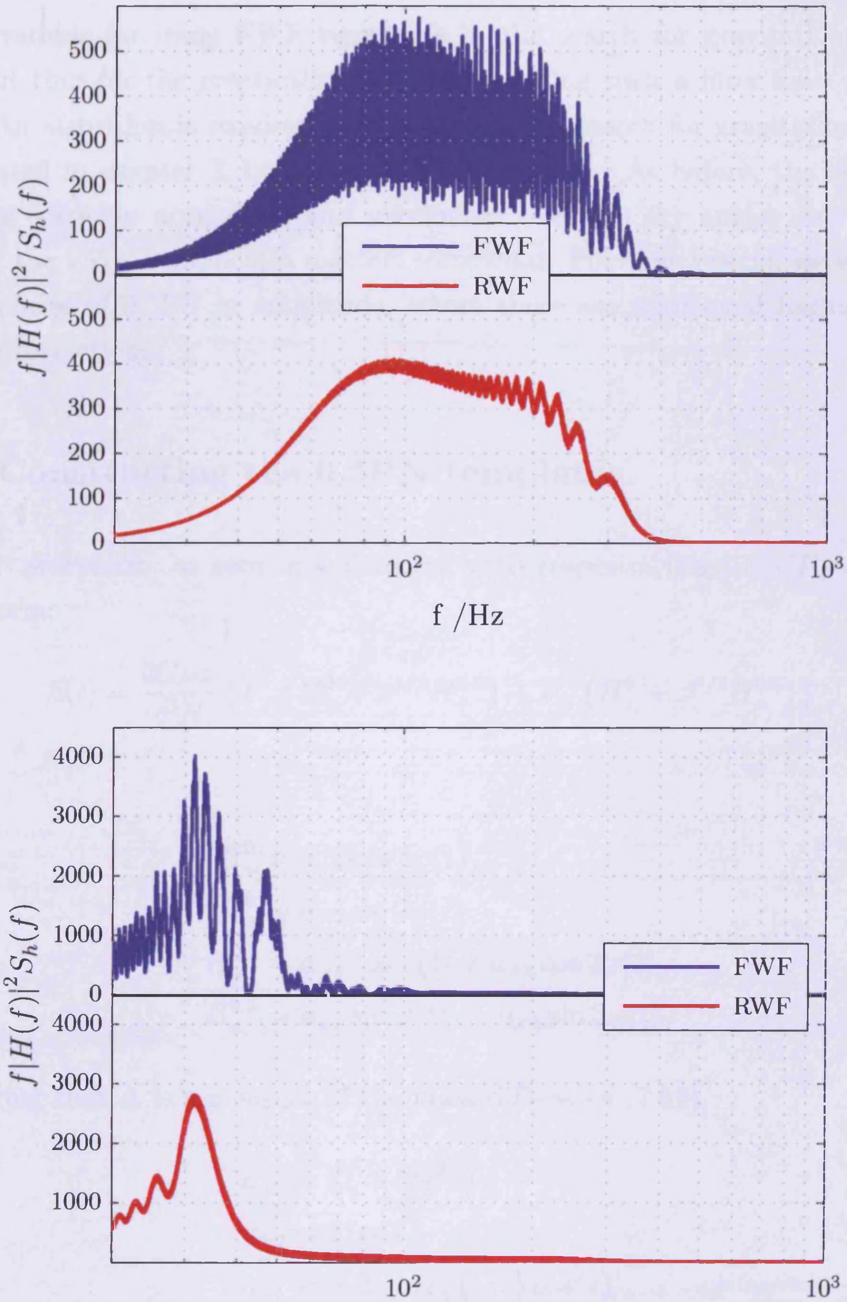

FIGURE 4.2: A comparison of the observed spectra for CBC waveforms overhead an Advanced LIGO detector, with component masses (1,10)$M_\odot$ [top] and (10,100)$M_\odot$ [bottom]. The sources are at a distance of 100 Mpc and have an inclination angle of 45°.

4.2 Developing a filter

The motivations for using FWF templates in the search for gravitational waves are strong, but thus far the practicalities of implementing such a filter have not been addressed. An algorithm is required that allows one to search for gravitational waves, as demonstrated in chapter 3, but using FWF templates. As before, the templates will need to be correctly normalised and maximised over the sky angles etc. As we shall see, use of the FWF complicates matters somewhat. For that reason, we will only consider templates of 0.5PN in amplitude, where there are additional harmonics but no amplitude corrections.

4.2.1 Constructing the 0.5PN templates

The 0.5PN waveform, as seen in a detector with response functions F_+ and $F_\times$, will take the form:

$$h(t) = \frac{2G\mu x}{c^2 R} \left\{ F_+ \left(H_+^0 + x^{1/2} H_+^{0.5} \right) + F_\times \left(H_\times^0 + x^{1/2} H_\times^{0.5} \right) \right\} , \tag{4.5}$$

where

$$H_+^0 = a_{+2} \cos 2\varphi(t) \,, \tag{4.6a}$$

$$H_\times^0 = a_{\times 2} \sin 2\varphi(t) \,, \tag{4.6b}$$

$$H_+^{0.5} = a_{+1} \cos \varphi(t) + a_{+3} \cos 3\varphi(t) \,, \tag{4.6c}$$

$$H_\times^{0.5} = a_{\times 1} \sin \varphi(t)) + a_{\times 3} \sin 3\varphi(t) \,, \tag{4.6d}$$

and, recalling that Δ is a measure of the mass difference (2.52),

$$a_{+2} = \left(1 + \cos^2 i\right) \,, \tag{4.7a}$$

$$a_{\times 2} = 2 \cos i \,, \tag{4.7b}$$

$$a_{+1} = -\Delta \sin i \left(\tfrac{5}{8} + \tfrac{1}{8} \cos^2 i \right) \,, \tag{4.7c}$$

$$a_{\times 1} = \Delta \tfrac{3}{4} \sin i \cos i \,, \tag{4.7d}$$

$$a_{+3} = \Delta \sin i \left(\tfrac{9}{8} + \tfrac{9}{8} \cos^2 i \right) \,, \tag{4.7e}$$

$$a_{\times 3} = -\Delta \tfrac{9}{4} \sin i \cos i \,. \tag{4.7f}$$

We can simplify (4.5) with the following relations,

$$A_k := \left(F_+^2 a_{+k}^2 + F_\times^2 a_{\times k}^2 \right)^{1/2} \tag{4.8}$$

and

$$k\psi_k := \tan^{-1}\left(\frac{F_\times a_{\times k}}{F_+ a_{+k}}\right), \tag{4.9}$$

where $k = 1, 2, 3$ and represents the first three harmonics of the orbital phase. Let us define

$$V_0 = \frac{2G\mu x}{c^2 R}, \tag{4.10}$$

and now write

$$\begin{aligned} h(t) = V_0 \Big[& A_2 \,(\, \cos 2\psi_2 \cos 2\varphi(t) + \sin 2\psi_2 \sin 2\varphi(t) \,) \\ & + x^{1/2} A_1 \,(\, \cos \psi_1 \cos \varphi(t) + \sin \psi_1 \sin \varphi(t) \,) \\ & + x^{1/2} A_3 \,(\, \cos 3\psi_3 \cos 3\varphi(t) + \sin 3\psi_3 \sin 3\varphi(t) \,) \Big] . \end{aligned} \tag{4.11}$$

After using the double angle formulae we have

$$h(t) = \sum_{k=1}^{3} A_k V_k \cos k(\varphi(t) - \psi_k) = \sum_{k=1}^{3} \mathcal{H}_k , \tag{4.12}$$

where $V_2 = V_0$ and $V_1 = V_3 = x^{1/2} V_0$. On the right hand side of (4.12) the template is simply written as the sum of three terms, $\mathcal{H}_k$, representing the first, second and third harmonic.

We will also find it useful to define the following:

$$h_{+1} = h_1 = V_1\, a_{+1} \cos \varphi(t), \tag{4.13a}$$

$$h_{+2} = h_2 = V_2\, a_{+2} \cos 2\varphi(t), \tag{4.13b}$$

$$h_{+3} = h_3 = V_3\, a_{+3} \cos 3\varphi(t), \tag{4.13c}$$

$$h_{\times 1} = h_4 = V_1\, a_{\times 1} \sin \varphi(t), \tag{4.13d}$$

$$h_{\times 2} = h_5 = V_2\, a_{\times 2} \sin 2\varphi(t), \tag{4.13e}$$

$$h_{\times 3} = h_6 = V_3\, a_{\times 3} \sin 3\varphi(t). \tag{4.13f}$$

The waveform (4.12) will be used as a matched filter. It should be immediately noted that there are three phase offset angles $\psi_{1,2,3}$. These angles depend upon the sky position and orientation of the source independently of one another and will need to be maximised over - it is not simply the case that $\psi_2 = 2\psi_1$ etc.

4.2.2 Orthonormalisation

At first glance, one may assume that the three terms of (4.12) could be matched filtered separately, maximising the three phase offset angles as in (3.31), before recombining by taking the sum of squares of the SNRs, a process that neglects any correlation between the harmonics.

To examine the above idea we will look at one polarisation, i.e., $h_{1,2,3}$. Recalling that each template must be normalised such that its overlap is unity, a priori one might expect that to good accuracy

$$\langle \bar{h}, \bar{h} \rangle = \frac{\langle h_1, h_1 \rangle + \langle h_2, h_2 \rangle + \langle h_3, h_3 \rangle}{\langle h, h \rangle} = 1 , \tag{4.14}$$

where the numerator is the output of matched filtering each of $h_{1,2,3}$ separately and the denominator is the normalisation factor, which by definition is

$$\sigma_h := \langle h, h \rangle = \langle h_1, h_1 \rangle + \langle h_2, h_2 \rangle + \langle h_3, h_3 \rangle + 2 \langle h_1, h_2 \rangle + 2 \langle h_1, h_3 \rangle + 2 \langle h_2, h_3 \rangle \ , \tag{4.15}$$

Let us define the *diagonal* and *cross* terms

$$\sigma_\perp = \langle h_1, h_1 \rangle + \langle h_2, h_2 \rangle + \langle h_3, h_3 \rangle \ , \tag{4.16}$$

and

$$\sigma_c = 2 \langle h_1, h_2 \rangle + 2 \langle h_1, h_3 \rangle + 2 \langle h_2, h_3 \rangle \ , \tag{4.17}$$

respectively, that add to give

$$\sigma_h = \sigma_\perp + \sigma_c \, . \tag{4.18}$$

Thus for (4.14) to hold, the cross terms, σ_c, should sum to zero for any choice of waveform parameters and sky location.

The effect of assuming that (4.14) is always true, and filtering the three harmonics separately can be studied by calculating the ratio σ_h:$\sigma_\perp$. If the ratio is always greater than unity, the template would be over-normalised and thus the SNR would be underestimated, which may be acceptable within a certain tolerance. In fact, if the ratio is always close to unity an overestimation of SNR could also be acceptable. Figure 4.3 shows $\sigma_h : \sigma_\perp$ plotted against the total mass for a single set of parameters, and reveals that it would most likely not be appropriate to proceed with the assumption that (4.14) is true - the difference is $\sim 5\%$ at a total mass of $60 M_\odot$. Furthermore, only one choice of mass ratio and inclination angle has been examined. The relative amplitudes of the first and third harmonics, with respect to the second harmonic, increase with mass ratio

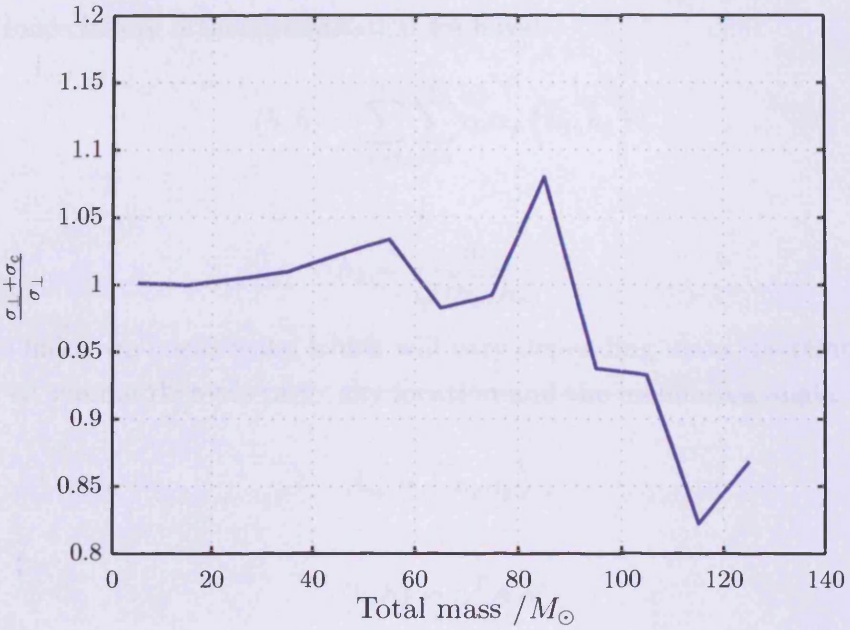

FIGURE 4.3: The ratio of the correct template normalisation, σ_h, to the normalisation using only the diagonal terms, $\sigma_\perp$. In this example the waveforms are of constant mass ratio 4, overhead a LIGO detector, with an inclination angle of 45°.

and also take a maximum at an inclination angle of 90°. Therefore, one would expect a greater difference between σ_h and $\sigma_\perp$ for different choices of parameters.

It is clear that if the harmonics were orthogonal to each other, i.e.,

$$\langle \bar{h}_i, \bar{h}_j \rangle = \delta^i_j \,, \tag{4.19}$$

then $\sigma_c = 0$ and $\sigma_h : \sigma_\perp = 1$. Thus we can avoid problems of over/under-normalising the templates by using any linear transformation that orthogonalises the components of h. The simplest approach is to use Gram-Schmidt orthonormalisation. However, we will use a matrix to transform the original template h into an template h', with orthogonal components. Such an approach is adopted as the transformation matrix becomes useful elsewhere in the filtering algorithm (see Section 4.4). In later discussions we shall consider this transformation as a coordinate change from the original template basis to the orthonormal basis.

In practice, the template consists of six components as each harmonic has two polarisations. Hence before orthonormalisation we have

$$\langle h, h\rangle = \sum_{i=1}^{6}\sum_{j=1}^{6} \alpha_i \alpha_j \left\langle \hat{h}_i, \hat{h}_j \right\rangle , \tag{4.20}$$

where

$$\hat{h}_k = \frac{h_k}{\sqrt{\langle h_k, h_k\rangle}} , \tag{4.21}$$

and α_i are unknown coefficients, which will vary depending upon the template parameters, such as symmetric mass ratio, sky location and the inclination angle. Let us define a matrix

$$A_{ij} = \left\langle \hat{h}_i, \hat{h}_j \right\rangle , \tag{4.22}$$

such that

$$\langle h, h\rangle = \alpha^T A\, \alpha^j . \tag{4.23}$$

It is obvious that A_{ij} is symmetric and the non-diagonal terms represent the cross-correlation between the six components of h. One can introduce a matrix, S, with the properties that it is real and unitary, and that it transforms A_{ij} to a diagonal matrix:

$$A' = S^{-1} A\, S , \tag{4.24}$$

allowing us to rewrite (4.23) as

$$\langle h, h\rangle = \alpha^T \left(S S^{-1}\right) A \, \left(S S^{-1}\right) \alpha , \tag{4.25}$$

or

$$\langle h, h\rangle = \left(\alpha^T S\right) A' \left(S^{-1}\alpha\right) . \tag{4.26}$$

Let us define a *template vector*

$$\mathbf{h} = \left\{\hat{h}_1, \hat{h}_2, \hat{h}_3, \hat{h}_4, \hat{h}_5, \hat{h}_6\right\} , \tag{4.27}$$

allowing us to make the following transformations with the matrix S:

$$\mathbf{h} \to \mathbf{h}' = S^{-1}\mathbf{h} , \tag{4.28a}$$

$$\alpha \to \alpha' = S^{-1}\alpha , \tag{4.28b}$$

$$\alpha^T \to \alpha'^T = \alpha^T S . \tag{4.28c}$$

which gives

$$\langle h, h\rangle = \alpha'^T A' \alpha' , \tag{4.29}$$

where we know that A'_{ij} is diagonal and consequently there are no *cross* terms on the RHS. Since the template and its vector are related as

$$h' = \alpha'^T \mathbf{h}' \ , \tag{4.30}$$

we find

$$\langle h', h' \rangle = \alpha'^T \left\langle \mathbf{h}', \mathbf{h}'^T \right\rangle \alpha' \, . \tag{4.31}$$

All that remains to be done is to find the matrix S used in the transformation, which is straightforward - as S diagonalises A_{ij}, it is simply constructed from the *eigenvectors* of A_{ij}.

Thus far, we have a method that orthorgonalises the six components h_i that form the template h. However, we need to satisfy the normalisation condition $\langle h', h' \rangle = 1$. Since

$$h' = \sum_{j=1}^{6} \alpha'_j \hat{h}'_j \, , \tag{4.32}$$

and

$$\langle h', h' \rangle = \sum_{i=1}^{6} \sum_{j=1}^{6} \alpha'_i \alpha'_j \delta_{ij} \, , \tag{4.33}$$

it is clear that the templates would be normalised if the coefficients satisfied the following

$$\sum_{j=1}^{6} \alpha_j'^2 = 1 \, . \tag{4.34}$$

Hence (4.34) will be used as a constraint in the maximisation of the SNR below.

4.2.3 Maximisation

The maximisation of the SNR is very different to that calculated in (3.31), although it turns out to be straightforward. The SNR, ρ, of the orthonormalised template, $\bar{h}'$, with some data, x, is

$$\rho = \left\langle x, \bar{h}' \right\rangle = \sum_{j=1}^{6} \alpha'_j \left\langle x, \hat{h}'_j \right\rangle \, . \tag{4.35}$$

In order to maximise the SNR over the unknown coefficients, α'_j, of the template, we shall use (4.34) as a constraint. It is then convenient to introduce a Lagrange multiplier,

λ, and maximise the following quantity, Λ, with respect to α'_j and λ,

$$\Lambda = \sum_{j=1}^{6} \alpha'_j \left\langle x, \hat{h'}_j \right\rangle - \lambda \left[\sum_{k=1}^{6} \alpha'^2_k - 1 \right] . \tag{4.36}$$

Finding $d\Lambda/d\alpha'_j = 0$ and $d\Lambda/d\lambda = 0$, yields

$$\left\langle x, \hat{h'}_j \right\rangle - 2\lambda\alpha'_j = 0\,, \tag{4.37}$$

and

$$\sum_{k=1}^{6} \alpha'^2_k = 1\,. \tag{4.38}$$

An obvious solution to (4.37) and (4.38) is

$$\alpha'_j = \frac{\left\langle x, \hat{h'}_j \right\rangle}{\sqrt{\sum_{k=1}^{6} \left\langle x, \hat{h'}_k \right\rangle^2}} \tag{4.39}$$

and

$$\lambda = \frac{1}{2} \sqrt{\sum_{k=1}^{6} \left\langle x, \hat{h'}_k \right\rangle^2}\,. \tag{4.40}$$

By substituting (4.39) in to (4.35) we find

$$\rho_{\max} = \frac{\sum_{j=1}^{6} \left\langle x, \hat{h'}_j \right\rangle \left\langle x, \hat{h'}_j \right\rangle}{\sqrt{\sum_{k=1}^{6} \left\langle x, \hat{h'}_k \right\rangle^2}} = \sqrt{\sum_{l=1}^{6} \left\langle x, \hat{h'}_l \right\rangle^2}\,. \tag{4.41}$$

The maximisation of the SNR is, therefore, simply the sum of squares of the filtered orthonormal vectors that make up the template.

We will also find it useful to define an SNR vector in the primed coordinates,

$$\rho'_i = \left\langle x, \hat{h'}_i \right\rangle\,. \tag{4.42}$$

For proof that the above maximises the SNR, see Section C.1.

4.2.4 Overview of the filtering algorithm

The algorithm that implements the orthonormalisation and filtering is described in a stepwise fashion below. N.B.: the orthonormalisation transformations are applied to the Fourier transformed template components, $\widetilde{h}_{+,\times i}$; i.e., all transformations etc. are calculated in the FD, as we are only interested in the SNR time series at the end of the algorithm.

1. Initially, given the component masses of the template, m_1 and m_2, the amplitudes of the three + polarisations (4.7) are calculated, along with the phase. The amplitudes of the first and third harmonics are dependent on the inclination angle, i. However, the amplitudes will all be normalised (it is their evolution that is important) so one can choose any value, for i other than $i = 0$, so that the first and third harmonic amplitudes are non-zero. (In the case of equal mass templates, the first and third harmonic are correctly set to zero).

2. The + polarisations of the three harmonics, h_{+k}, are constructed and Fourier transformed, giving $\widetilde{h}_{+k}$. Before orthogonalising the templates, there exists a simple relation between the FTs of the two polarisations, namely,

$$\widetilde{h}_{+k} = i\widetilde{h}_{\times k}\,, \tag{4.43}$$

   allowing all six components of $\widetilde{h}_k$ to be calculated from the three components h_{+k}. We now have a vector $\widetilde{h} = \left[\widetilde{h}_{+1}, \widetilde{h}_{\times 1}, \widetilde{h}_{+2}, \widetilde{h}_{\times 2}, \widetilde{h}_{+3}, \widetilde{h}_{\times 3}\right]$ that is to be orthonormalised as described above.

3. As the amplitude of the first and third harmonic may be orders of magnitude below the dominant harmonic, one can encounter problems when computing the transformation matrix. For that reason the components $\widetilde{h}_i$ are normalised *before* the transformation matrix is calculated.

4. The matrix A_{ij} is calculated and the transformation matrix, S^{-1}, is constructed from its eigenvectors.

5. The transformation $\widetilde{\mathbf{h}} \rightarrow \widetilde{\mathbf{h}}' = S^{-1}\widetilde{\mathbf{h}}$, then yields the orthogonal template [4].

6. Although the template components were normalised *before* the transformation to alleviate potential numerical issues, the transformed components $\widetilde{h}'_i$ need to be re-normalised to yield the orthonormal template $\widetilde{\bar{h}}'$.

7. Finally, the SNR is given by (4.41).

---

[4] The calculations of A_{ij}, A'_{ij}, S, S^1 and $\widetilde{\bar{h}}'$ are performed using functions from the GNU Scientific Library [63].

4.3 Initial results

The filtering algorithm was tested in three ways:

- Studying the *ambiguity function*, i.e., the overlap of a single signal with a bank 0.5PN templates.
- Comparing the *overlap* and *faithfulness* (the overlap of the template with the same parameters as the signal) of the 0.5PN template family with standard RWF template families against a random set of FWF (2PN) injected signals.
- Repeating the above study with the signals injected into Gaussian noise at a fixed SNR of 10.

To perform the above tests a template bank was required. In these tests, the template bank metric was calculated using the SPA, as described in Section 3.4.1, with a minimum match of 0.99. The same metric was used for both the RWF and 0.5PN templates, rather than computing a new template bank for the 0.5PN templates [5]. Using the same metric provides a good comparison of the two template families and, in any case, would likely understate the performance of the 0.5PN templates.

We are interested in using the 0.5PN templates as a better, but not an exact, representation of nature's gravitational waves in comparison to RWF templates. For that reason the injected signals were at a higher order of 2PN *in amplitude*. The TT3 approximant at 2PN was used for the phase evolution of the signals *and* both the 0.5PN and RWF templates. A further comparison was also made with RWF templates using the SPA phase approximant at 2PN. However, there was negligible difference between the results of the two RWF models and therefore on the following pages only the results using the TT3 approximant are plotted.

All TD waveforms were tapered using the method to be set out in Chapter 5 and all of the tests were performed using the LIGO design PSD, with a lower cutoff frequency of 40 Hz.

4.3.1 Ambiguity of the 0.5PN templates

The ambiguity function measures the overlap of all the templates in a bank for a given signal, forming a surface that should be peaked around the true value of the signal

---

[5] This would be a complicated task.

parameters. The ambiguity function, therefore, gives an indication of the parameter estimation - the sharper the peak, the more likely the correct values will be recovered in the presence of noise.

Figures 4.4 - 4.9 show the ambiguity function for both the 0.5PN and RWF (TT3) templates for a variety of signals: BNS, NSBH, BBHs and intermediate mass binary black holes (IMBBHs). The signal parameters are located where the black lines meet on these figures.

The ambiguity function of the NSBH signal (Figure 4.5 [left]) has *two* peaks for the 0.5PN templates, giving an insight into potential problems with parameter estimation. In the presence of noise, it is highly likely that a signal could be detected by a template at the secondary maximum. Furthermore, Figure 4.8 and Figure 4.9 show that for IMBBH systems, the ambiguity functions of the 0.5PN templates do not have a well defined peak. Indeed, for the $(40, 60)M_{\odot}$ system (Figure 4.8), the ambiguity function is roughly constant and conceivably any one of the templates may recover a signal in the presence of noise.

The issues with parameter estimation will be discussed in Section 4.6.

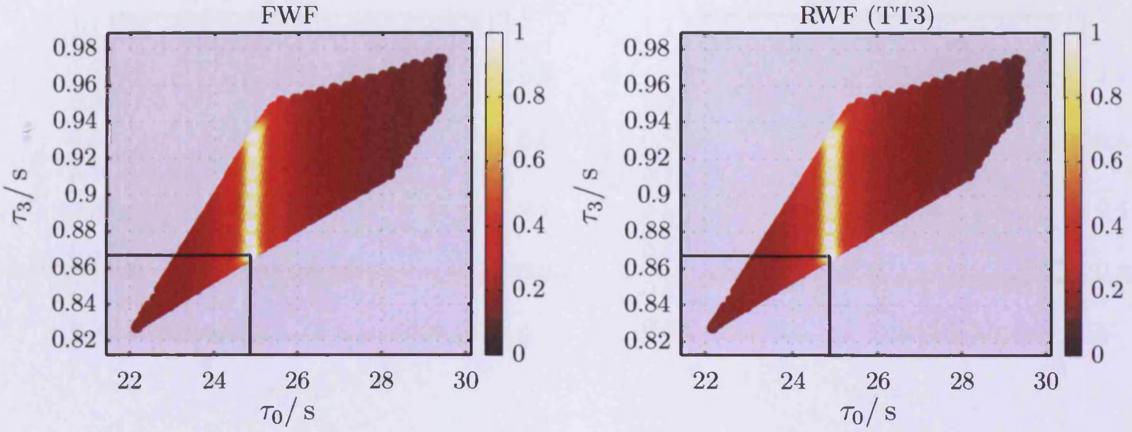

FIGURE 4.4: The ambiguity function of a BNS signal - $(1.38, 1.42)M_\odot$ - for the surrounding region of the template bank. The results for the 0.5PN templates (left) and RWF templates (right) are indistinguishable.

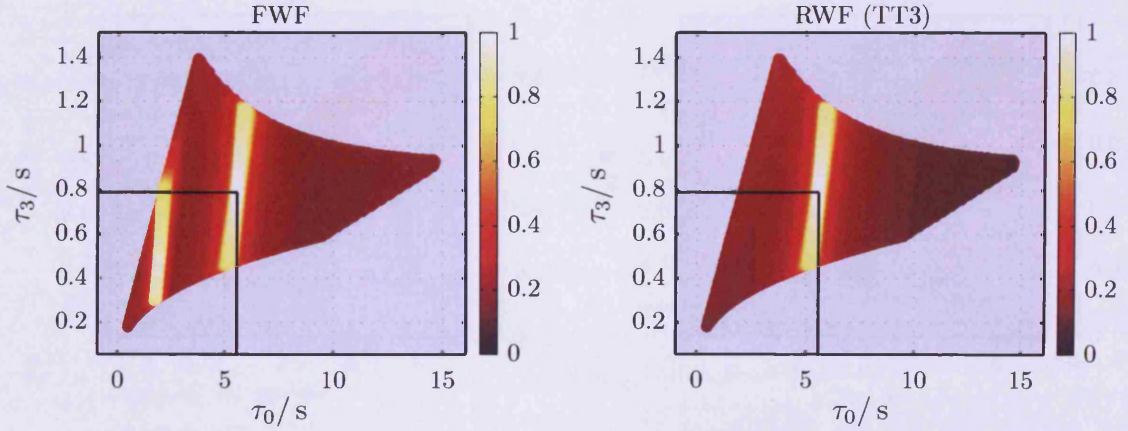

FIGURE 4.5: The ambiguity function of a NSBH signal - $(1.4, 10)M_\odot$. The are two peaks in the function for the 0.5PN templates (left) as opposed to a single maximum for the RWF templates (right).

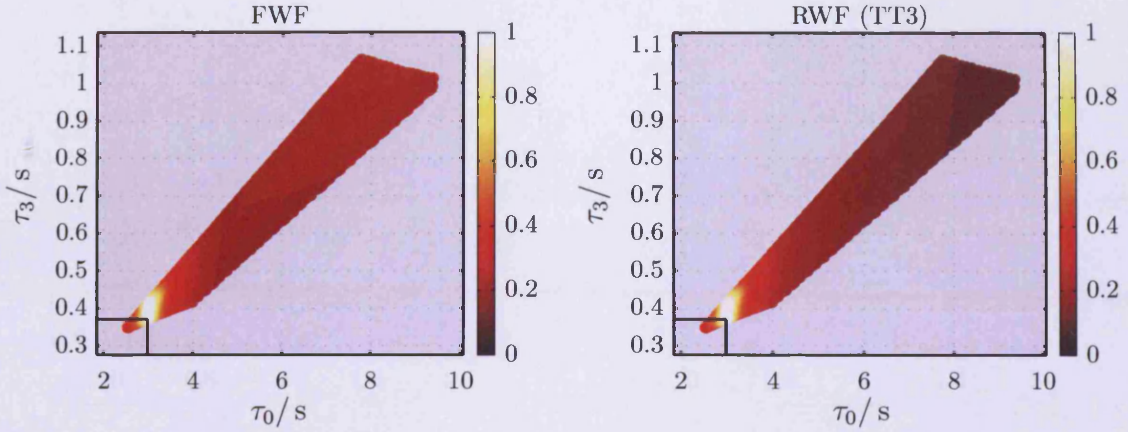

FIGURE 4.6: The ambiguity function of a BBH signal - $(4.8, 5.2)M_\odot$ - for the surrounding region of the template bank. The 0.5PN templates (left) have a slightly larger overlap in the region away from the signal parameters when compared to the RWF templates (right).

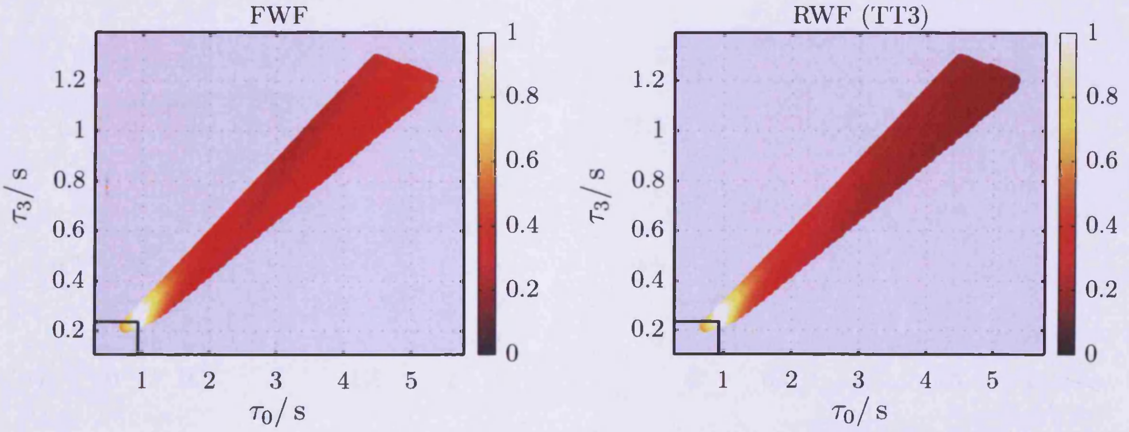

FIGURE 4.7: The ambiguity function of a BBH signal - $(9.5, 10.5)M_\odot$ - for the surrounding region of the template bank. The 0.5PN templates (left) have larger overlap in the region away from the signal parameters when compared to the RWF templates (right).

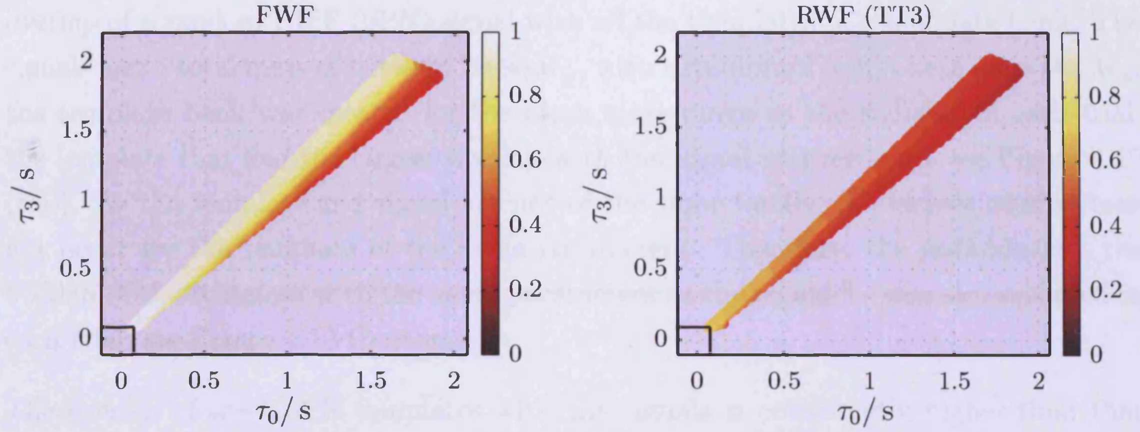

FIGURE 4.8: The ambiguity function of a IMBBH signal - $(40, 60)M_\odot$. There is no well defined maximum for the 0.5PN templates (left) - the overlap is close to unity for a large range of templates. However, the RWF templates (right), show similar behaviour, but do not recover the signal as well.

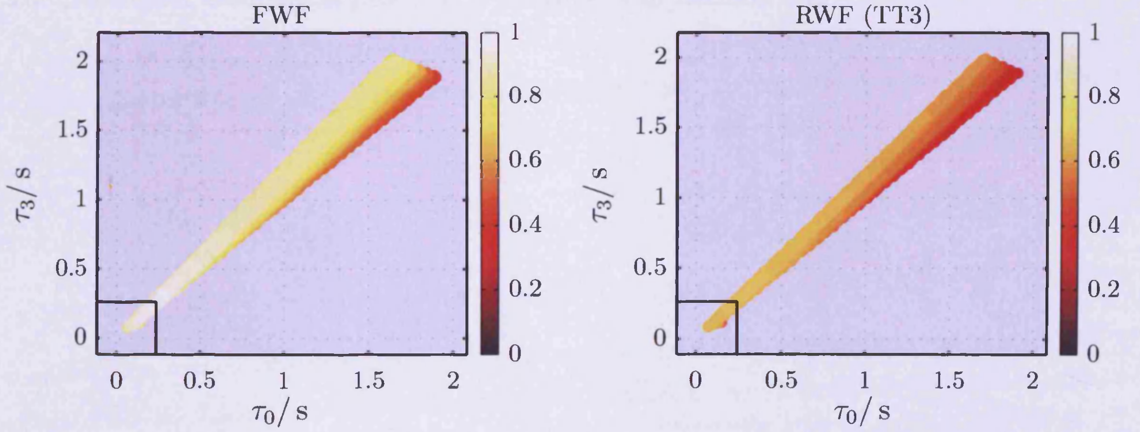

FIGURE 4.9: The ambiguity function of an IMBBH of $(10, 100)M_\odot$. There is no well defined maximum for the 0.5PN templates (left) - the overlap is close to unity for a large range of templates. As in Figure 4.8, the RWF templates (right), show similar behaviour, but do not recover the signal as well.

4.3.2 Overlap and faithfulness

A Monte-Carlo simulation of 10,000 trials was performed with each trial calculating the overlap of a random FWF (2PN) signal with all the templates in a template bank. The signals had a total mass of between 20-90$M_\odot$, with a minimum component mass of $1M_\odot$; the template bank was created for the same mass range as the signals. In each trial, the template that had the largest overlap with the signal was recorded, see Figure 4.10 (top). As the template and signal are not of the same family, the largest overlap may not occur for the template of the same parameters. Therefore, the *faithfulness* - the overlap of the template with the same parameters as the signal [6] - was also recorded in each trial, see Figure 4.10 (bottom).

The overlap of the 0.5PN templates with the signals is consistently higher than that of the RWF templates, with the difference becoming clearer above $40M_\odot$. There is little difference between the faithfulness plot and the overlap plot. The results shown in Figure 4.10 are promising. However, when the recovered parameters are compared, the 0.5PN templates do not fare so well. Figure 4.12 shows the recovered chirp mass, i.e., the chirp mass of the template with the largest overlap, for the 0.5PN templates (top) and the RWF (TT3) templates (bottom). The parameter estimation is comparable for low values of chirp mass, but for values above $1.8M_\odot$ three distinguishable 'bands' exist for the 0.5PN templates; one that recovers the chirp mass well and two that underestimate the chirp mass. There are also two bands for the case of RWF templates.

The parameter estimation problem is diagnosed in Section 4.6.

---

[6] Recall that the template parameters are only the component masses; all other parameters are maximised over.

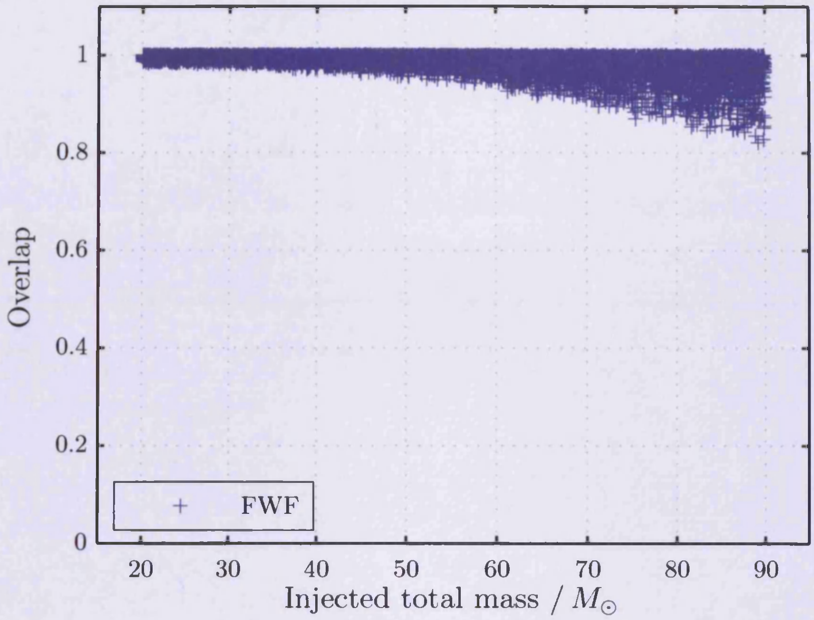

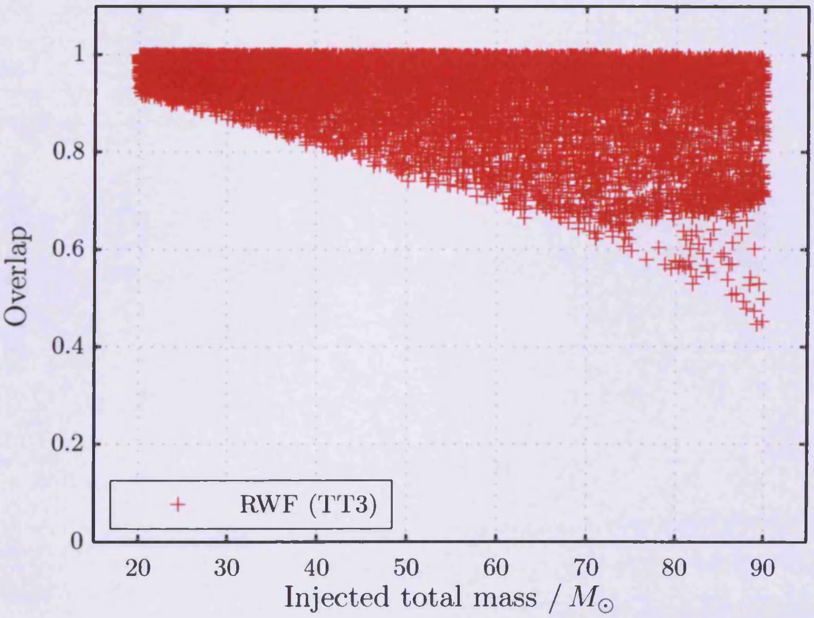

FIGURE 4.10: The overlap of the 0.5PN filter (top) and the RWF (bottom), with FWF (2PN) signals.

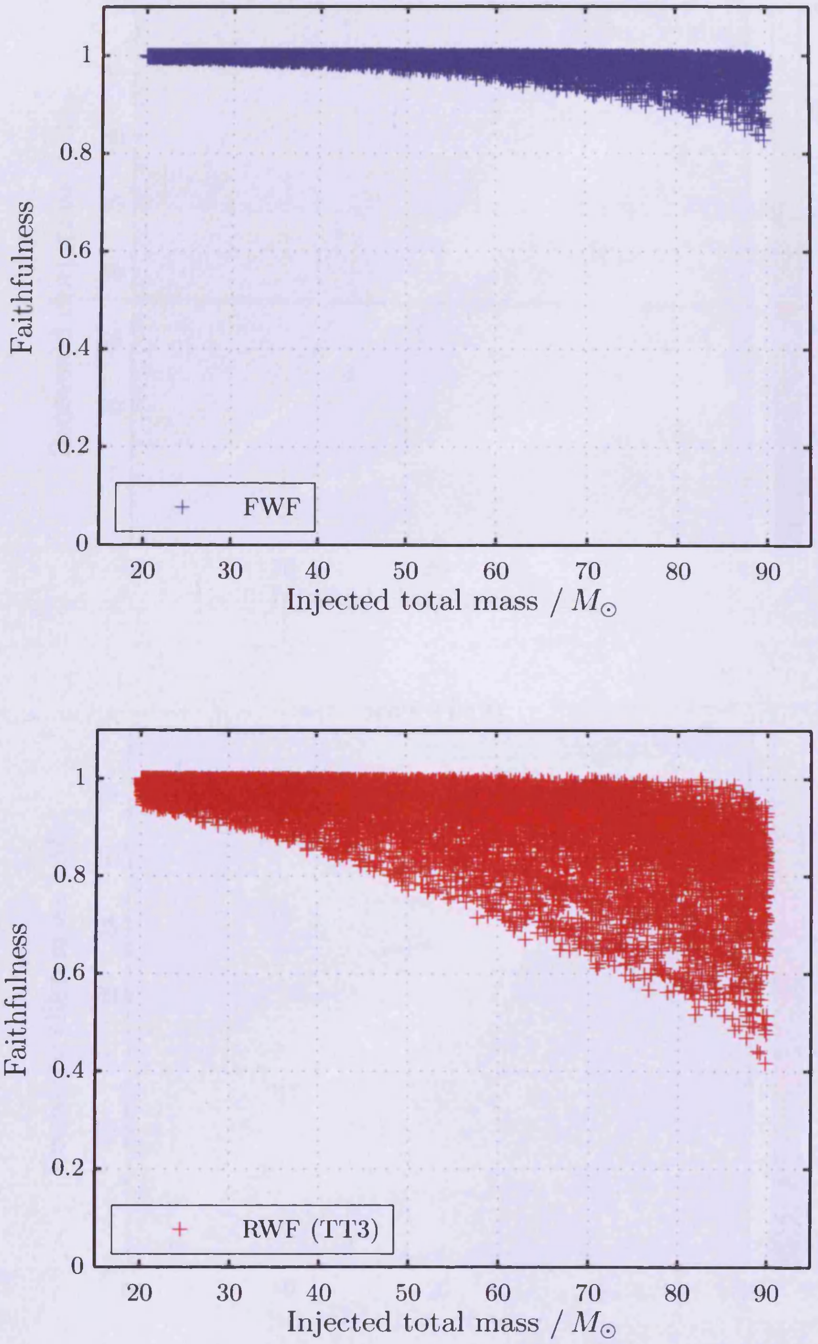

FIGURE 4.11: The faithfulness of the 0.5PN filter (top) and the RWF (bottom), with FWF (2PN) signals.

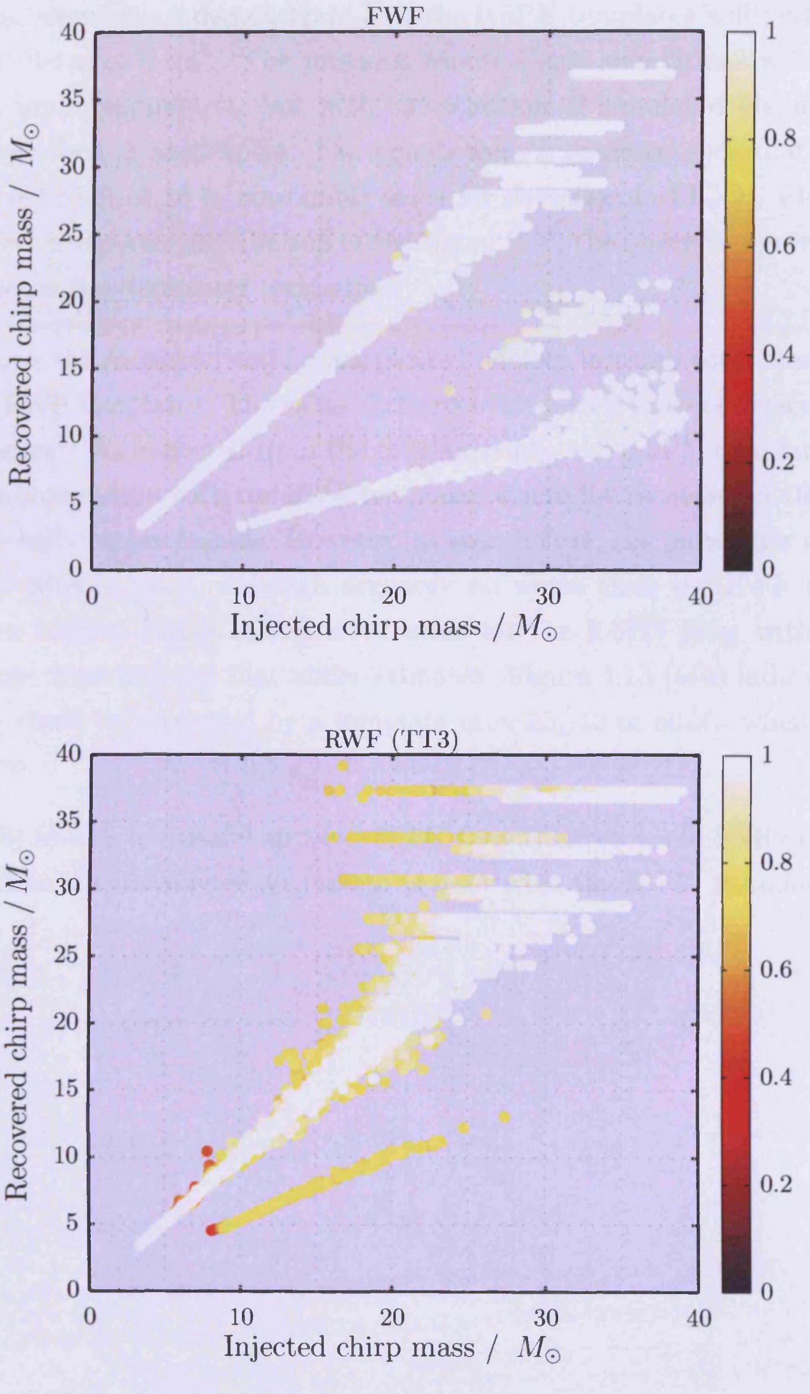

FIGURE 4.12: The recovered chirp mass corresponding to the overlaps (Figure 4.10) for the 0.5PN templates (top) and the RWF (TT3) templates (bottom).

4.3.3 Signal and noise simulations

Signal and noise simulations demonstrate how the 0.5PN templates will perform when analysing 'real' detector data[7]. The previous Monte-Carlo simulations were repeated with the same input parameters, but with the addition of simulated Gaussian noise, generated as described in Section 6.6. The signals were normalised such that they were injected at a fixed SNR of 10 (a reasonable value for detection in LIGO). Fluctuations in the noise affect the power distribution of the signal (i.e., the observed spectrum) and, therefore, influence the parameter estimation.

Figure 4.13 shows the recovered total mass plotted against injected total mass for both the 0.5PN and RWF templates. The value of the recovered SNR is also shown on the plot as a colour gradient. As expected from the overlap study, the 0.5PN templates recover the SNR well in comparison with the RWF templates where the recovered SNR is greatly reduced for the higher mass signals. However, as seen before, the parameter estimation with the 0.5PN filter is poor, although arguably no worse than the RWF templates. There are three distinct bands of recovered mass for the 0.5PN filter with one that overestimates the mass and one that underestimates. Figure 4.13 (top) indicates that a signal of $40M_{\odot}$ could be recovered by a template of $\sim$ 15, 40 or $60M_{\odot}$ when using the 0.5PN templates.

The RWF (TT3) filter is not useful above $\sim 50M_{\odot}$ for either recovered SNR or recovered mass. N.B.: where the parameter esitmation is poor with the RWF, it underestimates the mass.

---

[7] Under the assumption that the detector noise is Gaussian.

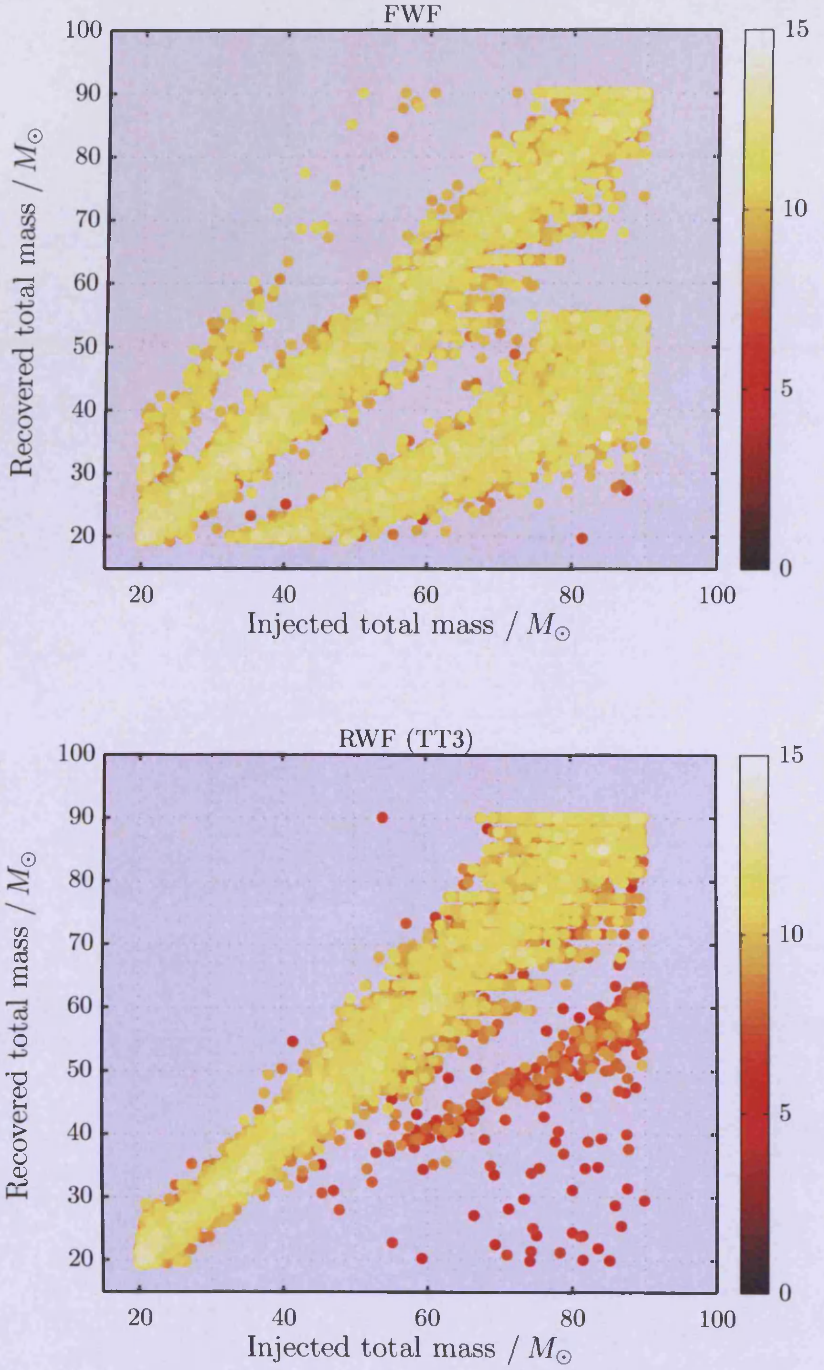

FIGURE 4.13: The recovered total mass when using the 0.5PN templates (top) compared to the RWF TT3 model. The colour map shows the value of the recovered SNR.

Signal Mass $/M_\odot$	Signal FLSO /Hz	Template Mass $/M_\odot$	Template FLSO /Hz		
			1	2	3
40	~ 110	20	$\sim$ **110**	~ 220	~ 330
		40	~ 55	$\sim$ **110**	~ 165
		60	~ 36	~ 73	$\sim$ **110**
60	~ 73	30	$\sim$ **73**	~ 147	~ 220
		60	~ 36	$\sim$ **73**	~ 110
		90	~ 24	~ 48	$\sim$ **73**

TABLE 4.1: The signal FLSO is compared with the FLSO of each of the three harmonics in the 0.5PN template for three different choices of template total mass, such that in each case one of the template harmonic's FLSO matches that of the signal.

4.3.4 The parameter estimation problem

The band that *underestimates* the recovered mass in Figure 4.13 appears to have a clear threshold at template total masses of approximately $50M_\odot$, i.e., it ceases to exist above that value, which corresponds to the mass at which the first harmonic does not enter the sensitive band and so is not present in the template. It is, therefore, no great leap of faith to conclude that the underestimating band occurs when the dominant harmonic of the signal, which is much larger in amplitude than the signal's first and third harmonics, is recovered by the first harmonic of the template. One must then conclude that the band that *overestimates* the recovered mass is caused by the template's third harmonic recovering the dominant harmonic of the signal. Such an effect may be qualitatively understood by comparing the frequency evolution of the signals. Table 4.1 shows the signal FLSO for two choices of total mass. In each case the FLSOs of the template harmonics are shown for three different masses, chosen such that the FLSO of one of the harmonics matches that of signal. The information in this table goes some way to explaining why in Figure 4.13 it was observed that a signal of 40 $M_\odot$ could be recovered by a template of approximately $15M_\odot$ and $60M_\odot$

Comparing the FLSOs gives some insight into the parameter estimation problem, but, as we have learned in section 4.1.2, the parameter estimation depends upon the observed spectra. Let us turn our attention to the ambiguity function. Figure 4.5 showed that there are two peaks in the ambiguity function of a $(1.4, 10)M_\odot$ system with the 0.5PN templates. The second peak occurs at approximately $(3.8, 14)M_\odot$, which is an overestimation that we believe is caused by the third harmonic of the template matching the dominant harmonic of the signal. Figure 4.14 shows the observed spectra of the second and third harmonic of the aforementioned masses, respectively.

N.B.: the RWF templates also underestimate the mass for large signal masses, which is likely to be due to the second (and only) harmonic of the template matching the third

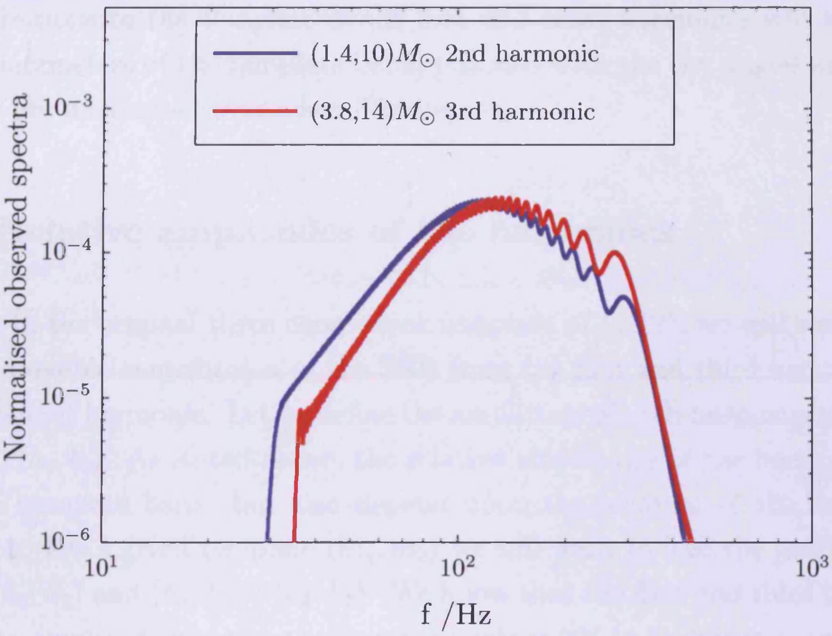

FIGURE 4.14: The observed spectra of the second harmonic of a $(1.4, 10)M_\odot$ waveform compared to the third harmonic of a $(3.8, 14)M_\odot$ waveform. Both are normalised to unity.

harmonic of the signal. One must conclude that this must also occur with the 0.5PN templates.

4.4 Implementing a constraint on the template harmonics

It should be of no great surprise that the parameter estimation problem exists. The first and third harmonics are an order (v/c) smaller in amplitude than the dominant harmonic, yet we place no constraint on the SNR contributions from each harmonic, allowing the dominant harmonic of the signal to have a greater correlation with one of the sub-dominant template harmonics. The simplest constraint one can place on the template is to check that the contributions to the SNR from the first and third template harmonics do not exceed their expected values when compared to the contribution from the dominant harmonic. In order to implement such a constraint there are several things to consider. Firstly, the prior information regarding the amplitudes of the harmonics applies only to the non-transformed templates. Once the templates are orthonormalised, it no longer makes physical sense to discuss the components. We will, therefore, need to implement a constraint based on the physical template before transformation. Secondly, the contributions to the template of the first and third harmonics will vary, not only with the parameters of the template bank, but also with the sky angles and inclination angle that are maximised over when filtering.

4.4.1 Relative amplitudes of the harmonics

Returning to the original three component template of (4.12), we will want to find the maximum possible contribution of the SNR from the first and third harmonics relative to the dominant harmonic. Let us define the amplitude of each harmonic as its expected SNR^2, i.e., $\langle h_i, h_i \rangle$. As stated above, the relative amplitudes of the harmonics will vary across the template bank, but also depend upon the location of the source and the polarisation. For a given template (m_1, m_2) we will want to find the maximum ratio of $\langle h_1, h_1 \rangle : \langle h_2, h_2 \rangle$ and $\langle h_3, h_3 \rangle : \langle h_2, h_2 \rangle$. We know that the first and third harmonic take a maximum amplitude when the inclination angle is 90° (4.7), but it is unclear how the relative amplitudes will vary with the sky angles. One can therefore use a maximisation algorithm on the ratios, with the inclination fixed at 90° and the sky position angles set as free parameters. However, to do so for each template in the bank is likely to be computationally expensive. Instead, we will examine the maximum relative amplitudes at a series of points on the template bank and try to find a function that fits those results.

Figure 4.15 shows the output of the maximum ratio of the inner products of the first and second harmonic, calculated for a range of mass choices using a maximisation algorithm. N.B.: the first harmonic does not enter the detector bandwidth above $\sim 50M_\odot$ and hence the ratio will be set to zero in such cases. Figure 4.16 shows the ratio of the third and second harmonic calculated in the same manner (note the different limits on the axes).

Figure 4.17 and Figure 4.18 show fitting functions chosen by trial and error to match Figure 4.15 and Figure 4.16, respectively. The functions used in Figure 4.17, denoted R_{12} is

$$R_{12} = \frac{0.012}{10.67}\left[\left(\left|M_T - 30\right|(0.25-\eta)\right)^{0.75-\eta} + 25\,(0.25-\eta)\right] \tag{4.44}$$

and the function used in Figure 4.18, denoted R_{32} is

$$R_{32} = \frac{0.42}{0.23} f(M_T, \log(60), [0.75+\eta]).(0.25-\eta)M_T^{1.2} \tag{4.45}$$

where $f(x,y,z)$ is the log-normal distribution (see C.2). N.B.: in this notation $R_{22} = 1$. When compared to the calculated relative amplitudes, both fitting functions had an average error of less than 10%. It is important to note that the functions used to fit the

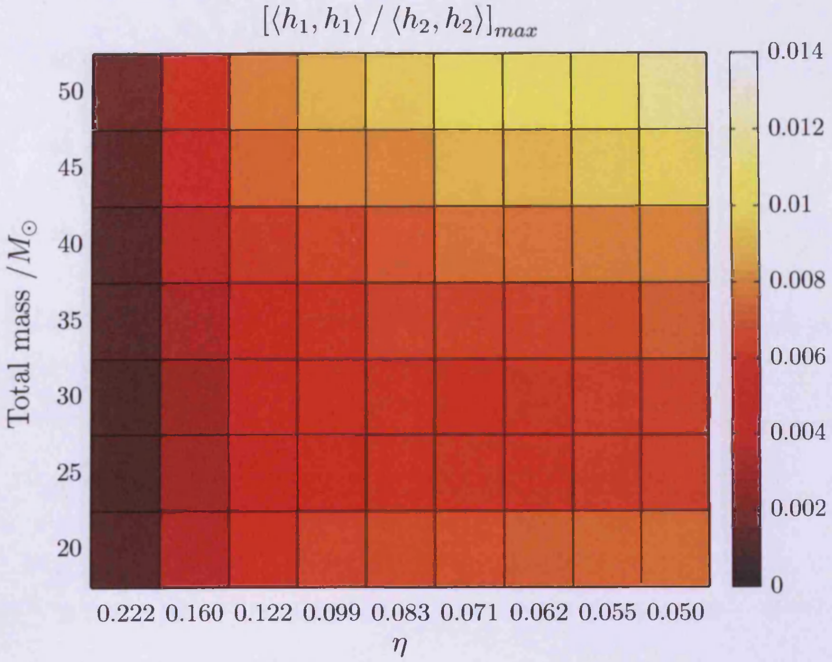

FIGURE 4.15: The maximised ratio $\langle h_1, h_1\rangle : \langle h_2, h_2\rangle$ plotted for a number of choices of M_T and the symmetric mass ratio η.

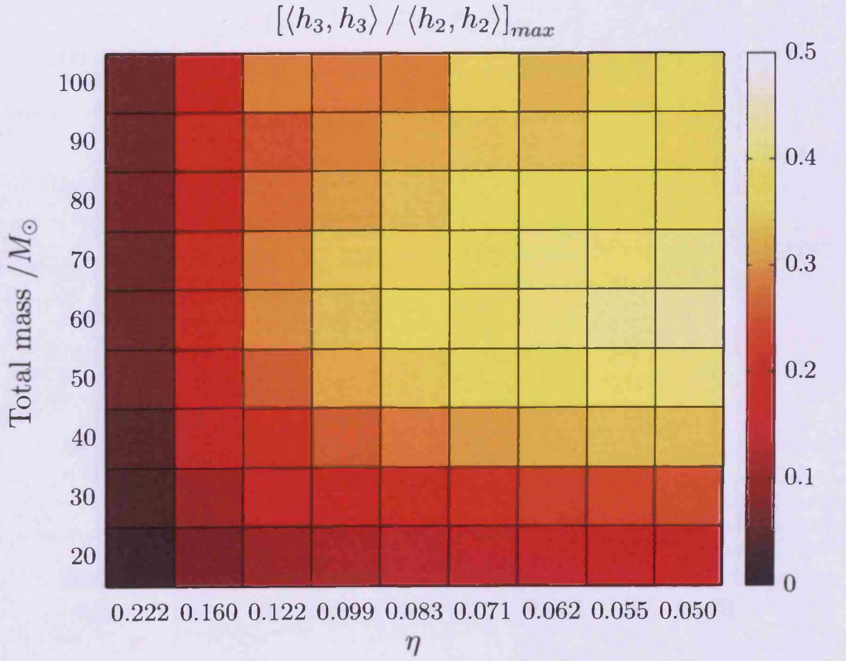

FIGURE 4.16: The maximised ratio $\langle h_3, h_3\rangle : \langle h_2, h_2\rangle$ plotted for a number of choices of M_T and η.

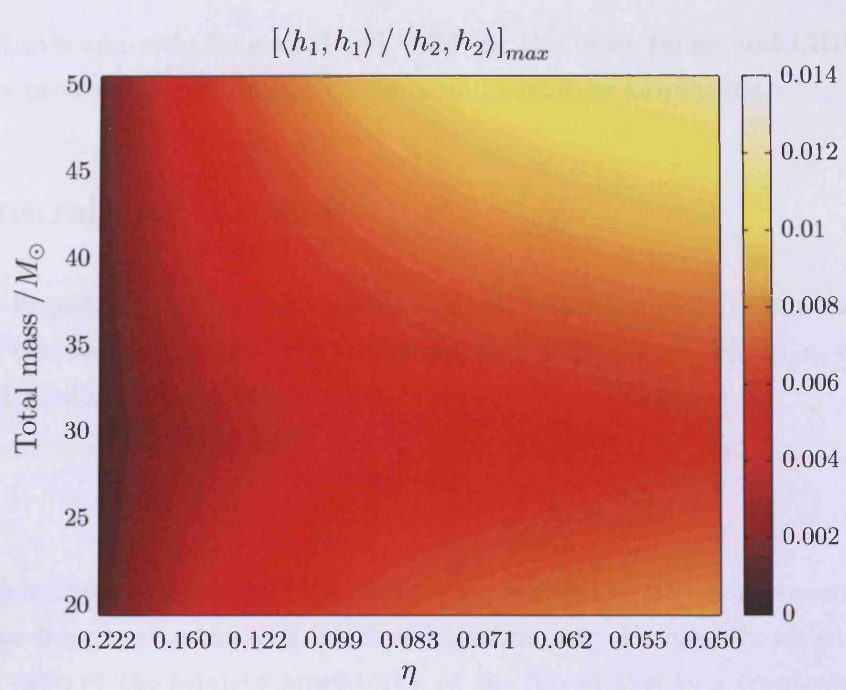

FIGURE 4.17: A fit to the maximised ratio $\langle h_1, h_1\rangle : \langle h_2, h_2\rangle$ as a function of M_T and η.

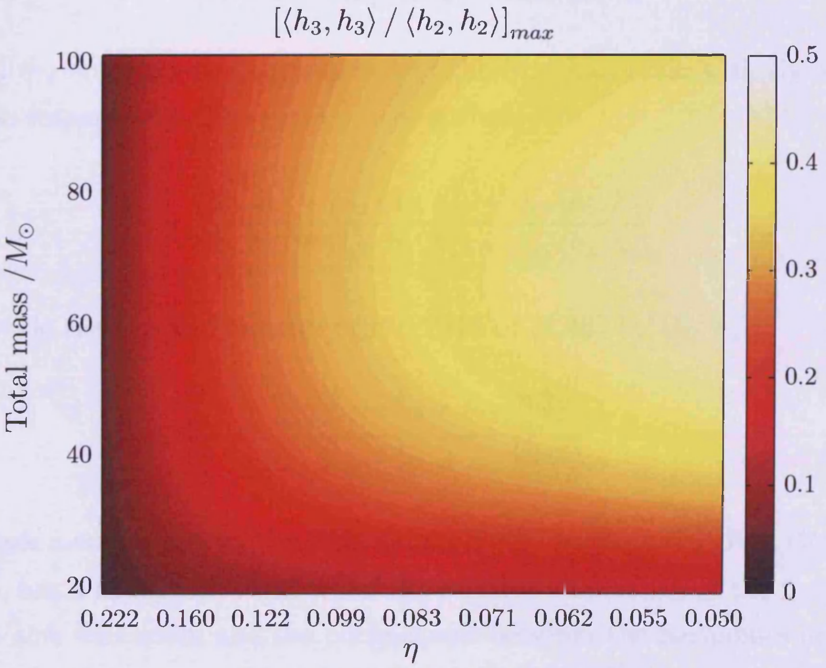

FIGURE 4.18: A fit to the maximised ratio $\langle h_3, h_3\rangle : \langle h_2, h_2\rangle$, as a function of M_T and η.

relative amplitudes can only be considered valid for the mass range and LIGO design PSD that were used when calculating the maximum relative amplitudes.

4.4.2 Constraining the SNR

As we wish to implement a constraint in the original template basis, using the relative amplitudes of the harmonics, we will transform the SNR vector, ρ'_i, to ρ_i using the inverse of the transformation matrix, which is simply S,

$$\rho'_i \rightarrow \rho_i = S\rho'_i \,. \tag{4.46}$$

Let us consider a *three-component* SNR vector, $\overset{(3)}{\rho}_\mu$, where the first component consists of contributions from both phases of the first harmonic etc. Essentially we wish to use the maximum ratio of the relative amplitudes of the harmonics as a constraint on the ratio $\overset{(3)}{\rho}_1 : \overset{(3)}{\rho}_2$. However, as we are in the original basis, we must also consider the cross correlation between the harmonics. The SNR of the first harmonic, $\overset{(3)}{\rho}_1$, is defined as

$$\overset{(3)}{\rho}_1 = \langle h_1, h_1 \rangle + \beta_{12} \langle h_2, h_2 \rangle + \beta_{13} \langle h_3, h_3 \rangle \,, \tag{4.47}$$

where β_{12} and β_{13} are unknown correlations of the first harmonic with the second and third harmonic respectively. The ratio $\overset{(3)}{\rho}_1 : \overset{(3)}{\rho}_2$ is then

$$\frac{\overset{(3)}{\rho}_1}{\overset{(3)}{\rho}_2} = \frac{\langle h_1, h_1 \rangle + \beta_{12} \langle h_2, h_2 \rangle + \beta_{13} \langle h_3, h_3 \rangle}{\langle h_2, h_2 \rangle + \beta_{12} \langle h_1, h_1 \rangle + \beta_{23} \langle h_3, h_3 \rangle} \,. \tag{4.48}$$

Let us now divide the top and bottom of the RHS of (4.48) by $\langle h_2, h_2 \rangle$,

$$\frac{\overset{(3)}{\rho}_1}{\overset{(3)}{\rho}_2} = \frac{\frac{\langle h_1, h_1 \rangle}{\langle h_2, h_2 \rangle} + \beta_{12} + \beta_{13}\frac{\langle h_3, h_3 \rangle}{\langle h_2, h_2 \rangle}}{1 + \beta_{12}\frac{\langle h_1, h_1 \rangle}{\langle h_2, h_2 \rangle} + \beta_{23}\frac{\langle h_3, h_3 \rangle}{\langle h_2, h_2 \rangle}} \,. \tag{4.49}$$

We wish to place a constraint on the maximum allowed ratio (4.49). It is clear that the numerator, $\overset{(3)}{\rho}_1$, has a maximum value when the relative amplitudes of the first and third harmonics are at a maximum and the correlations between the harmonics are also at a maximum. For simplicity, we will heuristically assume that this also gives the maximum value of the ratio (4.49). N.B.: this also naively assumes that the relative amplitudes of the first and third harmonic are a maximum for the same set of sky angles. Our constraint on the first harmonic, C_1, is therefore

$$C_1 = \frac{\overset{(3)}{\rho}_1}{\overset{(3)}{\rho}_2} = \frac{R_{12} + c_{12} + c_{13}R_{32}}{1 + c_{12}R_{12} + c_{23}R_{32}}\,, \tag{4.50}$$

where c_{12}, c_{13} and c_{23} are the maximum correlations between the harmonics over both phases (i.e., the overlap), calculated using the method of Damour et al. [64] (see C.3 for details). Following the same reasoning we set the constraint on the third harmonic, C_3,

$$C_3 = \frac{\overset{(3)}{\rho}_3}{\overset{(3)}{\rho}_2} = \frac{R_{13} + c_{13}R_{13} + c_{12}}{1 + c_{12}R_{12} + c_{23}R_{32}}\,. \tag{4.51}$$

4.4.3 Implementation

For a given template the *six-component* SNR vector, ρ'_i, is calculated and transformed to the original coordinates, giving ρ_i. Recall that the first two components of ρ_i relate to the two phases of the first harmonic etc. The ratio of the *three-component* SNR, $\overset{(3)}{\rho}_1 : \overset{(3)}{\rho}_2$, is then calculated and the following inequality is evaluated:

$$\sqrt{\frac{\rho_1^2 + \rho_2^2}{\rho_3^2 + \rho_4^2}} \leq C_1\,. \tag{4.52}$$

If the inequality is violated, the SNR for the template is set to 0, i.e., it is discarded at that point in the SNR time series. Likewise, for the third harmonic the inequality is

$$\sqrt{\frac{\rho_5^2 + \rho_6^2}{\rho_3^2 + \rho_4^2}} \leq C_3\,, \tag{4.53}$$

and the template will be discarded if the inequality is violated.

4.5 Results

Figure 4.19 shows the recovered mass using the constrained 0.5PN templates, repeating the signal and noise simulation as before, with a fixed SNR of 10. When compared to the original results (Figure 4.13 [top]), it is clear that the constraint has improved the 0.5PN filtering algorithm. The bands that overestimate and underestimate the total mass no longer exist, with the exception of a few templates at low mass that overestimate and a small band at high mass that underestimate. Figure 4.20 shows the recovered mass and the symmetric mass ratio of the templates. Where the parameter estimation is poor

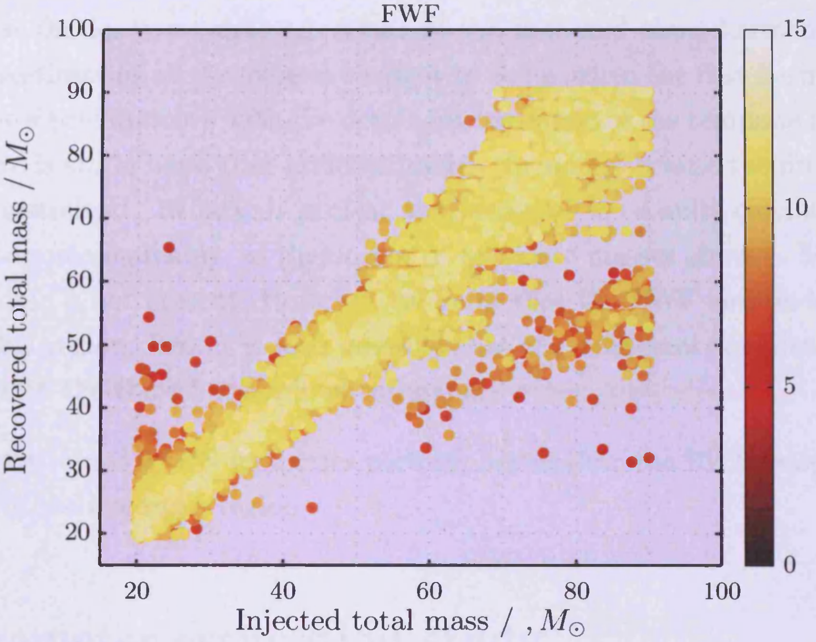

FIGURE 4.19: The recovered total mass when using the 0.5PN filter, with a constraint implemented. The colour map shows the value of the SNR.

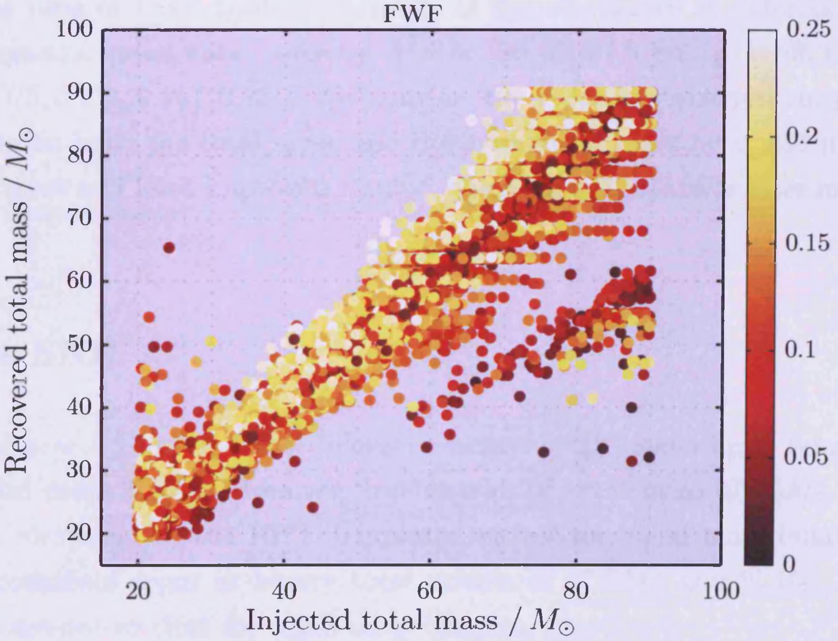

FIGURE 4.20: The recovered total mass when using the 0.5PN filter, with a constraint implemented. The colour map shows the value of the template symmetric mass ratio. The poor parameter estimation appears where the templates are the least constrained.

the templates are of a small symmetric mass ratio, which is understandable as these templates have the least constrained values of the first and third harmonics. Given that the underestimation of the mass is thought to occur when the first harmonic of the template of the signal matches with the dominant harmonic of the template it is slightly surprising there is still a band that underestimates the mass because the first harmonic is the most constrained. In fact, it is clear that some of the results cannot be caused by the first harmonic matching, as they occur at template masses above $\sim 50M_\odot$ where the first harmonic is not present. However, we know that the RWF also underestimates the mass in this region, hence, is also possible that the dominant template harmonic matches well with the third harmonic of the signal,

Overall, the constrained 0.5PN templates perform better than the RWF templates, with the exception of the low mass region.

4.6 Parameter estimation study

The results shown in Figure 4.19 are promising and give some indication into improvements in parameter estimation with the constrained 0.5PN templates. Here a deeper study of the parameter estimation is presented. Further Monte-Carlo simulations were performed this time of 1,000 trials for a range of signals masses at different values of SNR and symmetric mass ratio, namely $M_T = [30, 45, 67.5, 80]$, $\rho = [8, 16, 64]$ and $\eta = [0.050, 0.075, 0.111, 0.167, 0.25]$. We examine the error in recovered chirp mass as this depends upon both the total mass and the symmetric mass ratio and present examples of the most and least improved results[8] when using the 0.5PN filter in a variety of contexts.

4.6.1 Low SNR

At an SNR of $\rho = 8$ there is little difference between the constrained templates for binaries of total mass $30M_\odot$. However, for binaries of total mass of $45M_\odot$ there are improvements compared to the RWF templates except for equal mass binaries. The greatest improvements occur at binary total masses of $67.5M_\odot$ and $85M_\odot$, again the improvements are not so clear for equal mass binaries.

Low SNR - least improved Figure 4.21 shows an example where there is little difference between the 0.5PN and RWF, whereas Figure 4.22, shows an example where

---

[8] I.e., the most improved by qualitatively studying histograms of the errors.

the RWF templates outperform the 0.5PN templates - an equal mass signal of total mass $45M_{\odot}$. N.B.: for the other choices of symmetric mass ratio at $45M_{\odot}$ the 0.5PN templates perform better.

Low SNR - most improved As would be expected from Figure 4.19, the greatest improvements occur for the high mass signals where the 0.5PN templates outperform the RWF templates. We also see a bias in the recovered chirp mass with a peak away from the true value, which is much more dramatic for the RWF templates. See Figure 4.23 and Figure 4.24.

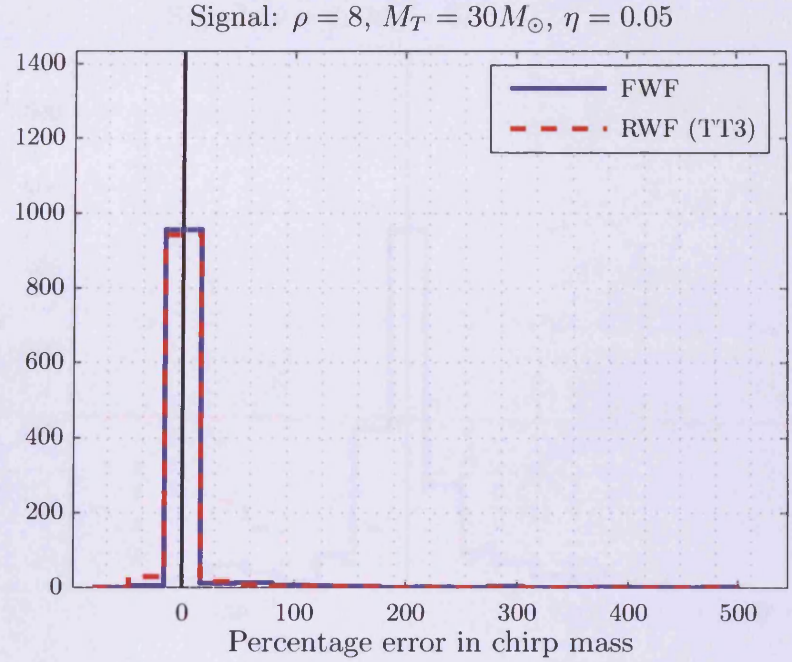

FIGURE 4.21: Histogram of the percentage error in chirp mass for a low SNR, low mass signal of symmetric mass ratio $\eta = 0.05$. There is negligible difference between the performance of the two template families.

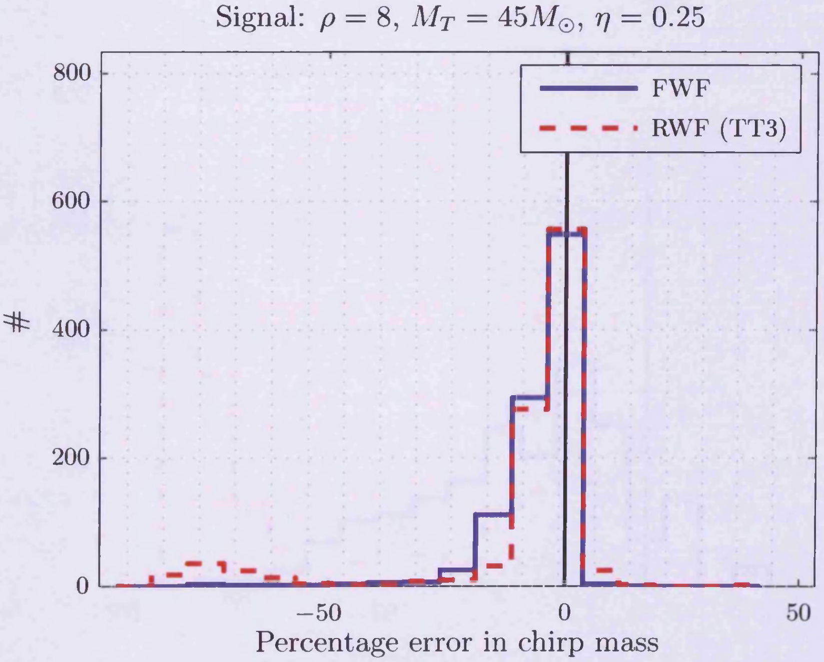

FIGURE 4.22: Histogram of the percentage error in chirp mass for a low SNR, medium mass signal of equal mass ($\eta = 0.25$). There is negligible difference between the performance of the two template families.

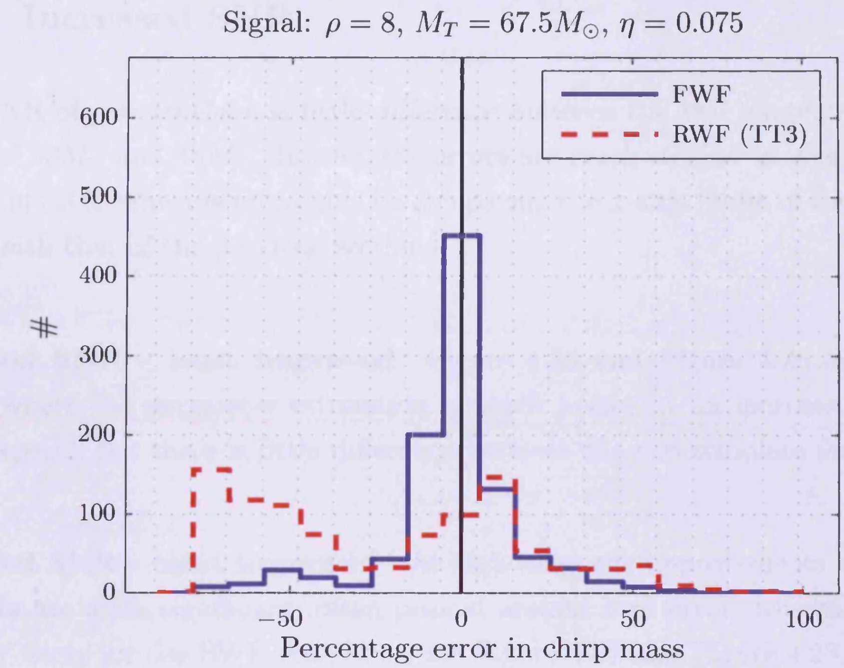
Signal: $\rho = 8$, $M_T = 67.5 M_\odot$, $\eta = 0.075$

FIGURE 4.23: Histogram of the pecentage error in chirp mass for a low SNR, high mass signal of symmetric mass ratio $\eta = 0.075$. The 0.5PN templates clearly outperform the RWF templates.

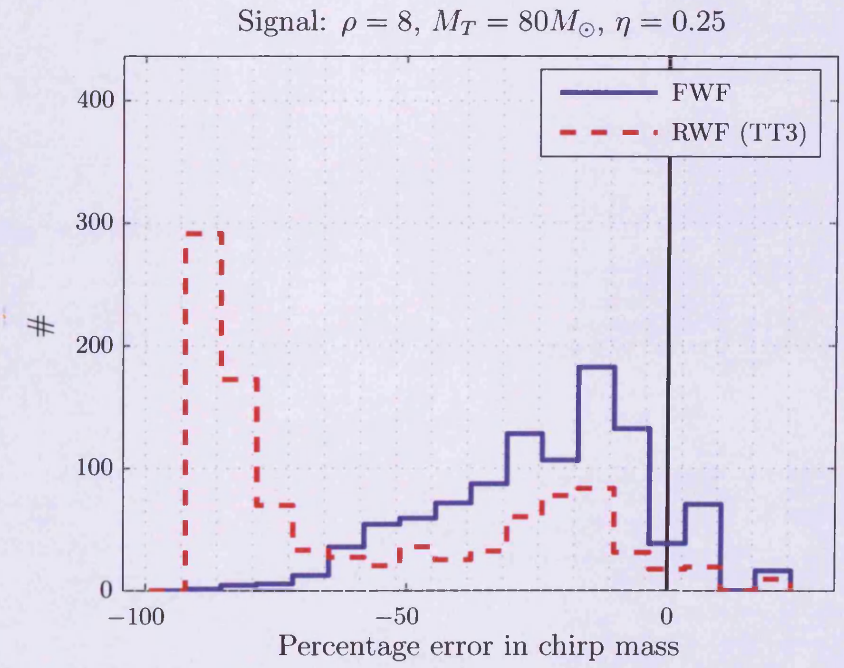
Signal: $\rho = 8$, $M_T = 80 M_\odot$, $\eta = 0.25$

FIGURE 4.24: Histogram of the percentage error in chirp mass for a low SNR, high mass signal of equal mass ($\eta = 0.25$). The RWF templates have a large bias whereas the 0.5PN templates peak close to zero, although the peak is not sharp.

4.6.2 Increased SNR

At an SNR of $\rho = 16$ there is little difference between the two template families total masses of $30M_{\odot}$ and $45M_{\odot}$. Indeed, the errors are much smaller in general, due to the increase in SNR, which is noticeable by comparing the x-axis limits of the figures in this section with that of the previous section.

Increased SNR - least improved Figure 4.25 and Figure 4.26 are examples of results, where the parameter estimation is much better at an increased SNR (as one would expect), but there is little difference between the two template families.

Increased SNR - most improved At high mass the improvements with the 0.5PN templates are quite significant, often peaked around zero error, whereas there a large bias may occur for the RWF templates, see Figure 4.27 and Figure 4.28.

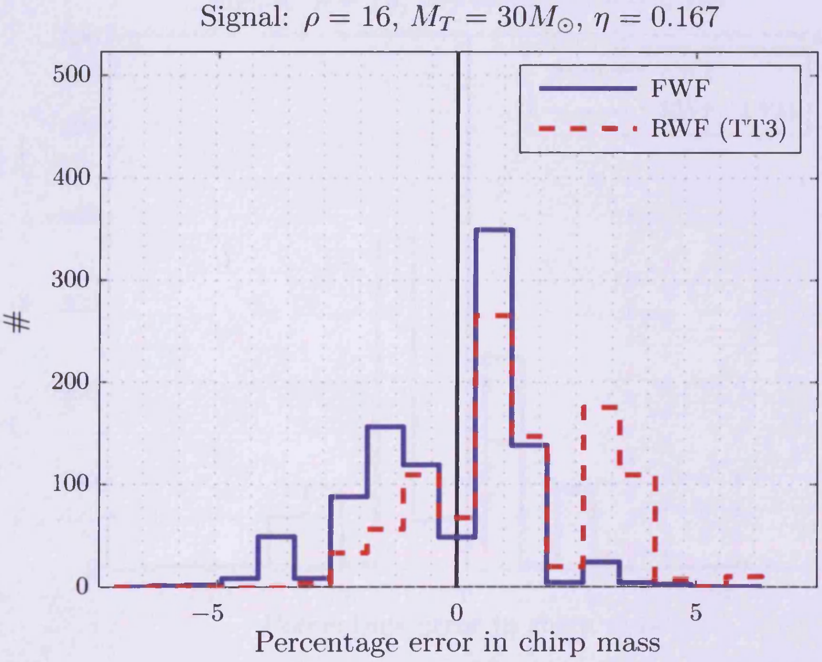

FIGURE 4.25: Histogram of the percentage error in chirp mass for an intermediate SNR, low mass signal of symmetric mass ratio $\eta = 0.167$. Results are similar for both template families; the errors are within $\sim 5\%$.

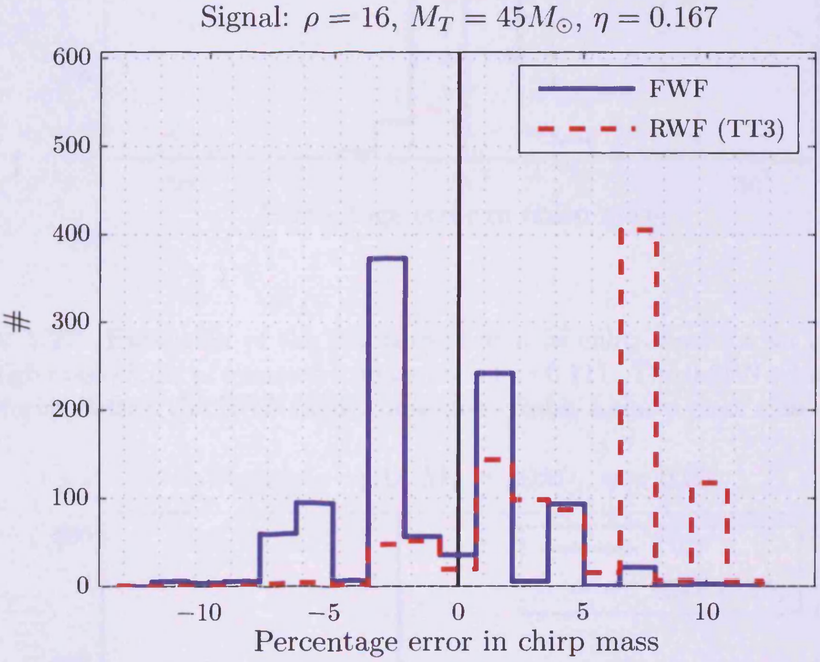

FIGURE 4.26: Histogram of the percentage error in chirp mass for an intermediate SNR, medium mass signal of symmetric mass ratio $\eta = 0.167$. Both template families are within $\sim$ 10%, but have a bias. The 0.5PN templates largest peak is closer to zero.

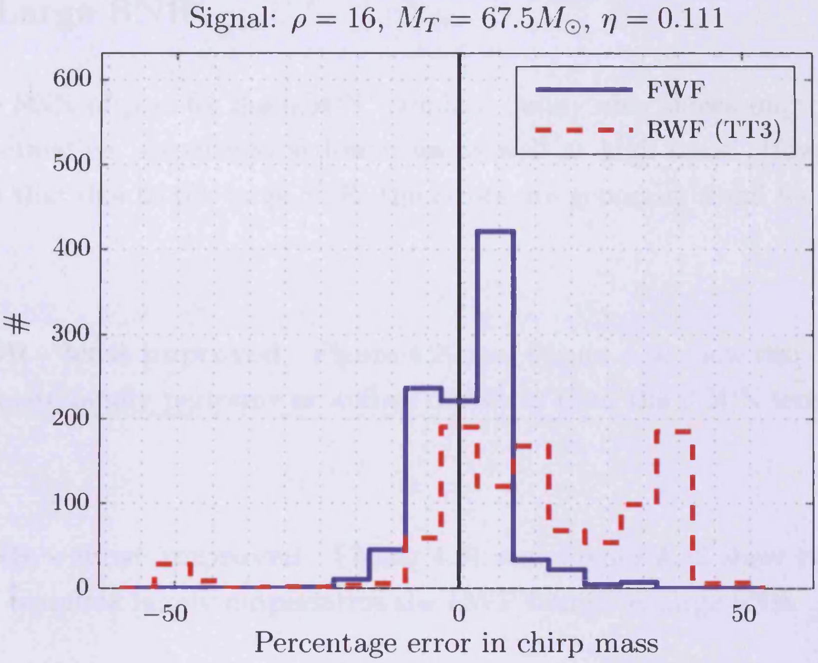

FIGURE 4.27: Histogram of the percentage error in chirp mass for an intermediate SNR, high mass signal of symmetric mass ratio $\eta = 0.111$. The 0.5PN template family performs better, the RWF family does not exhibit a sharp peak close to zero.

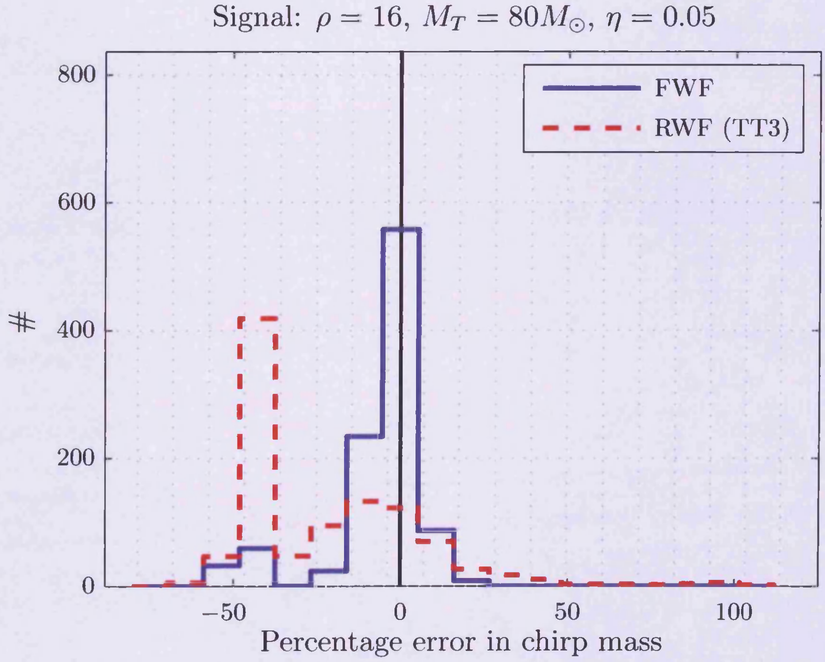

FIGURE 4.28: Histogram of the percentage error in chirp mass for a high SNR, high mass signal of symmetric mass ratio $\eta = 0.05$. This 0.5PN template family performs much better than the RWF family, which has a clear bias.

4.6.3 Large SNR

At a large SNR of $\rho = 64$ the 0.5PN template family also shows improvement in parameter estimation, sometimes at low mass as well as high mass. However, it should be noticed that due to the large SNR, the errors are generally small for both template families.

Large SNR - least improved Figure 4.29 and Figure 4.30 show two cases where the RWF template family performs as well as or better than the 0.5PN templates at large SNR.

Large SNR - most improved Figure 4.31 and Figure 4.32 show two cases where the 0.5PN template family outperforms the RWF family at large SNR.

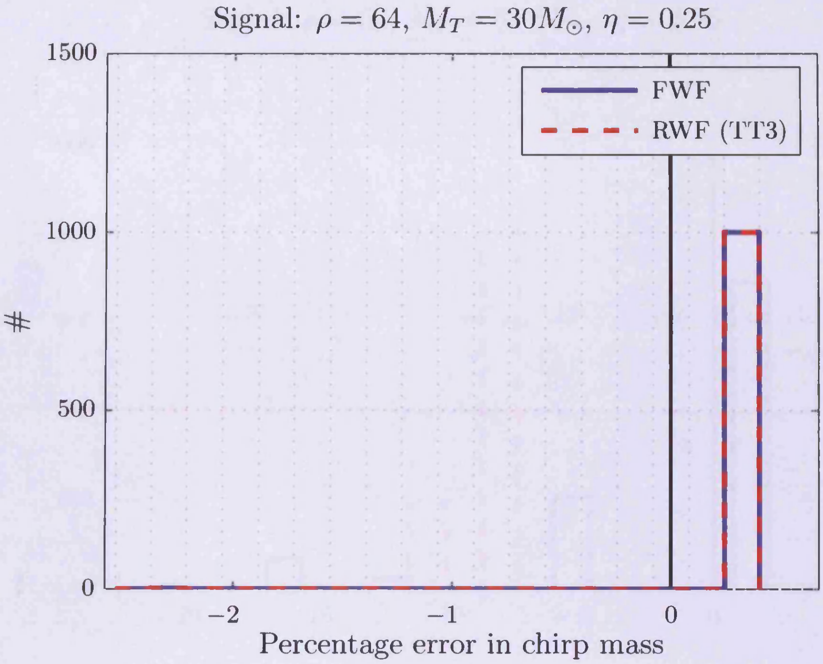

FIGURE 4.29: Histogram of the percentage error in chirp mass for a large SNR, low mass signal of equal mass. The results are indistinguishable.

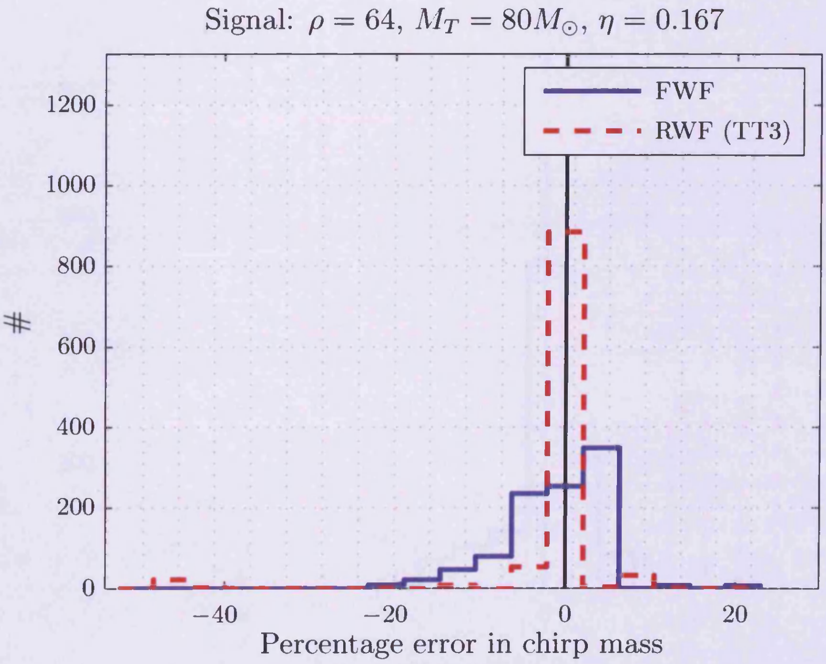

FIGURE 4.30: Histogram of the pecentage error in chirp mass for a large SNR, high mass signal of symmetric mass ratio $\eta = 0.167$. This is one of the few cases of a high mass signal where the RWF templates perform better than the 0.5PN templates.

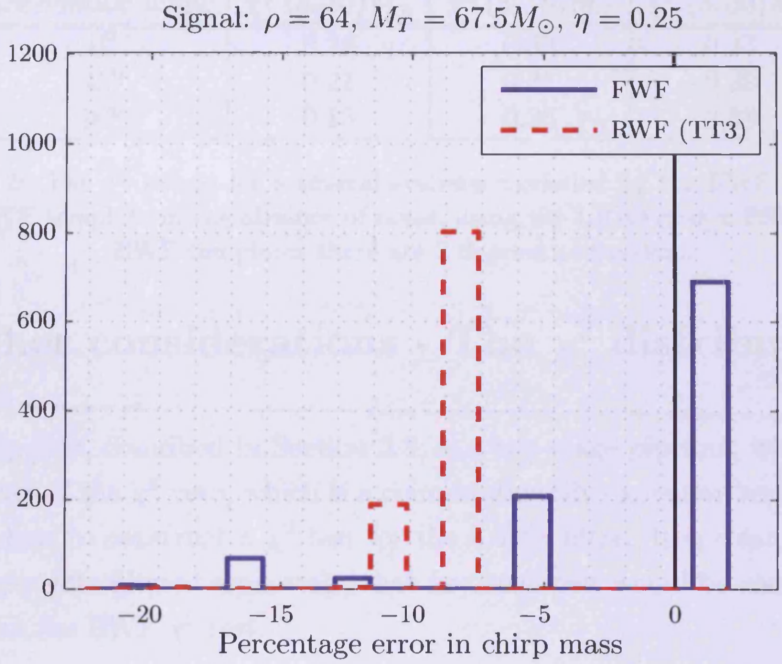

FIGURE 4.31: Histogram of the percentage error in chirp mass for a large SNR, high mass signal of equal mass. The 0.5PN templates outperform the RWF templates.

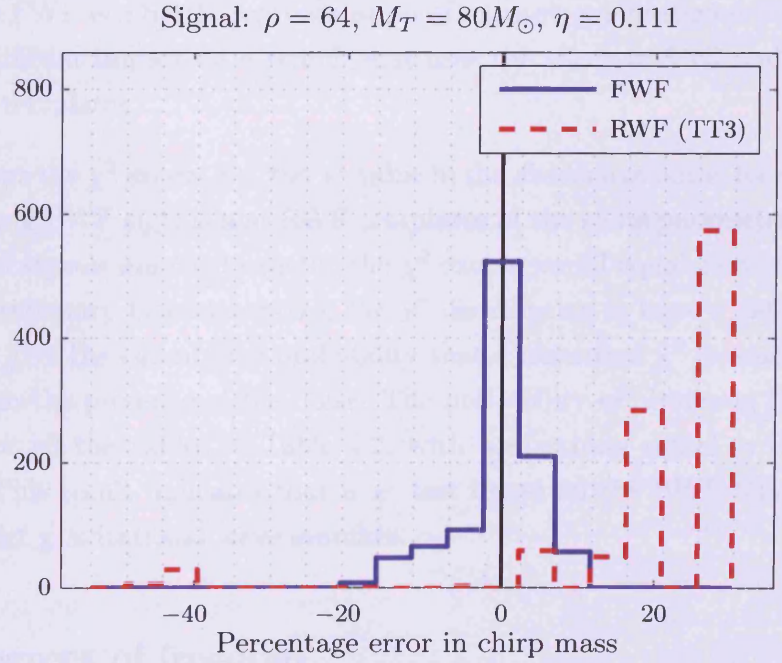

FIGURE 4.32: Histogram of the percentage error in chirp mass for a large SNR, high mass signal of symmetric mass ratio $\eta = 0.111$. The 0.5PN templates outperform the RWF templates.

Inclination angle	χ^2 $(3,10)M_\odot$	χ^2 $(3,15)M_\odot$	χ^2 $(3,30)M_\odot$
0^0	0.25	0.33	0.33
45^0	0.21	0.31	0.39
90^0	0.15	0.26	0.38

TABLE 4.2: The χ^2 excess for a several systems modelled by the FWF and filtered with a RWF template in the absence of noise, using the LIGO design PSD. N.B.: for RWF templates there are 2 degrees of freedom.

4.7 Other considerations - The χ^2 distribution

The LIGO pipeline, described in Section 3.3, is a two-stage pipeline, where the second stage makes use of the χ^2 veto, which is a computationally expensive test. Here, we will not consider how to construct a χ^2 test for the 0.5PN filter. It is clear, however, that with six components filtered separately, that any such test would be considerably more expensive than the RWF χ^2 test.

4.7.1 The χ^2 test with RWF templates and FWF injections

We have seen in Figure 4.2 that the spectra of the FWF and the RWF can differ greatly and since the FWF is a better representation of nature's gravitational waves, one might expect a significant impact on a search that uses the effective SNR and χ^2 veto based on the RWF templates.

Table 4.2 shows the χ^2 excess, i.e, the χ^2 value in the absence of noise, for several systems computed using FWF signals and RWF templates of the same parameters. N.B.: if the templates and signals matched exactly, the χ^2 excess would equal zero. However, in the presence of stationary Gaussian noise, the χ^2 distribution is known [39], which can be integrated to give the cumulative probability that a measured χ^2 is consistent with the template given the presence of the noise. The probability of obtaining the χ^2 excesses, or greater, for all the values in Table 4.2, with a matching signal in Gaussian noise, is $\sim$ 100%. This result indicates that a χ^2 test based on the RWF template does not adversely affect gravitational wave searches.

4.7.2 Degrees of freedom

The RWF filtering algorithm has two degrees of freedom, one for each phase of the filter. The 0.5PN filter has six components and therefore six degrees of freedom, although the constraint placed on the filter is likely to have a large effect on the χ^2 distribution.

Figure 4.33 and Figure 4.34 show the distribution of the SNR time-series for Gaussian noise filtered using the unconstrained 0.5PN filter with templates of mass-ratio 1:2 and 1:49 . The histogram, as expected, follows a classic χ^2 distribution with six degrees of freedom.

4.7.3 A signal-based veto included in the filter?

The constraint on the 0.5PN filter is, effectively, a signal-based veto. A value in the SNR time series is rejected if it does not pass the constraint, i.e. if it does not look like a signal. We therefore expect the χ^2 distribution to be very different with the constraint implemented. Figure 4.35 and Figure 4.36 show the χ^2 distribution for the same templates as above, but with the constraint applied, which has a dramatic effect (note the change in the y-axis from Figure 4.33 and Figure '4.34). There were 262144 points[9] in the time-series and all but 1133 and 5044 were discarded for the $(10, 20)M_\odot$ and $(1, 49)M_\odot$ constrained templates respectively.

This result is highly significant as it gives rise to the possibility that the FAR could be dramatically reduced in a gravitational wave search using the 0.5PN filter. It is also promising to see that the same effect is also impressive for the large mass ratio system where the constraint is less restrictive.

---

[9] Sampled at 4096 Hz, a total duration of 64 s.

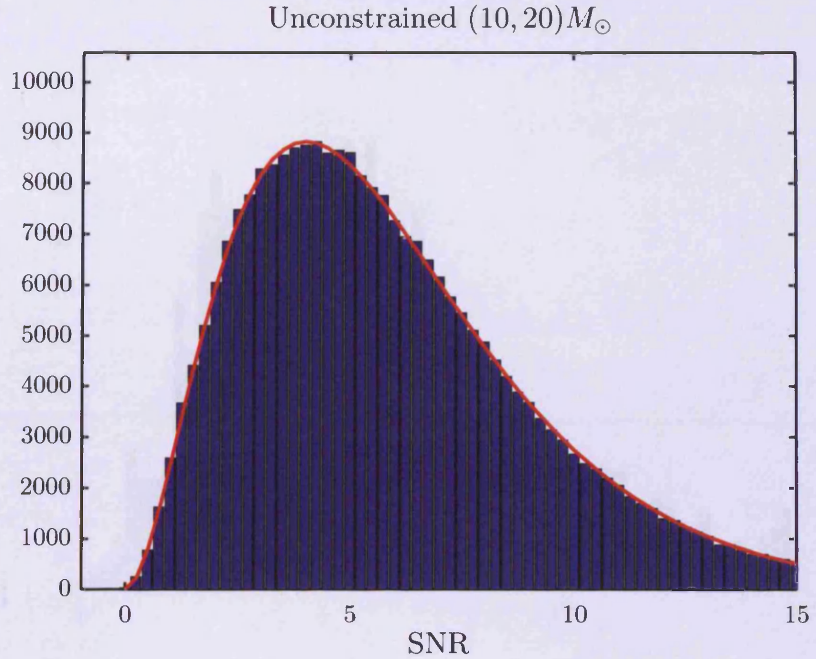

FIGURE 4.33: Histogram of the SNR time series with the unconstrained 0.5PN filter. As expected the distribution follows a classic χ^2 distribution with six degrees of freedom (red). The template has component masses $(10, 20)M_{\odot}$

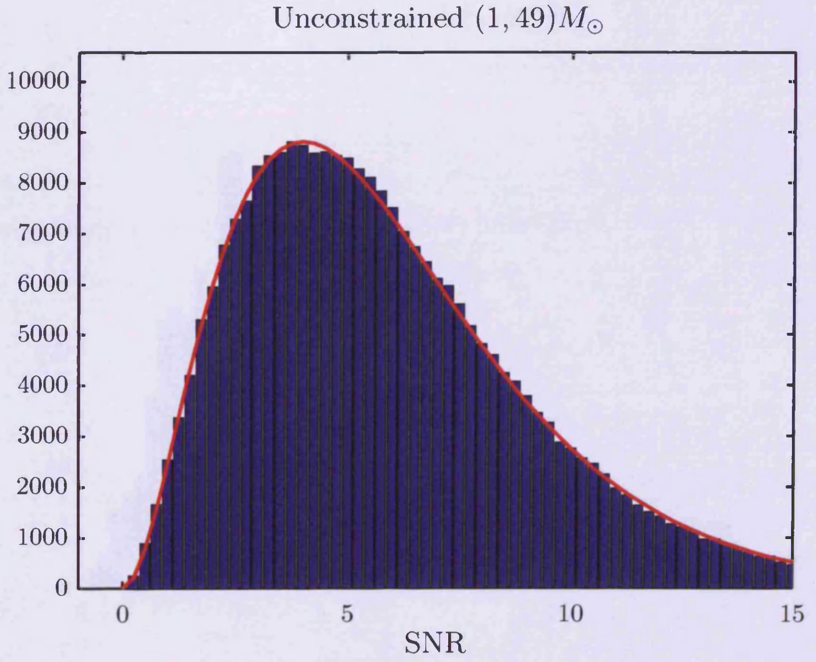

FIGURE 4.34: Histogram of the SNR time series with the unconstrained 0.5PN filter. As expected the distribution follows a classic χ^2 distribution with six degrees of freedom (red). The template has component masses $(1, 49)M_{\odot}$

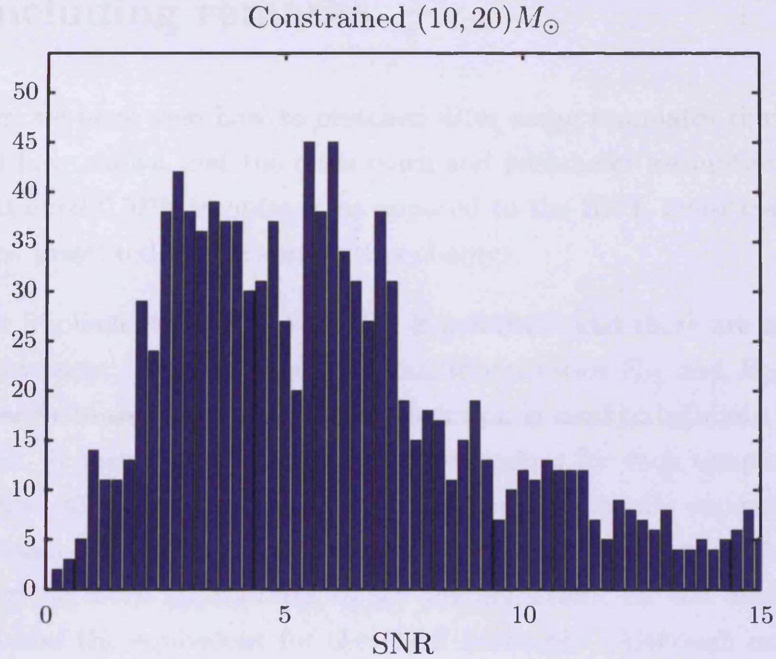

FIGURE 4.35: Histogram of the SNR time series with the 0.5PN filter with all null values removed. The template has component masses $(10, 20)M_\odot$. N.B.: the y-axis limits are markedly different to those in Figure 4.33.

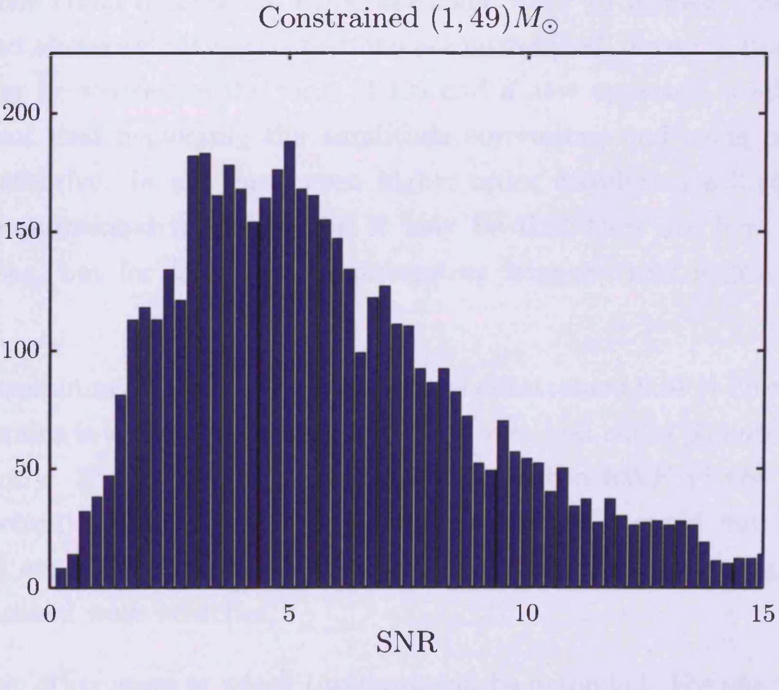

FIGURE 4.36: Histogram of the SNR time series with the 0.5PN filter with all null values removed. The template has component masses $(1, 49)M_\odot$. N.B.: the y-axis limits are markedly different to those in Figure 4.34.

4.8 Concluding remarks

In this chapter, we have seen how to matched filter using templates that are 0.5PN in amplitude and have shown that the mass reach and parameter estimation are improved with the constrained 0.5PN templates, as opposed to the RWF templates, which fulfils the motivations presented at the start of the chapter.

The constraint implemented in this chapter is primitive and there are many potential areas for improvement. For one thing, the maximum ratios R_{12} and R_{13} are currently tuned for a specific mass range and a fitting function is used to estimate how they vary across the bank. It may be that computing these values for each template greatly improves the results, although that would likely be computationally expensive. Moreover, the constraint was set using the relative amplitudes of the individual harmonics, but it would in fact be more appropriate to set the constraint on the maximum allowed ratio of (4.49) and the equivalent for the third harmonic. Although not discussed in this chapter, the additional complexity of the 0.5PN filtering algorithm does lead to longer processing times, which may be a practical consideration when performing a search for gravitational waves. Despite the above concerns, the results presented here are promising and already proffer improvements on the existing RWF templates.

In principle, one could extend the three harmonic filter to include higher harmonics, but at 1PN and above amplitude corrections are introduced, meaning that the template could no longer be written in the form (4.12) and a new approach would be required. It may turn out that neglecting the amplitude corrections and using only the higher harmonics is effective. In any case, *even* higher order waveforms will place additional strains on computational resources and it may be that they are best used not as a detection device, but for following up interesting triggers from a gravitational wave search.

However, by examining the χ^2 distribution of the constrained 0.5PN filter we have seen that the constraint is a very effective signal-based veto and could *potentially* reduce the FAR significantly. If used in a two-stage pipeline, with a RWF χ^2 test at the second stage, a reduction in triggers due to the decrease in FAR could mitigate the extra computational expense of the 0.5PN filter making it a viable algorithm to be used in future gravitational wave searches.

There are many other ways in which this work can be extended. For one thing the tests in this chapter consider a single IFO, yet it would be interesting to study the effects on coincidence and the FAR in the context of a complete gravitational wave search, similar to that in Chapter 3. It would also be interesting to apply the 0.5PN filtering algorithm to IMR waveforms, which should be used in gravitational wave searches for CBCs of the mass ranges studied in this chapter.

Chapter 5

A tapering window for time-domain templates and simulated signals

---

Inspiral signals from binary black holes, in particular those with masses in the range $10M_{\odot} \lesssim M \lesssim 1000M_{\odot}$, may last for only a few cycles within a detector's most sensitive frequency band. The spectrum of a square-windowed time-domain signal could contain unwanted power that can cause problems in gravitational wave data analysis, particularly when the waveforms are of short duration. There may be leakage of power into frequency bins where no such power is expected, causing an excess of false alarms.

In this chapter a method of tapering TD waveforms is presented that significantly reduces unwanted leakage of power, leading to a spectrum that agrees very well with that of a long duration signal. The tapered window also decreases the false alarms caused by instrumental and environmental transients that are picked up by templates with spurious signal power. The suppression of background is an important goal in noise-dominated searches and can lead to an improvement in the detection efficiency of the search algorithms.

The tapering method has proved very useful and has been used in all of the studies in Chapter 4.

5.1 Motivations

We have seen in Chapter 3 that gravitational wave searches are noise dominated and must use techniques to extract the signal from the noise. In Chapter 3 the matched filter was used; other examples include: wavelet transforms for transient signals of unknown shape [65, 66], coherent search methods for burst signals [67], etc. Moreover, we have also discussed vetoes based on the expected signal evolution [39] and instrumental and environmental monitors [68] that have been developed over the past decade to improve detection probability and mitigate false alarms. Detecting a signal buried in non-stationary noise is a challenging problem as some types of non-stationary noise artefacts can partially mimic the signal.

Many of these techniques involve the computation of a correlation integral in which band-passed data are multiplied by the FD model waveform or the discrete Fourier transform (DFT) of the TD model (see, e.g., [69]). Here we will again consider a matched filtering search for inspiral signals where the DFT of a TD waveform is used to construct the correlation. A problem that has not been adequately addressed (see, however, [70]) in this context is the effect of the window that is used in chopping a TD signal before computing its DFT.

Inevitably, all signal analysis algorithms use, implicitly or explicitly, some form of window function. An inspiral waveform sampled from a time when the signal's instantaneous frequency enters a detector's sensitive band until the time when it reaches the FLSO implicitly makes use of a square window. Signal analysis literature is full of examples of artefacts caused by the use of such window functions. Examples are: leakage of power from the main frequency bins where the signal is expected to lie into neighbouring bins, loss of frequency resolution and corruption of parameter estimation [71]. In this chapter we will explore the problems caused by using a square window and suggest an alternative that cures some of the problems.

There is no unique, or favoured, windowing method. One is often guided by the requirements of a particular analysis at hand. In this case, a square window is especially bad since the leakage of power outside the frequency range of interest can lead to increased FAR and poorer estimation of parameters. One reason for increased FAR could be that the noise glitches in the detector look more like the untapered/square-windowed waveform and less like a tapered one. Here we will explore the effect of a smoother window function, presented in Section 5.2, which has a far steeper fall-off of power outside the frequency range of interest. Use of this window has cured several problems we had with a square window. The effect of the new method on waveform spectra is shown in in Section 5.3.

Section 5.4 shows how tapering helps in a more reliable signal spectral estimation and hence a proper determination of the expected signal-to-noise ratio. Spectral contamination is worse for larger mass black hole binaries as they are in the detector's sensitive band for a shorter time and the window function can only extend over a short time. It is for such signals that the tapered window presented here offers the most improvement. In Section 5.5 we will see how the rate of triggers from a matched filtered search can vary depending on the kind of window function used. Finally, in Section 5.6 we see what effect the window function has on parameter estimation, before drawing the conclusions of the study in Section 5.7.

5.2 Window functions and their temporal and spectral characteristics

Let $h(t)$ denote a continuous differentiable function, for example a gravitational wave signal emitted by a CBC, and let $\widetilde{h}(f)$ denote the FT of $h(t)$ defined by

$$\widetilde{h}(f) = \int_{-\infty}^{\infty} h(t)\, \exp(2\pi i f t)\, \mathrm{d}t. \tag{5.1}$$

In reality the signal does not really last for an infinite time. The FT of a signal of finite duration lasting, say, from $-T/2$ to $T/2$, can be represented either by setting the limits of the integral to go from $-T/2$ to $T/2$ or by using a window function. The latter is preferred so as to preserve the definition of the FT.

A window function is a function that has either a finite support or falls off sufficiently rapidly as $t \longrightarrow \pm\infty$. Two simple windows that have finite support are the square window $s_T(t)$ defined by

$$s_T(t) = \begin{cases} 1 & \text{for} \quad -\frac{T}{2} \leq t \leq \frac{T}{2} \\ 0 & \text{otherwise}. \end{cases} \tag{5.2}$$

and the triangular window $b_T(t)$ defined by

$$b_T(t) = \begin{cases} (1 - 2|t|/T) & \text{for} \quad -\frac{T}{2} \leq t \leq \frac{T}{2} \\ 0 & \text{otherwise}. \end{cases} \tag{5.3}$$

Neither the square nor the triangular window are differentiable everywhere. As a result, they are not functions of finite bandwidth. In other words, their FTs, $\widetilde{s}_T(f)$ and $\widetilde{b}_T(f)$, do not have finite support in the FD: $|\widetilde{s}(f)| > 0$ for $-\infty \leq f \leq \infty$. In the case of a square window the FT $\widetilde{s}(f)$ is a sinc function, $|\widetilde{s}_T(f)| = T\mathrm{sinc}(\pi f T)$, which is peaked at $f = 0$, with a width π/T and falls off as f^{-1} as $f \longrightarrow \pm\infty$. The lack of finite support in the Fourier domain could sometimes cause problems, especially when the width, T, of the window in the time domain (TD) is too small. For functions that have infinite bandwidth the sampling theorem does not hold but this is not a serious drawback if the

FT falls off sufficiently fast above the Nyquist frequency. However, there could be other issues when the window leads to leakage of power outside a region of interest as we shall see below.

5.2.1 The Planck-taper window function

A signal $h(t)$ with the window $w_T(t)$ applied to it, in other words the windowed signal $h_w(t)$, is defined by

$$h_w(t) = h(t) w_T(t). \tag{5.4}$$

The convolution theorem states that the FT of the product of two functions $h(t)$ and $w_T(t)$ is the convolution of individual FTs:

$$\begin{aligned} \widetilde{h}_w(f) &= \int_{-\infty}^{\infty} h(t) w_T(t) \exp(2\pi i f t) \mathrm{d}t\,, & (5.5\text{a}) \\ &= \int_{-\infty}^{\infty} \widetilde{h}(f') \widetilde{w}_T(f - f') \mathrm{d}f'\,, & (5.5\text{b}) \end{aligned}$$

We can now see why a window whose power in the FD does not fall off sufficiently rapidly might be problematic. The convolution integral will have contributions from all frequencies. Suppose we are interested in matched filtering the data with an inspiral signal from a compact coalescing binary whose instantaneous frequency varies from f_a, at time t_a, to f_b, at time t_b. One would normally achieve this by using a square window $s_T(t)$ that is centred at $(t_a + t_b)/2$ with width $T = t_b - t_a$. However, we can see from (5.5b) that the convolution integral will have contributions from outside the frequency range of interest.

To circumvent this problem we define a new window function that falls off rapidly outside the frequency range of interest. Inspired by the tapering function used in Damour et al. [72], we define the new function $\sigma(t)$ by

$$\sigma_T(t;\epsilon) = \begin{cases} & 0, \quad \text{for} \quad t \le t_1\,, \\ \dfrac{1}{\exp(z(t)) + 1}, & z(t) = \dfrac{t_2 - t_1}{t - t_1} + \dfrac{t_2 - t_1}{t - t_2}, \quad \text{for} \quad t_1 < t < t_2\,, \\ & 1, \quad \text{for} \quad t_2 \le t \le t_3\,, \\ \dfrac{1}{\exp(z(t)) + 1}, & z(t) = \dfrac{t_3 - t_4}{t - t_3} + \dfrac{t_3 - t_4}{t - t_4}, \quad \text{for} \quad t_3 < t < t_4\,, \\ & 0, \quad \text{for} \quad t_4 \le t\,, \end{cases} \tag{5.6}$$

where

$$t_1 = -\frac{T}{2}\,, \tag{5.7}$$

$$t_2 = -\frac{T}{2}(1-2\epsilon)\,, \tag{5.8}$$

$$t_3 = \frac{T}{2}(1-2\epsilon)\,, \tag{5.9}$$

$$t_4 = \frac{T}{2}\,. \tag{5.10}$$

Here T is the width of the window and ϵ is the fraction of the window width over which the window function smoothly rises from 0 at $t = t_1$ to 1 at $t = t_2$ or falls from 1 at $t = t_3$ to 0 at $t = t_4$. We shall call $\sigma(t)$ the *Planck-taper window* as the basic functional form is that of the Planck distribution. The motivation for choosing this window function is to reduce the leakage of power in the FD but at the same time not to lose too much of the length of the signal in the TD. The choice of ϵ will affect both aspects significantly. Figure 5.1 shows the window function for several choices of the parameter $\epsilon = 0.01, 0.033$ and 0.1 with their corresponding spectra. At lower frequencies the spectrum of the Planck-taper window falls off at the same rate (i.e., $1/f$) as a square window. But beyond a certain frequency $f_0 \sim (\epsilon T)^{-1}$, the spectrum falls off far faster.

A key feature the Planck-taper window is the fraction of the window width that is flat, i.e., the choice of ϵ, which we will automate to be waveform-dependent, see section 5.2.2 below.

5.2.2 Implementation of the window

We may discretise (5.6) by replacing t, t_1, t_2, t_3, t_4 with the array indices j, j_1, j_2, j_3, j_4. In this notation the parameter epsilon is approximated by $\epsilon \simeq (j_2 - j_1)/N$, where N is the number of data points in the waveform. The start and end of the waveform are denoted by j_1 and j_4, respectively. The values of j_2 and j_3 have to be chosen judiciously to avoid leakage of power. We shall choose j_2 and j_3 to be the array indices corresponding to the second stationary point after j_1 and before j_4 (see Figure 5.2). Applying the transition stage of σ from a crest/trough ensures that the window does not have a sudden impact on the behaviour of the waveform. The first stationary point would not be an appropriate choice as it may occur within only a few array points of j_1 or j_4, causing ϵ to be too small. One could choose the 3rd, 4th or 5th, but using such later maxima would reduce the genuine power of the waveform more than what might be acceptable.

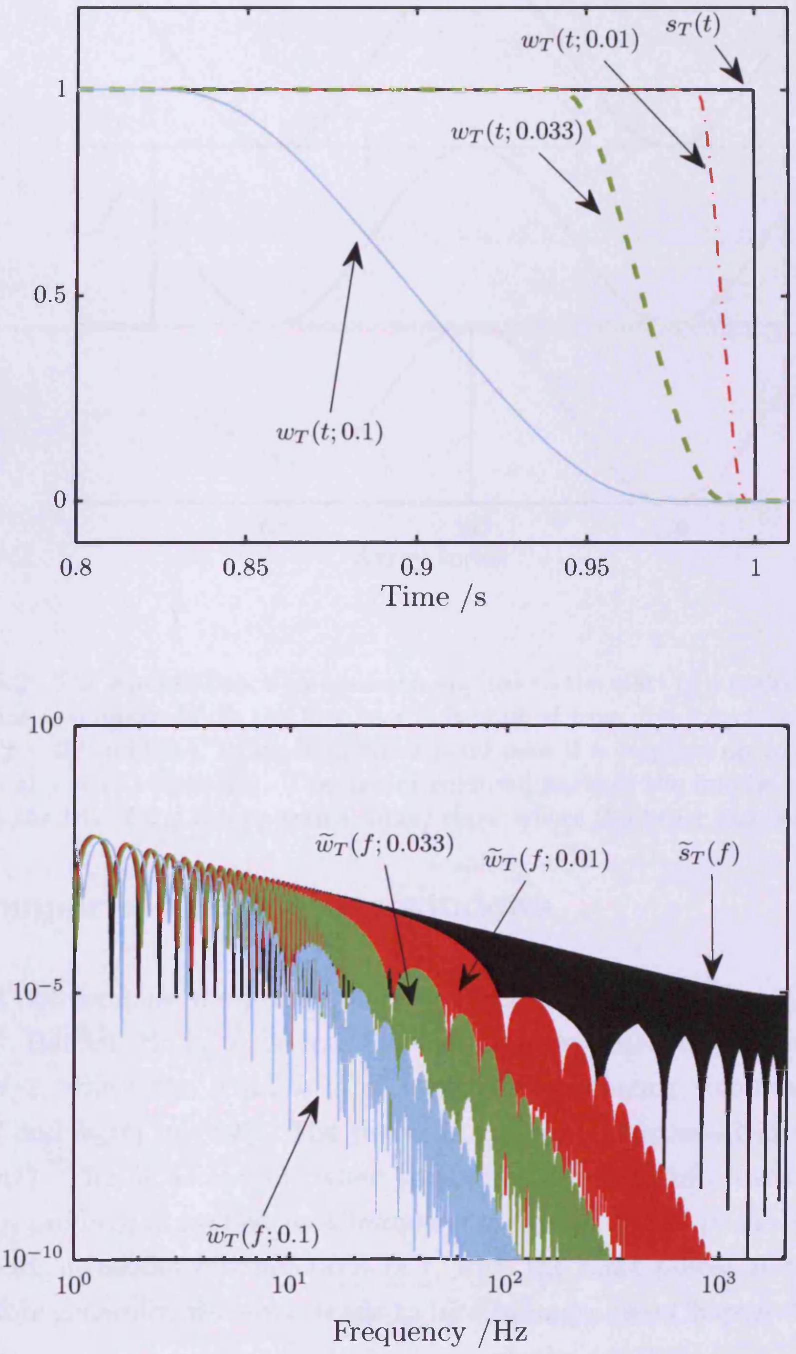

FIGURE 5.1: The Planck-taper window in the TD for three different choices of the parameter $\epsilon = 0.01$, 0.033, 0.1, (top). For reference the square window with the same effective width as the Planck-taper window has also been plotted. The bottom plot shows their corresponding spectra.

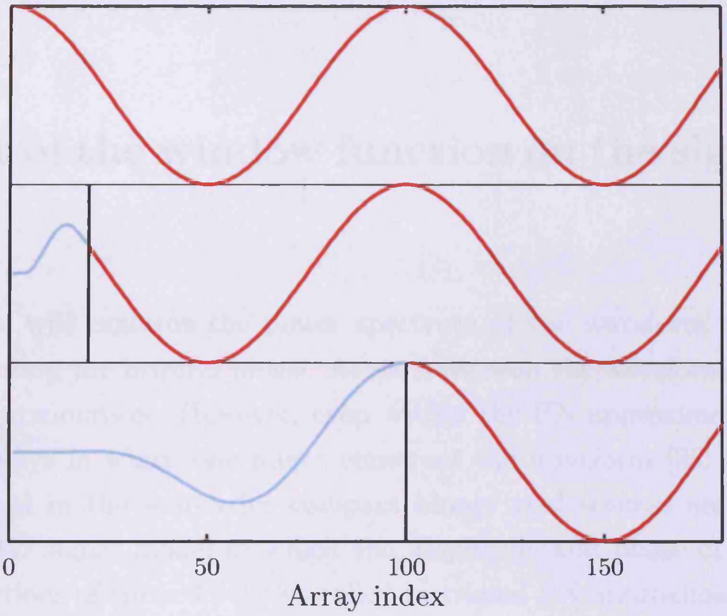

FIGURE 5.2: The window function has been applied to the start of a cosine wave (top curve) using two methods. In the first case it is applied from $j = 1$ up to an arbitrary choice of $j = 20$ (middle), whereas in the second case it is applied up to the second maximum at $j = 100$ (bottom). The lighter coloured parts of the middle and bottom curves (to the left of the black vertical lines) show where the taper has been applied.

5.2.3 Comparison with other windows

Here we shall not compare the performance of Planck-taper with other commonly used windows, e.g., Bartlet, Hann or Welch. Such windows transition between 0 and 1 over $j = 1, \ldots, N/2$, where the window is of length N, producing significant differences between $h(t)$ and $h_w(t)$ in (5.4). The power is therefore suppressed at the beginning and end of $h(t)$. This is acceptable when computing the PSD of a data segment, but would cause a problem if applied to a template waveform as the phase and amplitude of $h(t)$ are both instantaneous functions of t, with the most power at the end of the waveform. More generally, the noise tends to be stationary (see Chapter 3) whereas the signal is not.

Windows with properties similar to Planck-taper, such as having a central flat region, do exist. For example, the Tukey window [73], which has been used in gravitational-wave data analysis recently [74], may offer a good comparison. However, a key feature in our study of the Planck-taper window is the waveform-dependent adjustment of j_2 and j_3. Whilst this automation could be considered separately from the Planck-taper window and used on other windows defined by the points $j_{1,2,3,4}$, we have not done so here.

Given the shared features of the Tukey window with Planck-Taper one might expect similar results.

5.3 Effect of the window function on the signal spectrum

In this section we will examine the power spectrum of the waveform of a coalescing binary emitted during the inspiral phase. As we have seen the waveforms are modelled using the PN approximation. However, even within the PN approximation, there are several different ways in which one might construct the waveform [25, 55]. Two such models widely used in the search for compact binary coalescences are TT3 and the SPA. TT3 is a TD signal model in which the amplitude and phase of the signal are both explicit functions of time. In the so-called restricted PN approximation the signal consists of the dominant harmonic at twice the orbital frequency, but not higher order PN corrections consisting of other harmonics, and the phase is a PN expansion that is currently known to $\mathcal{O}(v^7)$ in the expansion parameter v – the relative velocity of the two stars. The SPA is the Fourier transform of the TT3 model obtained by using the stationary phase approximation to the Fourier integral [75]. A template belonging to the TT3 model is defined for times when the gravitational wave frequency is within the detector's sensitivity band until it reaches FLSO. This means one is in effect multiplying a square window with a continuous function.

Figure 5.3 shows the SNR integrand of the SPA, computed using the initial LIGO design PSD [25]. The inspiral waveform is defined from a lower cut-off frequency of 35 Hz up to its FLSO, for $20\,M_\odot$ and $80\,M_\odot$ equal-mass binaries. The DFT of the TT3, generated between the same frequencies, with a square window (or rather no window), labelled H_S, and with the Planck-taper window, labelled H_σ, are also plotted. Where the Planck-taper window is used the excess power (that above FLSO) decreases rapidly and the spectrum is closer to that of the SPA.

5.4 Effect of the window function on the estimation of the signal-to-noise ratio

Gravitational wave searches for known signals, such as those emitted by CBCs [1, 29], rely upon signal models for two primary reasons. Firstly, they are used as templates to matched filter the data. Secondly, they are injected into the data as simulated signals

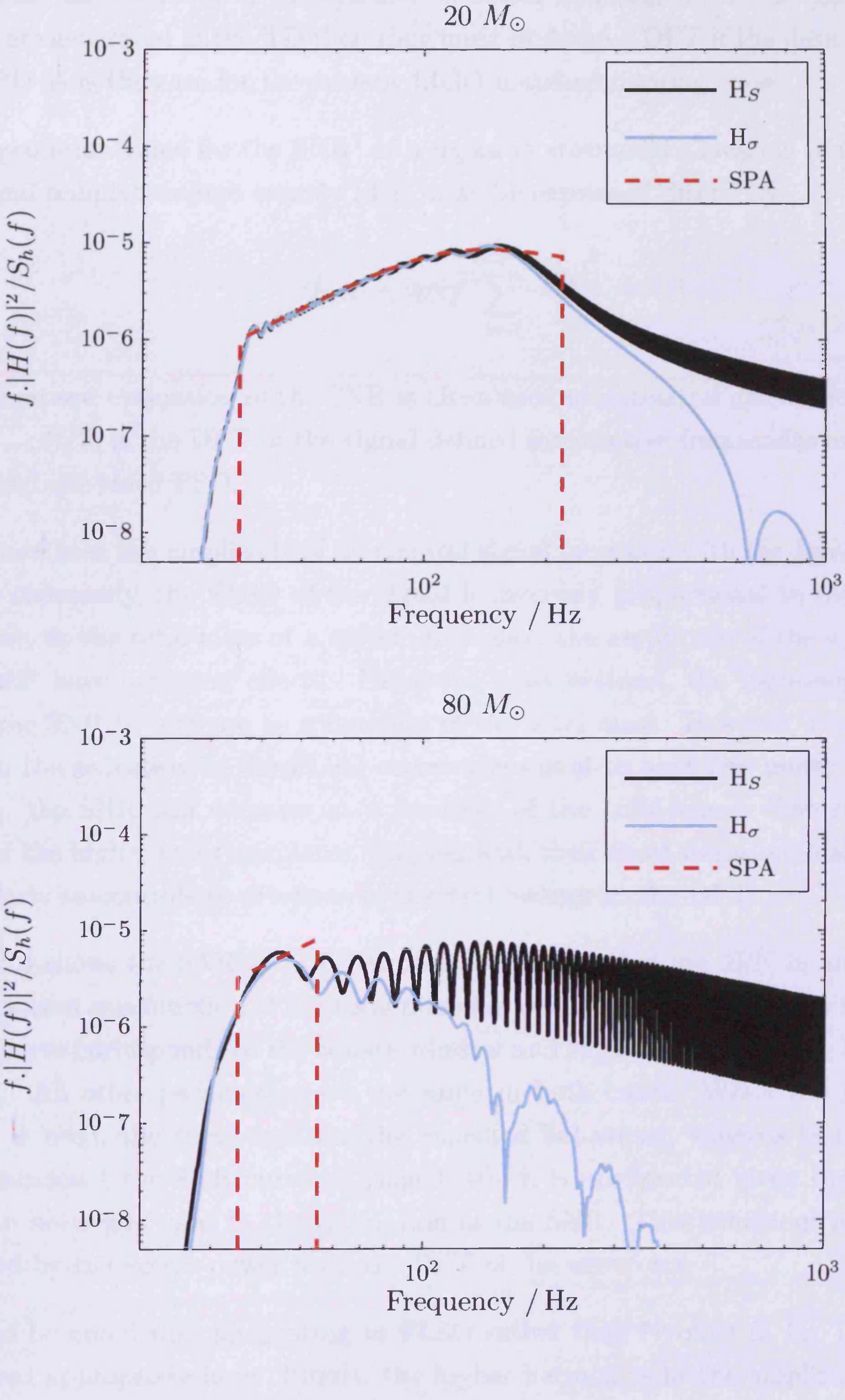

FIGURE 5.3: The SNR integrand produced with both the square and Plank-taper window, where the waveform is generated from a frequency of 35 Hz to the FLSO of the source, computed using the LIGO design PSD for sources of total mass $20M_\odot$ (top) and $80M_\odot$ (bottom). In both cases, the SNR integrand falls off far faster with the use of the Planck-taper window compared to the square window.

to estimate the efficiency of the detector to detect such signals. If the signal/template models are generated in the TD then they must undergo a DFT if the data are analysed in the FD as is the case for the current LIGO matched filtering code.

The expectation value for the SNR^2 of a signal in stationary Gaussian noise, when the signal and template match exactly (4.2), may be expressed discretely

$$\langle h, h \rangle \simeq 4\Delta f \sum_{k=1}^{N/2-1} \frac{|\widetilde{h}_k|^2}{S_{nk}}, \tag{5.11}$$

The discretised evaluation of the SNR is often used in numerical calculations. Here $\widetilde{h}_k$, $k = 0, \ldots, N/2$, is the DFT of the signal defined for positive frequencies and S_{nk} is the discretised one-sided PSD.

As we have seen the amplitude of an inspiral signal increases with the total mass of the system; conversely, the FLSO of the signal is inversely proportional to the total mass. Therefore, as the total mass of a system increases, the amplitude of the signal and the FLSO will have opposing effects. For lower mass systems, the increasing amplitude causes the SNR to increase as a function of the total mass. However, for higher mass systems, the reduction in the FLSO causes the signal to have less power in band. As a result, the SNR will decrease as a function of the total mass. The relatively low FLSO of the higher mass templates, coupled with their short duration, lead them to be particularly susceptible to artefacts of spectral leakage in the DFT.

Figure 5.4 shows the SNR for TT3 inspiral waveforms that are 2PN in amplitude and phase, plotted as a function of the total mass for two choices of the window function: the dashed curve corresponds to the square window and the solid curve to the Planck-taper window. All other parameters are the same in both cases. When the Planck-taper window is used, the curve exhibits the expected behaviour, whereas in the case of a square window , the SNR curve is 'jagged' which is unexpected given that stationary Gaussian noise was used in the estimation of the SNR. This behaviour is most likely explained by the excess power from the DFT of the waveform.

It should be noted that integrating to FLSO rather than Nyquist in Eq. (5.11), is not considered appropriate here. Firstly, the higher harmonics in the amplitude corrected waveforms contain power above FLSO (which becomes more significant for high mass systems). Secondly, cutting off the integration at FLSO is essentially the application of a square window to the template waveform in the frequency domain. This will lead to leakage of power in the time domain which is not a desirable feature. The problem of using a square-windowed TD template as our matched filter is not that there is power

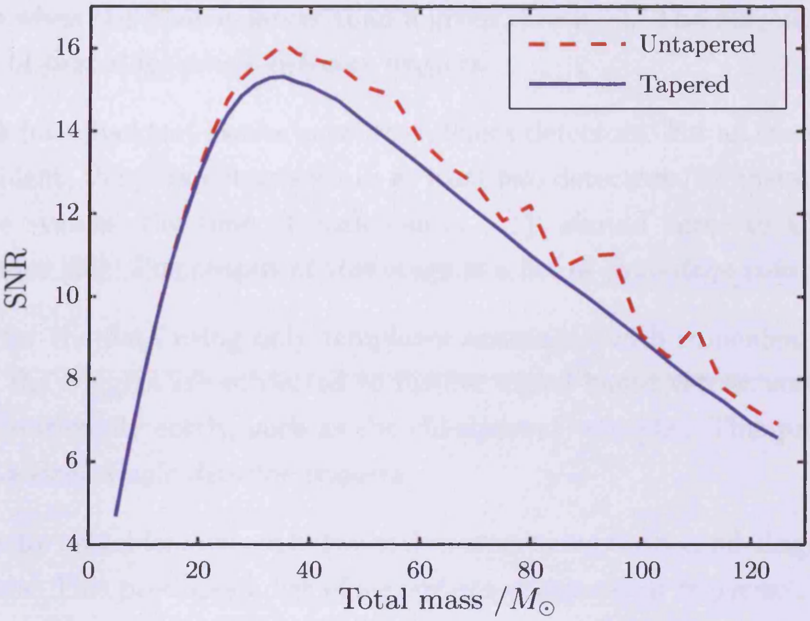

FIGURE 5.4: The SNR vs. the total mass of the source for signals corresponding to compact binary systems directly overhead a detector of initial LIGO design PSD. The SNR is obtained using the DFT of TD waveforms with a square window (dashed curve) and with the Planck-taper window (solid curve). Here the systems are overhead the detector at an effective distance of 65 Mpc, using a fixed mass ratio of 5 : 1 and a fixed inclination angle of 45°.

above FLSO; it is that the excess power in this region, present due to windowing, but not present in a genuine signal will lead to unnecessary false alarms in a search.

5.5 Effect of window functions on trigger rates

To assess the effect that tapering of templates has on trigger rates, we have applied the LSC CBC pipeline [1, 27–30] to data taken during the LIGO's 4th science run (S4), which took place from February 22 - March 23, 2005. The basic topology of the pipeline is similar to that used in many previous searches [28, 29], with the pipeline used in [1] described in detail in Chapter 3, from which we recall the trigger generation:

- The template bank is chosen such that the loss of SNR due to having a finite number of templates is no more than 3% for any signal belonging to a given family of waveforms [37, 76].

- Matched filter the data with the generated templates. A trigger is generated at times when the SNR is larger than a given threshold. The output of this stage is a list of *first-stage single-detector triggers.*
- Check for coincident events between different detectors. For an event to be deemed coincident, the parameters seen in at least two detectors (for instance, the masses of the system, the time of coalescence, ...) should agree to within a certain tolerance [38]. The output of this stage is a list of *first-stage coincident triggers.*
- Re-filter the data using only templates associated with coincident triggers. This time, the triggers are subjected to further signal-based vetoes, some of which are computationally costly, such as the chi-squared veto [39]. This produces a list of *second-stage single-detector triggers.*
- Check for coincident events between detectors using the second-stage single-detector triggers. This produces a list of *second-stage coincident triggers.*

In this study the data were filtered using the effective one-body (EOB) templates [25, 77, 78], tuned to recent results in numerical relativity [19, 20], with a total mass in the range $25 - 100 M_{\odot}$. This choice agrees with the templates used to search for signals from high-mass CBCs in data from LIGO's 5th science run (S5). Because the EOB waveforms used as templates contain the inspiral, merger and ringdown phases, there was no need to taper the end of the waveform. Therefore, in this case, the taper specified in (5.6) was only applied to the start of the waveform. Although this may reduce the effect the taper has in comparison to tapering both ends of an inspiral-only template, it is of more interest to evaluate the performance in a realistic search case. N.B.: the tapering window is *explicitly applied to the template waveform* where the length of the waveform is less than the length of the data segment that is matched filtered. In this study no window has been applied to the data segment.

Figure 5.5 shows the number of triggers as a function of total mass with and without tapering for the first and second stages of the pipeline. It can be seen that the number of triggers is generally higher when the templates are not tapered. The only exception seems to be the lowest mass bin in the second-stage coincident triggers, where the opposite is true. However, the difference in the number of triggers in this bin is not large, and is likely just a statistical anomaly. For first-stage single-detector triggers, the number of triggers using tapered templates is 84% of that obtained using un-tapered templates. The number of second-stage coincident triggers when using tapered templates is 71% of that obtained for un-tapered templates. The difference in trigger rates is more significant at higher masses. This is because the template waveforms for these systems terminate at a frequency within or below the most sensitive frequency band of the detector, making any leakage of power to higher frequencies more significant (see Figure 5.3). The reduced trigger rate indicates that applying the taper function to the templates could aid in reducing the false alarm rate in a search for high mass CBCs.

5.6 Effect of windowing on detection efficiency and parameter estimation

The same data used in section 5.5 were re-analysed, but with simulated gravitational wave signals (injections) added. The injections were of the same family as the templates used in section 5.5, allowing the detection efficiencies and accuracy of parameter estimation using tapered vs. untapered templates to be compared. There was negligible difference in the error in recovered chirp mass and arrival time at both single detector first stage triggers and coincident second stage triggers. Although the detection efficiency was not explicitly measured as a function of distance, the number of injections recovered was found to be nearly identical in the two cases, with less than 1% fewer injections found when using tapered templates. Given the vast reduction in the trigger rates shown in Section 5.5, this indicates that an improvement in detection efficiency *can be expected* when using tapered templates.

The above studies were performed first with tapering applied to the injections and then repeated without - the difference between the results was negligible.

5.7 Concluding remarks

The Planck-taper window leads to spectra for TD waveforms that more closely match their FD analogs, containing significantly less power at unexpected frequencies when compared with the use of a square window. This is achieved by automating the implementation of the window.

If tapering is applied to templates in a gravitational wave search the trigger rates are reduced, especially for high mass templates, without any significant change in detection efficiency. In a search, foreground triggers can be ranked by their probability of occurring as a background trigger; thus if background triggers are reduced, a given foreground trigger may appear more significant. Another benefit of reduced trigger rates is that the computational cost of a search will decrease. Indeed the studies here demonstrate that the Planck-taper windowing method would be beneficial when used in a high mass search.

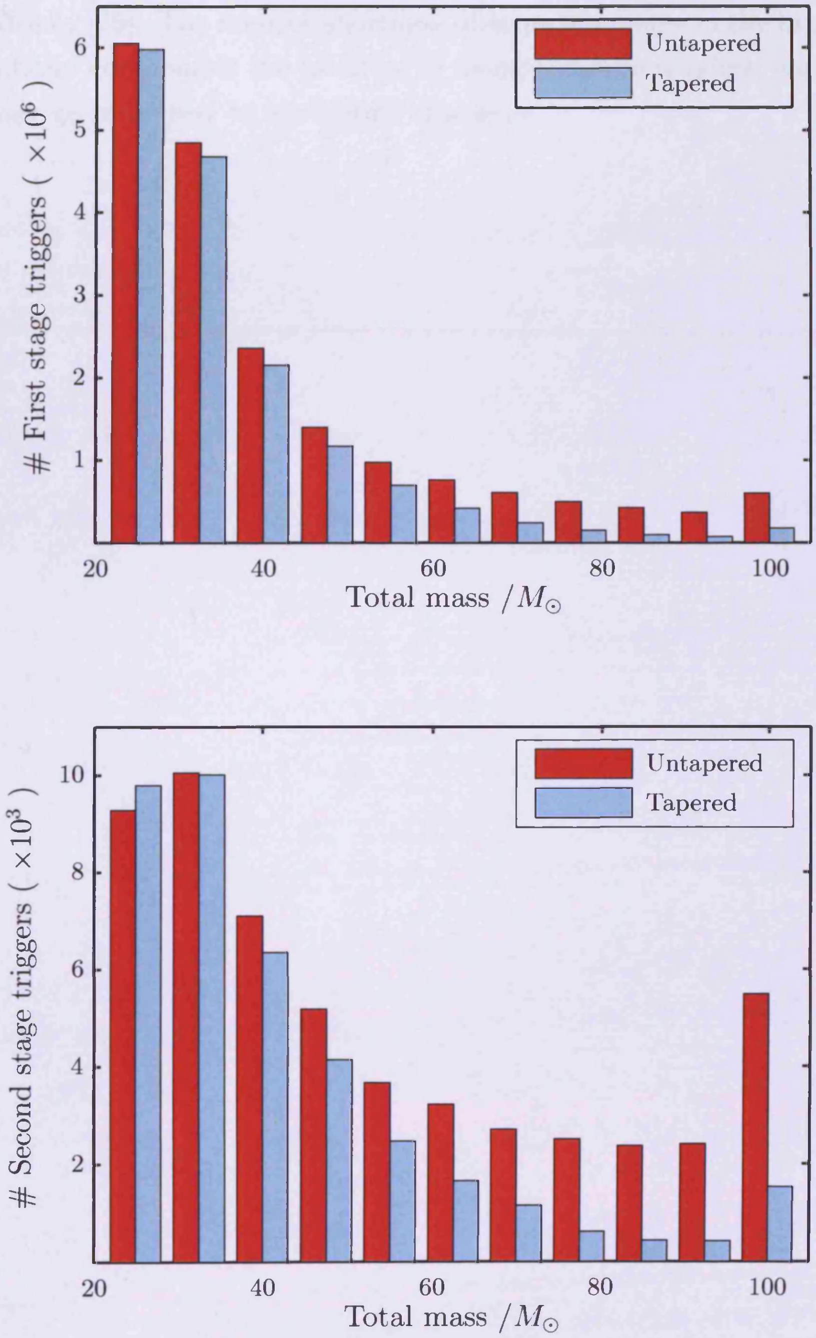

FIGURE 5.5: Number of triggers recovered by match filtering the S4 data with and without tapering applied to the templates for the first stage (top) and the second stage (bottom) where consistency checks and coincidence tests [38] in the time-of-arrival and masses of the component stars have been applied.

The tapering method could also be useful in low latency data analysis techniques where TD templates are divided into sub-templates of different frequency ranges, and match filtered individually [79]. The relative shortness of some templates in the higher frequency bands potentially compounds the problem of using a square window, and tapering the templates may go some way to alleviating this issue.

Chapter 6

Black Hole Hunter: The game that lets YOU search for gravitational waves

A collaboration of gravitational wave physics groups from the United Kingdom and Germany presented the exhibit 'Can you hear black holes collide?' at the Royal Society Summer Science Exhibition 2008 in London. The exhibit gave the public insight into how gravitational waves are generated, how gravitational wave detectors function, and how searches for gravitational waves are performed. The 'Black Hole Hunter' computer game was developed to illustrate the challenges of searching for a gravitational wave signal in noisy data. The game was popular with attendees at the exhibition and has subsequently been used in many other outreach projects. The game's website, *www.blackholehunter.org*, currently receives approximately one-thousand unique visitors each month.

6.1 Searching for gravitational waves

Gravitational wave experiments are in an exciting era. A global network of first generation IFOs have been used to search for gravitational waves and have already made statements about our Universe, e.g., [1, 29, 80, 81]. Furthermore, the detectors are currently undergoing upgrades to reach ever more impressive levels of sensitivity [13]. This provides an ideal opportunity to inspire public interest and excitement in science. There is a large outreach effort in the gravitational wave community, including public education centres [82], teaching projects in schools, and a travelling gravitational waves exhibit [83].

6.2 'Can you hear black holes collide?'

The Royal Society annually hosts a summer science exhibition at its offices in central London. This exhibition, which is open to the general public, aims to inform visitors of the latest developments and discoveries in all fields of science and inspire young people's interest and involvement in science. The Royal Society Summer Exhibition 2008 [84] consisted of twenty-three exhibits and two additional art and history of science exhibits each. These exhibits covered a vast range of scientific fields from bioscience to astrophysics, and the exhibition was attended by several thousand visitors over four days.

Among the exhibits selected for the summer exhibition in 2008 was 'Can you hear black holes collide?' presented by a collaboration of British and German gravitational wave researchers. Detectors such as LIGO and GEO are sensitive to gravitational waves with frequencies between approximately 50 Hz and a few thousand Hz. This range is comparable to frequency range of the human ear, motivating the choice of title.

The goals of this exhibit were two-fold: to give the public an idea of what gravitational waves are; and how we go about searching for them. The exhibition featured a short, looping video to attract visitors. A 'rubber sheet universe' was used to illustrate Einstein's concept of space-time and curvature and to demonstrate heuristically how orbiting bodies might emit gravitational radiation. A fully-functional table-top interferometer was used to explain and demonstrate to visitors the basic principles of laser interferometric detectors. In order to illustrate the methods and challenges involved in searching for gravitational waves, the 'Black Hole Hunter' game was available to play on multiple computers.

Additionally a group of researchers actively involved in gravitational wave science were stationed at the exhibit to talk to visitors and to answer their questions and a variety of handouts were distributed which provided visitors with website addresses and further information on the exhibit allowing them to continue learning more on gravitational waves after the exhibition.

6.3 The Black Hole Hunter game

The aim of the Black Hole Hunter game is to give the player insight into the various techniques used, and challenges faced, in the search for gravitational waves. There are many potential sources of gravitational waves, but the game focused on those emitted during the merger of binaries consisting of black holes and/or neutron stars. These systems produce a characteristic 'chirp' waveform which sweeps upwards in both frequency and amplitude as the stars draw closer to merger.

The game begins by showing the player a graph of the gravitational wave signal from a binary merger, as a TD waveform, and playing a short audio clip of the waveform [1]. The player is then told that he/she must 'detect' this gravitational wave signal. Once the player has listened to the signal he/she is presented with four graphs, and their corresponding audio clips, of simulated data output from a gravitational wave detector, one of which contains the signal. The SNR, which determines the relative amplitudes of the signal and the simulated detector noise, varies depending on the difficulty level. The idea is that the player must work in a similar way to real search algorithms and match the gravitational wave signal to what he/she can see or hear in the noisy data. Interestingly, it is much easier to pick out a signal by listening to the audio clips than by looking at the plots.

Once the player has decided which of the four data streams contains the signal, he/she selects an answer and the game reveals whether it is correct by showing which of the data streams contained the signal and the position of the signal in the noise. If the chosen answer is correct the player will proceed on to the next level where the SNR will be lower, and thus the signal is harder to find. If the wrong answer is selected the player will be able to try again with a different signal at the same SNR. This repeats until the player runs out of 'lives' or reaches the furthest level. The player can choose between *beginner*, *intermediate* or *advanced* at the start of the game, which adjusts the SNR of the first and hardest levels accordingly.

To demonstrate some of the problems faced in real gravitational wave data analysis (and to make the game more fun), the hardest levels also contain 'glitches' in some of the simulated data. The glitches are designed to confuse the player. They are either short sine waves of random frequency with Gaussian envelopes or *other* simulated gravitational waves that are similar to the signal, but shorter in duration. The hardest levels contain simulated data with several glitches of both kinds!

---

[1] Although the signal frequencies are within human hearing range they were in fact shifted to higher pitches because typical laptop speakers and headphones were not deemed adequate at low frequencies.

As well as giving a basic demonstration of the problems data analysts face in searching for gravitational wave sources, the Black Hole Hunter game aims to teach the player more about gravitational physics in general. This is achieved in two ways during the game. Firstly, the home page and the 'Game Over' pages of Black Hole Hunter both have an information bar on the right hand side, which contains links to a variety of pages where the player can find out more about gravitational wave physics, and even actively participate in real gravitational wave research through the *einstein@home* project [85]. Secondly, when the player has given their answer he/she is presented with a prominent 'Did you know?' box. The box contains a snippet of information about gravitational physics and an associated internet link leading to more information. There are nearly one hundred different pieces of information, so it is unlikely that a player will encounter the same 'Did you know?' twice.

In addition to the website the Black Hole Hunter game has been modified to run on a local machine without requiring access to the internet. This version is available in German as well as English.

6.4 Downloadable ringtones

In addition to the game itself, the Black Hole Hunter website also gave players the opportunity to download gravitational wave ringtones. These consisted of short snippets of sound or music in WAV and MP3 format which are suitable for use as a ringtone on a mobile phone. The ringtones themselves were produced by manipulating sound files generated from the expected gravitational wave signals of a variety of sources. The manipulations included significant editing, pitch shifting, layering signals on top of each other, and applying a number of audio effects. These processes were performed using audio editing software such as Cubase[86], LMMS [87] and Audacity [88].

6.5 Response to the Black Hole Hunter game

Black Hole Hunter has been used in exhibitions in the UK and Germany, as a teaching aid in Australia and is forming a major part of a travelling exhibition in the USA [83]. Visitors to these exhibitions typically include school teachers, schoolchildren and their parents.

Following its launch at the 2008 exhibition, Black Hole Hunter was featured in a New Scientist blog [89] and linked from the Einstein@Home web site [85]. With this publicity,

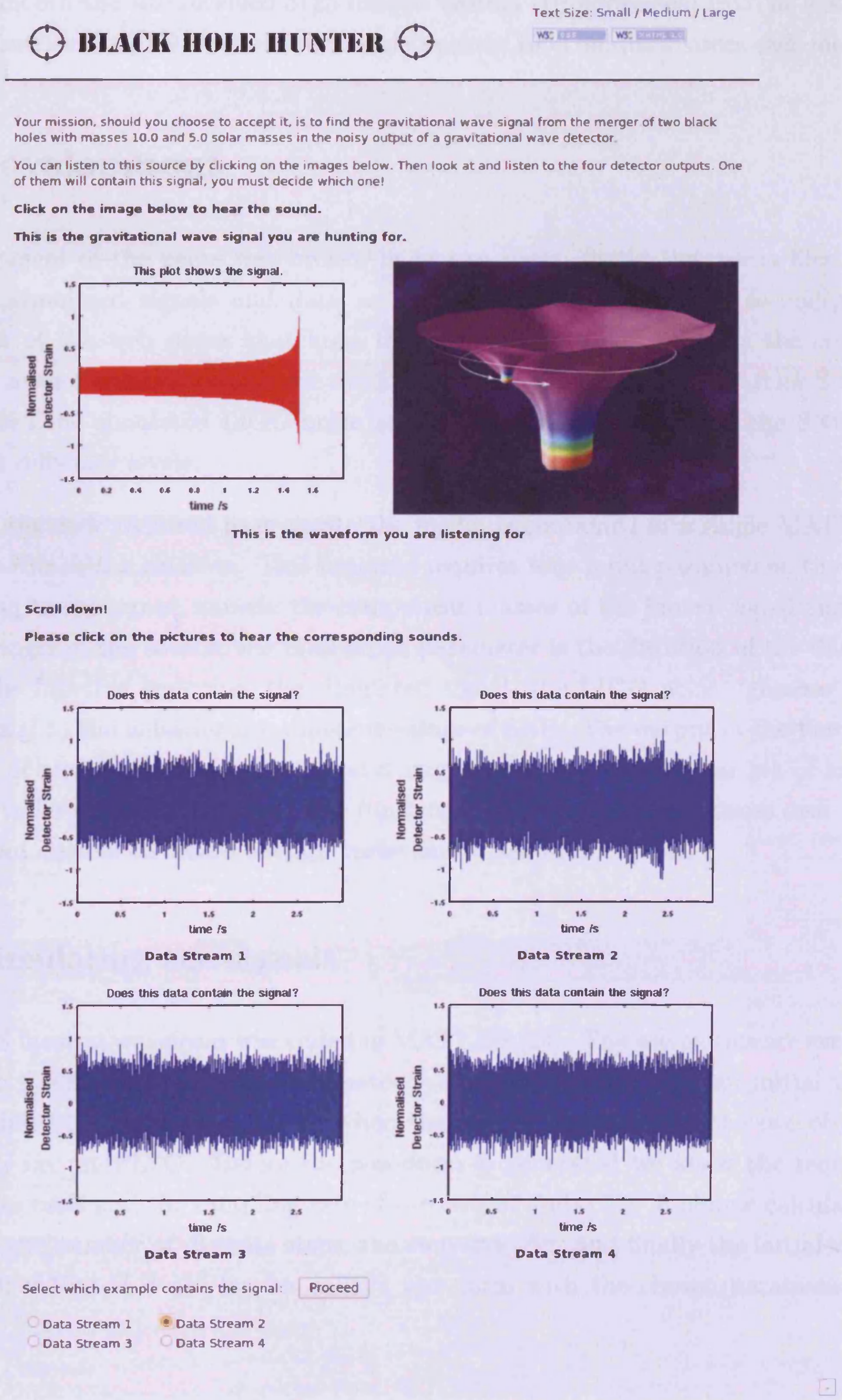

Your mission, should you choose to accept it, is to find the gravitational wave signal from the merger of two black holes with masses 10.0 and 5.0 solar masses in the noisy output of a gravitational wave detector.

You can listen to this source by clicking on the images below. Then look at and listen to the four detector outputs. One of them will contain this signal, you must decide which one!

Click on the image below to hear the sound.

This is the gravitational wave signal you are hunting for.

This is the waveform you are listening for

Scroll down!

Please click on the pictures to hear the corresponding sounds.

Select which example contains the signal:

○ Data Stream 1 ● Data Stream 2
○ Data Stream 3 ○ Data Stream 4

FIGURE 6.1: This is the web page that the player sees when playing Black Hole hunter. The four data sets are plotted, one of which contains the signal. The player listens to the data by clicking on the plots before selecting their answer at the bottom of the page.

in the first month the site received 3123 unique visitors (IP addresses) from at least 66 different countries. In 2009 the website recorded nearly 1000 unique visitors each month.

6.6 Development

The development of the game was broken in to two parts, firstly the media files that contain the simulated signals and data as both audio and images and secondly the development of the web pages that keep the player's score and presents the correct media. The author was responsible for the former, with some help from Patrick Sutton who generated the simulated LIGO noise and Ian Harry who calculated the SNRs of the different difficulty levels.

The core of the code required to generate the media is contained in a single MATLAB function *mp3BlackHoleMusic.m.* This function requires four input parameters, the first three relating to the signal, namely the component masses of the binary signal and the inclination angle of the source; the final input parameter is the duration of the data in seconds. The function generates the simulated signal, the LIGO noise, 'glitches' and adds the signal to the noise for five different values of SNR. The output of the function is a variety of audio and image files, everything needed for a particular set of signal parameters to be used in the game. The function can be run multiple times over with different input choices to create enough variation for the online game.

6.6.1 Simulating the signals

The TT3 PN inspiral waveform was coded in MATLAB [24]. The waveforms are evolved according to a dimensionless time parameter τ, which decreases from an initial value until it reaches 81/16, the value it has when the orbital separation of the two objects is $r = 6M_{\odot}$, i.e. at FLSO. Before the waveform is generated we know the required duration in seconds and the sampling rate of the output audio file. A simple calculation then reveals the number of discrete steps, the step size, $\Delta\tau$, and finally the initial value τ_0. Once all values of τ are known a 2PN waveform with the chosen parameters is generated.

6.6.2 Simulating the noise

The coloured noise is created in the FD, by multiplying a frequency array of Gaussian random amplitudes with the LIGO design PSD. The noise then undergoes an IFT, which means the length of the array and the frequency resolution must be set correctly so that the noise is of the correct length and sample rate in the TD.

6.6.3 Adding the signal to the noise

The first step of the process is to divide the signal and data by their maximum amplitudes plus "epsilon" respectively so that both have a maximum value of just under 1, as the function that produces the audio files from the arrays clips any data with amplitudes greater than 1. The signal and nose are then saved as audio files so that the player can hear the signal before playing and the noise can be used as one of the three data without the signal. Before adding the signal to the noise it is scaled by a chosen factor that sets the difficulty. The duration of the noise is twice that of the signal. Therefore, if the noise is of length T, the last point of the signal is placed at random between $T/2$ and T. The simulated data that contains the signal is again divided by its maximum amplitude plus epsilon. This process is iterated over with different scaling factors for the difficulty levels. At the time of the development, the levels were set 'by ear' with the SNRs estimated retrospectively.

6.6.4 Simulating glitches

There a several types of glitches introduced at random in the harder levels. Firstly, inspiral signals of different parameters are added. The other glitches are sine-Gaussians of a random frequency, in some cases several different glitches are added at the same time. The glitches were not modelled on real causes of data noise, but were engineered to make the game more interesting. The duration of each glitch was set to 1/5 of the noise and normalised to have a maximum amplitude half that of the noise.

Concluding remarks

It is currently an exciting time in gravitational wave research. The LIGO and Virgo detectors have recently collected the most sensitive gravitational wave strain data ever measured; as a result, analyses have produced upper limits on the rates of various astrophysical sources in the nearby Universe. The detectors are currently undergoing further commissioning that will increase their sensitivity, and hence their horizon distance, by a factor of ~ 10. This improved sensitivity equates to a factor of ~ 1000 increase in the volume of the observable Universe. The expected rate of CBCs detectable by advanced LIGO-Virgo networks may be as high as 400 per year or, more realistically, 40 per year [31]. It is not an implausible suggestion that gravitational waves will be directly detected by ground-based interferometric detectors before the centenary of Einstein's completed theory of general relativity, in 2016.

In Chapter 1 and Chapter 2 we learned the nature of gravitational waves and how they may be detected. Gravitational waves are generated by acceleration of the mass quadrupole moment, they are transverse and propagate through vacua at the speed of light. Gravitational waves from CBCs may be modelled using the PN approximation. We saw that the gravitational wave strain upon the Earth from a coalescing binary source at a distance of 100 Mpc would produce a strain of the right amplitude and frequency to be detectable by ground-based interferometric detectors such as LIGO.

In Chapter 3 we covered the derivation of the matched filter and saw how it was used in a search pipeline on a subset of LIGO's S5 data, that placed the following upper limits on the rates with 90% confidence: BNS - 1.4×10^{-2} $\mathrm{yr}^{-1}\mathrm{L}_{10}^{-1}$; BBH - 7.3×10^{-4} $\mathrm{yr}^{-1}\mathrm{L}_{10}^{-1}$ and NSBH - 3.3×10^{-3} $\mathrm{yr}^{-1}\mathrm{L}_{10}^{-1}$. Although these upper limits are 1-2 orders of magnitude above the optimistic predicted rates they are a significantly lower than those obtained from the S51YR search alone.

In Chapter 4 we set out the motivations behind using higher order waveforms in gravitational wave data analysis and then developed a filtering algorithm that used templates of

0.5PN in amplitude. The algorithm required significant development with key changes in normalisation and maximisation in comparison to the RWF algorithm. A matrix was used to transform the templates from their original basis to an orthonormal basis before computing the SNR. A constraint was set on the SNR of the relative harmonics by transforming it back to the original basis and comparing with the expected maximum values. The final results were promising with improvements in both the detection (SNR value) and the parameter estimation observed, which matched the original motivations. Furthermore, by studying the SNR time-series we observed that the constraint appears to be a very effective signal-based veto in terms of eliminating noise, which could lead to a reduced FAR. There is great potential for the FWF filtering algorithm, even at 0.5PN, and perhaps a further developed version will play a part in the analysis pipeline of the next generation detectors.

In Chapter 5 we examined a new method of windowing that tapers the start and/or end of a waveform using an algorithm that finds the near-optimal place to apply the taper, ensuring that the transitions are smooth. The new method resulted in a better estimation for the SNR, a more 'realistic' representation of the signal in the FD and reduced trigger rates when tested with a LIGO high mass pipeline in LIGO's S4 data. Furthermore, the method did not significantly affect the number of detected injections, indicating that detection efficiency would be improved with use of the window due to the reduction in background.

Finally, we ended with a description of Black Hole Hunter, an exciting outreach project that aims to teach the public about gravitational waves and the efforts to detect them.

Appendix A

Introduction

A.1 The energy-momentum tensor

The energy-momentum tensor contains information on the matter and energy that causes the curvature of spacetime. Its components represent the following:

- T^{00} is the relativistic mass density;
- T^{0i} is the flux of momentum in the i direction;
- T^{ij} is the rate of flow of the i component of momentum in the j direction. These components are often referred to as the *stress* components for $i \neq j$ and the *pressure* components for $i = j$.

N.B.: $T^{\mu\nu} = T^{\nu\mu}$.

A.2 The amplitude matrix $A_{\mu\nu}$

The Lorentz gauge condition (1.17) is only satisfied if

$$A_{\mu\nu}k^{\nu} = 0\,, \tag{A.1}$$

which implies that the amplitude matrix is orthogonal to k^{ν}.

Appendix B

Gravitational waves radiated from binary systems

B.1 The Lambda tensor

The Lambda tensor, $\Lambda_{ij,kl}$, upon contraction with any symmetric tensor, B_{ij}, yields the transverse and traceless part, i.e.,

$$B_{ij}^{TT} = \Lambda_{ij,kl} B_{kl} \,. \tag{B.1}$$

The Lambda tensor is defined as

$$\Lambda_{ij,kl}(\hat{\mathbf{n}}) = \delta_{ik}\delta_{jl} - \frac{1}{2}\delta_{ij}\delta_{kl} - n_j n_l \delta_{ik} - n_i n_k \delta_{jl} + \frac{1}{2} n_k n_l \delta_{ij} + \frac{1}{2} n_i n_j \delta_{kl} + \frac{1}{2} n_i n_j n_k n_l \,. \tag{B.2}$$

B.2 Centre-of-mass, single body representation

For a point particle, following a trajectory $x_0(t)$ in flat spacetime the energy momentum tensor is

$$T^{\mu\nu}(t, \mathbf{x}) = \frac{p^\mu p^\nu}{\gamma m} \delta^{(3)} \left(\mathbf{x} - \mathbf{x}_0(t) \right) , \tag{B.3}$$

where

$$p^\mu = \gamma m (dx_0^\mu / dt) \,, \tag{B.4}$$

is the four-momentum and

$$\gamma = \left(1 - v^2\right)^{-\frac{1}{2}}, \tag{B.5}$$

where

$$v^2 := \frac{dx^i}{dt}\frac{dx_i}{dt}. \tag{B.6}$$

B.3 Moments

B.3.1 Taylor expansion of the energy-momentum tensor

In Section 2.1.1 the polarisations (2.5) are written as a Taylor expansion of the energy-momentum tensor. Firstly, (2.4) is written in terms of the Fourier transform (FT) of $T_{\mu\nu}$, which only consists of frequencies $\omega \leq \omega_s$ where $\omega_s a \ll 1$. Under these conditions it is clear that the exponent in the FT can be expanded, which is equivalent to the Taylor expansion in the time domain (TD):

$$T_{kl}\left(t - D + \mathbf{x}' \cdot \hat{\mathbf{n}}, \mathbf{x}'\right) = T_{kl}\left(t - D, \mathbf{x}'\right) + \mathbf{x}'_i \mathbf{n}^i \delta T_{kl} + \frac{1}{2}\mathbf{x}'_i \mathbf{x}'_j \mathbf{n}^i \mathbf{n}^j \delta^2 T_{kl} + \dots. \tag{B.7}$$

B.3.2 Moments of the source

In Section 2.1.1 the expansion of the energy-momentum tensor is expressed as the moments, S^{ij}, of the the stress components of T^{ij}, which have the following definitions:

$$S^{ij}(t) = \int d^3x T^{ij}(t, \mathbf{x}), \tag{B.8a}$$

$$S^{ij,k}(t) = \int d^3x T^{ij}(t, \mathbf{x}) x^k, \tag{B.8b}$$

$$S^{ij,kl}(t) = \int d^3x T^{ij}(t, \mathbf{x}) x^k x^l. \tag{B.8c}$$

We also introduced the moments of the energy density, which are defined as

$$M = \int d^3x T^{00}(t, \mathbf{x}), \tag{B.9a}$$

$$M^i = \int d^3x T^{00}(t, \mathbf{x}) x^i, \tag{B.9b}$$

$$M^{ij} = \int d^3x T^{00}(t, \mathbf{x}) x^i x^j, \tag{B.9c}$$

$$M^{ijk} = \int d^3x T^{00}(t, \mathbf{x}) x^i x^j x^k. \tag{B.9d}$$

Similarly the moments of the momentum density are defined as

$$P^i = \int d^3x T^{0i}(t, \mathrm{x}) \,, \tag{B.10a}$$

$$P^{i,j} = \int d^3x T^{0i}(t, \mathrm{x}) x^j \,, \tag{B.10b}$$

$$P^{i,jk} = \int\int d^3x T^{0i}(t, \mathrm{x}) x^j x^k \,. \tag{B.10c}$$

$$\int$$

B.3.3 Identities

In linearised theory there are a number of identities that exist between the moments. These are obtained by defining a volume V that is larger than the source, such that $T^{\mu\nu} = 0$ outside V, and applying the conservation law $\partial_\mu T^{\mu\nu} = 0$. To first order the identities are

$$\dot{M} = 0 \,, \tag{B.11a}$$

$$\dot{M}^i = P^i \,, \tag{B.11b}$$

$$\dot{M}^{ij} = P^{i,j} + P^{j,i} \,, \tag{B.11c}$$

$$\dot{M}^{ijk} = P^{i,jk} + P^{j,ki} + P^{k,ij} \,, \tag{B.11d}$$

and

$$\dot{P}^i = 0 \,, \tag{B.12a}$$

$$\dot{P}^{i,j} = S^{ij} \,, \tag{B.12b}$$

$$\dot{P}^{i,jk} = S^{ij,k} + S^{ik,j} \,. \tag{B.12c}$$

It is from these identities that we find (2.6). N.B.: (B.11a) and (B.12a) are the conservation of mass and momentum respectively, whilst it can also be shown that $S^{ij} - S^{ji} = 0$, which corresponds to the conservation of angular momentum.

B.4 The Taylor-T3 phase approximant

The TT3 approximant up to 2PN in order [55]:

$$\begin{aligned}\varphi_{\mathrm{TT3}}(t) = \varphi_0 - \frac{1}{\eta\theta^5}\Bigg[1 &+ \left(\frac{3715}{8064} + \frac{55}{96}\eta\right)\theta^2 - \frac{3\pi}{4}\theta^3 \\ &+ \left(\frac{9275495}{14450688} + \frac{284875}{258048}\eta + \frac{1855}{2048}\eta^2\right)\theta^4 \\ &+ \left(\frac{38645}{21504} - \frac{65}{256}\eta\right)\ln\left(\frac{\theta}{\theta_{LSO}}\right)\pi\theta^5\Bigg],\end{aligned} \tag{B.13}$$

where

$$\theta = \left[\frac{\eta(t_0 - t)}{5M}\right]^{-\frac{1}{8}}, \tag{B.14}$$

φ_0 is a constant and θ_{LSO} is the value of θ at the time of ISCO.

B.5 The inspiral gravitational wave polarisations up to 2PN

The gravitational wave polarisations from inspiralling compact binaries up to 2PN are [26]:

$$H_+^{(0)} = \left(1 + \cos^2 i\right)\cos 2\varphi\,, \tag{B.15a}$$

$$H_\times^{(0)} = 2\cos i \sin 2\varphi\,, \tag{B.15b}$$

$$H_+^{(0.5)} = -\Delta \sin i\left[\left(\frac{5}{8} + \frac{1}{8}\cos^2 i\right)\cos\varphi - \left(\frac{9}{8} + \frac{9}{8}\cos^2 i\right)\cos(3\varphi)\right], \tag{B.16a}$$

$$H_\times^{(0.5)} = -\Delta \sin i \cos i\left[-\frac{3}{4}\sin\varphi + \frac{9}{4}\sin(3\varphi)\right], \tag{B.16b}$$

Continued on following page.

$$
\begin{aligned}
H_{+}^{(1)} = & -\cos 2\varphi\left[\frac{19}{6}+\frac{3}{2}\cos^2 i-\frac{1}{3}\cos^4 i+\eta\left(-\frac{19}{6}+\frac{11}{6}\cos^2 i+\cos^4 i\right)\right] \\
& +\cos 4\varphi\left[\frac{4}{3}\sin^2 i\left(1+cos^2 i\right)(1-3\eta)\right],
\end{aligned}
\qquad \text{(B.17a)}
$$

$$
\begin{aligned}
H_{\times}^{(1)} = & -\cos i\sin 2\varphi\left[\frac{17}{3}-\frac{4}{3}\cos^2 i+\eta\left(-\frac{13}{3}+4\cos^2 i\right)\right] \\
& -\cos i\sin^2 i\sin 4\varphi\left[-\frac{8}{3}(1-3\eta)\right],
\end{aligned}
\qquad \text{(B.17b)}
$$

$$
\begin{aligned}
H_{+}^{(1.5)} = & -\sin i\Delta\cos\varphi\left[\frac{19}{64}+\frac{5}{16}\cos^2 i-\frac{1}{192}\cos^4 i\right. \\
& \left.+\eta\left(-\frac{49}{96}+\frac{1}{8}\cos^2 i+\frac{1}{96}\cos^4 i\right)\right] \\
& -\cos 2\varphi\left[-2\pi\left(1+\cos^2 i\right)\right] \\
& -\sin i\Delta\cos 3\varphi\left[-\frac{657}{128}-\frac{45}{16}\cos^2 i+\frac{81}{128}\cos^4 i\right. \\
& \left.+\eta\left(\frac{225}{64}-\frac{9}{8}\cos^2 i-\frac{81}{64}\cos^4 i\right)\right] \\
& -\sin i\Delta\cos 5\varphi\left[\frac{625}{384}\sin^2 i\left(1+\cos^2 i\right)(1-2\eta)\right],
\end{aligned}
\qquad \text{(B.18a)}
$$

$$
\begin{aligned}
H_{\times}^{(1.5)} = & -\sin i\cos i\Delta\sin\varphi\left[\frac{21}{32}-\frac{5}{96}\cos^2 i+\eta\left(-\frac{23}{48}+\frac{5}{48}\cos^2 i\right)\right] \\
& +4\pi\cos i\sin 2\varphi \\
& -\sin i\cos i\Delta\sin 3\varphi\left[-\frac{603}{64}+\frac{135}{64}\cos^2 i+\eta\left(\frac{171}{32}-\frac{135}{32}\cos^2 i\right)\right] \\
& -\sin i\cos i\Delta\sin 5\varphi\left[\frac{625}{192}(1-2\eta)\sin^2 i\right],
\end{aligned}
\qquad \text{(B.18b)}
$$

$$
\begin{aligned}
H_+^{(2)} = & -\pi \sin i \cos\varphi \left[-\frac{5}{8} - \frac{1}{8}\cos^2 i \right] \\
& - \cos 2\varphi \left[\frac{11}{60} + \frac{33}{10}\cos^2 i + \frac{29}{24}\cos^4 i - \frac{1}{24}\cos^6 i \right. \\
& + \eta \left(\frac{353}{36} - 3\cos^2 i - \frac{251}{72}\cos^4 i + \frac{5}{24}\cos^6 i \right) \\
& \left. + \eta^2 \left(-\frac{49}{12} + \frac{9}{2}\cos^2 i - \frac{7}{24}\cos^4 i - \frac{5}{24}\cos^6 i \right) \right] \\
& - \pi \sin i \Delta \cos 3\varphi \left[\frac{27}{8}\left(1 + \cos^2 i\right) \right] \\
& - \frac{2}{15}\sin^2 i \cos 4\varphi \left[59 + 35\cos^2 i - 8\cos^4 i - \frac{5}{3}\eta\left(131 + 59\cos^2 i - 24\cos^4 i\right) \right. \\
& \left. + 5\eta^2\left(21 - 3\cos^2 i - 8\cos^4 i\right) \right] \\
& - \cos 6\varphi \left[-\frac{81}{40}\sin^4 i\left(1 + \cos^2 i\right)\left(1 - 5\eta + 5\eta^2\right) \right] \\
& - \sin i \Delta \sin\varphi \left[\frac{11}{40} + \frac{5\ln 2}{4} + \cos^2 i \left(\frac{7}{40} + \frac{\ln 2}{4} \right) \right] \\
& - \sin i \Delta \sin 3\varphi \left[\left(-\frac{189}{40} + \frac{27}{4}\ln\left(\frac{3}{2}\right) \right)\left(1 + \cos^2 i\right) \right]
\end{aligned}
\tag{B.19a}
$$

$$
\begin{aligned}
H_\times^{(2)} = & - \sin i \cos i \Delta \cos\varphi \left[-\frac{9}{20} - \frac{3}{2}\ln 2 \right] \\
& - \sin i \cos i \Delta \cos 3\varphi \left[\frac{189}{20} - \frac{27}{2}\ln\left(\frac{3}{2}\right) \right] \\
& + \sin i \cos i \Delta \frac{3\pi}{4}\sin\varphi \\
& - \cos i \sin 2\varphi \left[\frac{17}{15} + \frac{113}{30}\cos^2 i - \frac{1}{4}\cos^4 i \right. \\
& + \eta\left(\frac{143}{9} - \frac{245}{18}\cos^2 i + \frac{5}{4}\cos^4 i \right) \\
& \left. + \eta^2\left(-\frac{14}{3} + \frac{35}{6}\cos^2 i - \frac{5}{4}\cos^4 i \right) \right] \\
& - \sin i \cos i \Delta \sin 3\varphi \left[\frac{27\pi}{4} \right] \\
& - \frac{4}{15}\cos i \sin^2 i \sin 4\varphi \left[55 - 12\cos^2 i - \frac{5}{3}\eta\left(119 - 36\cos^2 i\right) + 5\eta^2\left(17 - 12\cos^2 i\right) \right] \\
& - \cos i \sin 6\varphi \left[-\frac{81}{20}\sin^4 i\left(1 - 5\eta + 5\eta^2\right) \right] .
\end{aligned}
\tag{B.19b}
$$

(B.19c)

Appendix C

Higher order waveforms in data analysis

C.1 Maximisation proof

Lemma: In (4.36) maximising Λ over α_i and λ yields the maximum of ρ with the constraint

$$\sum_{i=1}^{6} \alpha_i'^2 = 1\,. \tag{C.1}$$

Proof: Suppose that another quantity $\gamma_{i=1,\ldots,6}$ exists such that

$$\sum_{i=1}^{6} \gamma_i = 1\,, \tag{C.2}$$

and

$$\rho[\gamma_i] > \rho[\alpha_i']\,. \tag{C.3}$$

However, (C.2) means that

$$\rho[\gamma_i] = \Lambda[\gamma_i]\,. \tag{C.4}$$

Yet α_i' maximise Λ which would give

$$\Lambda[\gamma_i] \leq \Lambda[\alpha_i'] = \rho[\alpha_i']\,, \tag{C.5}$$

but that contradicts (C.3).

C.2 The log-normal distribution

The log-normal distribution, $f(x;\mu,\sigma)$, is the probability distribution of a random variable whose logarithm is normally distributed:

$$f(x;\mu,\sigma) = \frac{1}{x\sigma\sqrt{2\pi}} e^{-\frac{(\ln x-\mu)^2}{2\sigma^2}}, \quad x > 0\,, \tag{C.6}$$

where μ is the mean and σ is the standard deviation of the distribution, respectively.

C.3 Maximum correlation between two templates

In [64] it is shown how to find the minimum and maximum correlation between two *two-phase* templates, for the case of any time lag between the templates arrival time. We are interested in the maximum correlation. Given two templates, or two harmonics of a 0.5PN template, a and b, the process is as follows:

1. Compute the following:

$$A = \langle a_+, b_+\rangle^2 + \langle a_+, b_\times\rangle^2\,, \tag{C.7}$$

$$B = \langle a_\times, b_+\rangle^2 + \langle a_\times, b_\times\rangle^2\,, \tag{C.8}$$

$$C = \langle a_+, b_+\rangle \langle a_\times, b_+\rangle + \langle a_+, b_\times\rangle \langle a_\times, b_\times\rangle\,. \tag{C.9}$$

(C.10)

2. The maximum overlap, p, between a and b is then given by

$$p = \left[\frac{A+B}{2} + \left[\left(\frac{A-B}{2}\right)^2 + C^2\right]^{\frac{1}{2}}\right]^2 \tag{C.11}$$

3. Compute p over all values of time and record the maximum value.

Appendix D

Miscellany

D.1 ACTD logo

No self-respecting student can dare to develop new code without designing an appropriate logo. The 0.5PN filtering algorithms are written in codes named with the acronym *Amplitude Corrected Time-Domain (ACTD)*. Thus there was only one logo suitable... cf. Figure D.1.

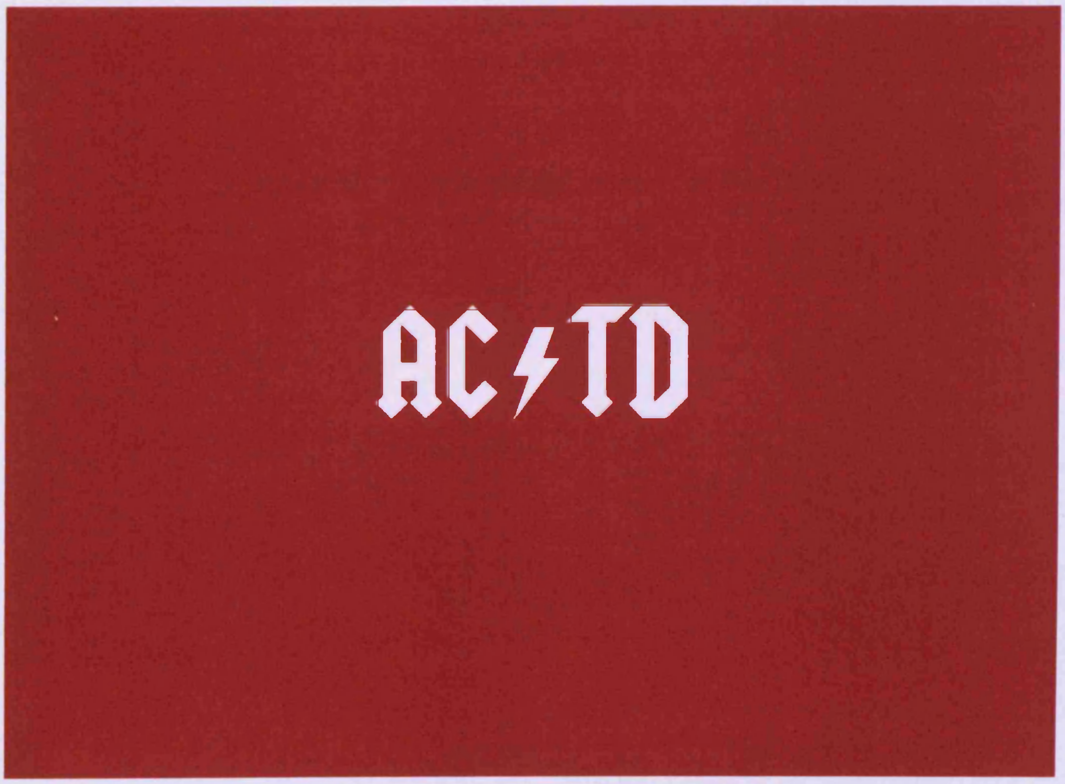

FIGURE D.1: The only appropriate logo for the ACTD codes.

D.2 SVN commit history

The author's progress in writing this thesis is shown in Figure D.2. N.B.: at the outset the author committed files individually before realising that several file changes could be covered in one commit. Therefore the actual increase in work rate is slightly under exaggerated.

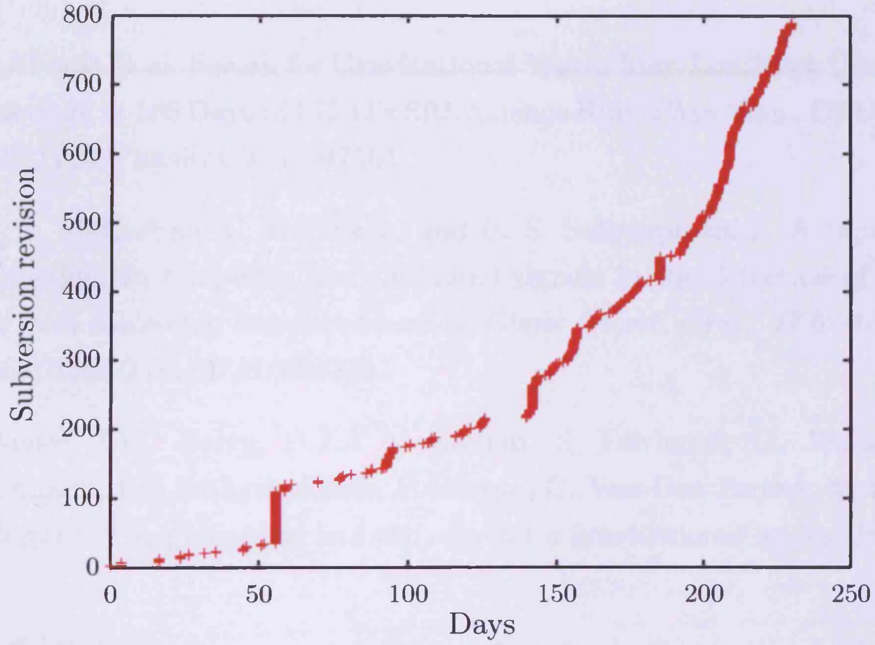

FIGURE D.2: SVN commit history of this thesis.

Bibliography

[1] B. P. Abbott et al. Search for Gravitational Waves from Low Mass Compact Binary Coalescence in 186 Days of LIGO's fifth Science Run. *Phys. Rev.*, D80:047101, 2009. doi: 10.1103/PhysRevD.80.047101.

[2] D. J. A. McKechan, C. Robinson, and B. S. Sathyaprakash. A tapering window for time-domain templates and simulated signals in the detection of gravitational waves from coalescing compact binaries. *Class. Quant. Grav.*, 27:084020, 2010. doi: 10.1088/0264-9381/27/8/084020.

[3] G. Davies, I.W. Harry, D.J.A McKechan, S. Fairhurst, G. Jones, D Pathak, C. Robinson, B.S Sathyaprakash, P. Sutton, C. Van Den Broeck, and J Yu. Black hole hunter: The game that lets you search for gravitational waves. *In preparation*, 2010.

[4] Peter R. Saulson. *Fundamentals of Interferometric Gravitational Wave Detectors.* World Scientific, Singapore, 1994.

[5] R. A. Hulse. Nobel lecture: The discovery of the binary pulsar. 66:699, 1994.

[6] V. Fafone. Developments in resonant-mass detectors. *Class. Quant. Grav.*, 23: S223–S229, 2006. doi: 10.1088/0264-9381/23/8/S28.

[7] A. Lazzarini and R. Weiss. LIGO science requirements document (srd). *Technical document LIGO-E950018-02-E*, 1996.

[8] Daniel A. Shaddock. An overview of the Laser Interferometer Space Antenna. *Publ. Astron. Soc. Austral.*, 26:128–132, 2009.

[9] Vincent Corbin and Neil J. Cornish. Detecting the cosmic gravitational wave background with the big bang observer. *Class. Quant. Grav.*, 23:2435–2446, 2006. doi: 10.1088/0264-9381/23/7/014.

[10] G. Hobbs et al. The international pulsar timing array project: using pulsars as a gravitational wave detector. 2009.

[11] J. P. W. Verbiest et al. Status Update of the Parkes Pulsar Timing Array. 2009.

[12] T. Uchiyama et al. Present status of large-scale cryogenic gravitational wave telescope. *Class. Quant. Grav.*, 21:S1161–S1172, 2004.

[13] Joshua R Smith. The path to the enhanced and advanced LIGO gravitational-wave detectors. *Class. Quant. Grav.*, 26:114013, 2009. doi: 10.1088/0264-9381/26/11/114013.

[14] Xavier Siemens, Bruce Allen, Jolien Creighton, Martin Hewitson, and Michael Landry. Making h(t) for LIGO. *Class. Quant. Grav.*, 21:S1723–S1736, 2004. doi: 10.1088/0264-9381/21/20/015.

[15] M Maggiore. *Gravitational Waves Volume 1: Theory and Experiments.* Oxford, Great Clarendon Street, OX2 6DP, 2008.

[16] G Efstathiou M Maggiore and AN Lasenby. *General Relativity An Introduction for Physicists.* Cambridge, The Edinburgh Building, CB2 8RU, 2006.

[17] E. W. Leaver. An Analytic representation for the quasi normal modes of Kerr black holes. *Proc. Roy. Soc. Lond.*, A402:285–298, 1985.

[18] Steven R. Brandt and Edward Seidel. The Evolution of distorted rotating black holes. 1: Methods and tests. *Phys. Rev.*, D52:856–869, 1995. doi: 10.1103/PhysRevD.52.856.

[19] Alessandra Buonanno et al. Toward faithful templates for non-spinning binary black holes using the effective-one-body approach. *Phys. Rev. D*, 76:104049, 2007. doi: 10.1103/PhysRevD.76.104049.

[20] Thibault Damour and Alessandro Nagar. Comparing Effective-One-Body gravitational waveforms to accurate numerical data. *Phys. Rev. D*, 77:024043, 2008. doi: 10.1103/PhysRevD.77.024043.

[21] Curt Cutler et al. The last three minutes: issues in gravitational wave measurements of coalescing compact binaries. *Phys. Rev. Lett.*, 70:2984–2987, 1993.

[22] C Cutler and E Flanagan. Gravitational waves from mergin compact binaries: How accurately can one extract the binary's parameters from the inspiral waveform? *Phys. Rev. D*, 49:2658, 1994.

[23] Luc Blanchet, Guillaume Faye, Bala R. Iyer, and Benoit Joguet. Gravitational-wave inspiral of compact binary systems to 7/2 post-Newtonian order. *Phys. Rev. D*, 65:061501(R), 2002.

[24] Luc Blanchet, Thibault Damour, Gilles Esposito-Farèse, and Bala R. Iyer. Gravitational radiation from inspiralling compact binaries completed at the third post-Newtonian order. *Phys. Rev. Lett.*, 93:091101, 2004.

[25] Thibault Damour, Bala R. Iyer, and B. S. Sathyaprakash. A comparison of search templates for gravitational waves from binary inspiral. *Phys. Rev. D*, 63:044023, 2001.

[26] Luc Blanchet, Guillaume Faye, Bala R. Iyer, and Siddhartha Sinha. The third post-Newtonian gravitational wave polarisations and associated spherical harmonic modes for inspiralling compact binaries in quasi-circular orbits. *Class. Quant. Grav.*, 25:165003, 2008.

[27] The LIGO Scientific Collaboration. Tuning matched filter searches for compact binary coalescence. Technical Report LIGO-T070109-01, 2007. URL `http://www.ligo.caltech.edu/docs/T/T070109-01.pdf`.

[28] B. Abbott et al. Search for gravitational waves from binary inspirals in S3 and S4 LIGO data. *Phys. Rev. D*, 77:062002, 2008.

[29] B. Abbott et al. Search for gravitational waves from low mass binary coalescences in the first year of ligo's s5 data. *Physical Review D*, 79(12):122001, 2009. doi: 10.1103/PhysRevD.79.122001. URL `http://link.aps.org/abstract/PRD/v79/e122001`.

[30] Bruce Allen, Warren G. Anderson, Patrick R. Brady, Duncan A. Brown, and Jolien D. E. Creighton. Findchirp: an algorithm for detection of gravitational waves from inspiraling compact binaries, 2005. URL `http://www.citebase.org/abstract?id=oai:arXiv.org:gr-qc/0509116`.

[31] J. Abadie et al. Predictions for the Rates of Compact Binary Coalescences Observable by Ground-based Gravitational-wave Detectors. 2010.

[32] F. Acernese et al. Status of Virgo. *Classical and Quantum Gravity*, 25(11):114045–+, June 2008. doi: 10.1088/0264-9381/25/11/114045.

[33] V. Kalogera, R. Narayan, D. N. Spergel, and J. H. Taylor. The coalescence rate of double neutron star systems. 556:340, 2001.

[34] L A Wainstein and V D Zubakov. *Extraction of signals from noise.* Prentice-Hall, Englewood Cliffs, NJ, 1962.

[35] B.S. Sathyaprakash and S.V. Dhurandhar. Choice of filters for the detection of gravitational waves from coalescing binaries. *Phys. Rev. D*, 44:3819–3834, 1991. doi: 10.1103/PhysRevD.44.3819.

[36] Benjamin J. Owen. Search templates for gravitational waves from inspiraling binaries: Choice of template spacing. *Phys. Rev. D*, 53:6749–6761, 1996.

[37] Thomas Cokelaer. Gravitational wave from inspiralling compact binaries: hexagonal template placement and its efficiency in detecting physical signals. *Phys. Rev. D*, 76:102004, 2007.

[38] C. A. K. Robinson, B. S. Sathyaprakash, and Anand S. Sengupta. Geometric algorithm for efficient coincident detection of gravitational waves. *Physical Review D*, 78(6):062002, 2008. doi: 10.1103/PhysRevD.78.062002.

[39] Bruce Allen. A χ^2 time-frequency discriminator for gravitational wave detection. *Phys. Rev. D*, 71:062001, 2005.

[40] Patrick R. Brady and Stephen Fairhurst. Interpreting the results of searches for gravitational waves from coalescing binaries. *Class. Quant. Grav.*, 25(10):1050002, 2008. doi: 10.1088/0264-9381/25/10/105002.

[41] P. R. Brady, J. D. E. Creighton, and A. G. Wiseman. Upper limits on gravitational-wave signals based on loudest events. *Class. Quant. Grav.*, 21:S1775–S1781, 2004.

[42] Rahul Biswas, Patrick R. Brady, Jolien D. E. Creighton, and Stephen Fairhurst. The Loudest Event Statistic: General Formulation, Properties and Applications. *Class. Quant. Grav.*, 26:175009, 2009. doi: 10.1088/0264-9381/26/17/175009.

[43] Ravi Kumar Kopparapu, Chad Hanna, Vicky Kalogera, Richard O'Shaughnessy, Gabriela Gonzalez, Patrick R. Brady, and Stephen Fairhurst. Host Galaxies Catalog Used in LIGO Searches for Compact Binary Coalescence Events. *Astrophys. J.*, 675 (2):1459–1467, 2008. doi: 10.1086/527348.

[44] LSC and Virgo. Search for Gravitational Waves from Compact Binary Coalescence in LIGO and Virgo Data from S5 and VSR1. 2010.

[45] R. N. Manchester, G. B. Hobbs, A. Teoh, and M. Hobbs. The australia telescope national facility pulsar catalogue. *Astronom. J.*, 129(4):1993–2006, 2005. doi: 10.1086/428488.

[46] Theocharis A. Apostolatos, Curt Cutler, Gerald J. Sussman, and Kip S. Thorne. Spin-induced orbital precession and its modulation of the gravitational waveforms from merging binaries. *Phys. Rev. D*, 49:6274, 1994.

[47] LSC Algorithm Library software packages LAL, LALWRAPPER, and LALAPPS. URL `http://www.lsc-group.phys.uwm.edu/lal`.

[48] Todd Tannenbaum, Derek Wright, Karen Miller, and Miron Livny. Condor – a distributed job scheduler. In Thomas Sterling, editor, *Beowulf Cluster Computing with Linux*. MIT Press, October 2001.

[49] Sathyaprakash B. Robinson C, Regimbau T. How ideal is ligo data? *In preparation*, 2010.

[50] B. Abbott et al. Search of S3 LIGO data for gravitational wave signals from spinning black hole and neutron star binary inspirals. *Phys. Rev. D*, 78:042002, 2008.

[51] Alessandra Buonanno, Yanbei Chen, Yi Pan, Hideyuki Tagoshi, and Michele Vallisneri. Detecting gravitational waves from precessing binaries of spinning compact objects. ii. search implementation for low-mass binaries. *Phys. Rev. D*, 72:084027, 2005.

[52] Alessandra Buonanno, Yan-bei Chen, Yi Pan, and Michele Vallisneri. A quasi-physical family of gravity-wave templates for precessing binaries of spinning compact objects: Ii. application to double-spin precessing binaries. *Phys. Rev. D*, 70: 104003, 2004. Erratum-ibid. 74 (2006) 029902(E).

[53] Yi Pan, Alessandra Buonanno, Yan-bei Chen, and Michele Vallisneri. A physical template family for gravitational waves from precessing binaries of spinning compact objects: Application to single-spin binaries. *Phys. Rev. D*, 69:104017, 2004. Erratum-ibid. 74 (2006) 029905(E).

[54] Chris Van Den Broeck. Binary black hole detection rates in inspiral gravitational wave searches. *Class. Quant. Grav.*, 23:L51–L58, 2006.

[55] Alessandra Buonanno, Bala Iyer, Evan Ochsner, Yi Pan, and B. S. Sathyaprakash. Comparison of post-Newtonian templates for compact binary inspiral signals in gravitational-wave detectors. *Phys. Rev.*, D80:084043, 2009. doi: 10.1103/PhysRevD.80.084043.

[56] Benjamin J. Owen and B. S. Sathyaprakash. Matched filtering of gravitational waves from inspiraling compact binaries: Computational cost and template placement. *Phys. Rev. D*, 60:022002, 1999.

[57] Alicia M. Sintes and Alberto Vecchio. Detection of gravitational waves from inspiraling compact binaries using non-restricted post-Newtonian approximations. 1999.

[58] Alicia M. Sintes and Alberto Vecchio. LISA observations of massive black holes binaries using post-Newtonian wave forms. 1999.

[59] Thomas A. Moore and Ronald W. Hellings. The angular resolution of space-based gravitational wave detectors. *Phys. Rev.*, D65:062001, 2002. doi: 10.1103/PhysRevD.65.062001.

[60] Ronald W. Hellings and Thomas A. Moore. The information content of gravitational wave harmonics in compact binary inspiral. *Class. Quant. Grav.*, 20: S181–S192, 2003.

[61] Chris Van Den Broeck and Anand S. Sengupta. Binary black hole spectroscopy. *Class. Quant. Grav.*, 24:1089–1114, 2007. doi: 10.1088/0264-9381/24/5/005.

[62] L.S. Finn and D.F. Chernoff. *Phys. Rev. D*, 47:2198–2219, 1993.

[63] URL `http://www.gnu.org/software/gsl/`.

[64] Thibault Damour, Bala R. Iyer, and B. S. Sathyaprakash. Improved filters for detecting gravitational waves from inspiralling compact binaries. *Phys. Rev. D*, 57: 885, 1998.

[65] S. Klimenko and G. Mitselmakher. A wavelet method for detection of gravitational wave bursts. *Class. Quantum Grav.*, 21:S1819–S1830, 2004.

[66] S. Klimenko, I. Yakushin, M. Rakhmanov, and G. Mitselmakher. Performance of the waveburst algorithm on ligo data. *Class. Quantum Grav.*, 21:S1685–S1694, 2004.

[67] Shourov Chatterji et al. Coherent network analysis technique for discriminating gravitational-wave bursts from instrumental noise. *Phys. Rev.*, D74:082005, 2006. doi: 10.1103/PhysRevD.74.082005.

[68] C. R. Hanna. Reducing gravitational wave false alarms using signals at the anti-symmetric port in LIGO detectors. *Class. Quant. Grav.*, 23:17–22, 2006.

[69] B. Abbott et al. Analysis of LIGO data for gravitational waves from binary neutron stars. *Phys. Rev. D*, 69:122001, 2004.

[70] K. A. Arnaud, S. Babak, J. G. Baker, M. J. Benacquista, N. J. Cornish, C. Cutler, L. S. Finn, S. L. Larson, T. Littenberg, E. K. Porter, M. Vallisneri, A. Vecchio, J.-Y. Vinet, and T. M. L. Data Challenge Task Force. An overview of the second round of the Mock LISA Data Challenges. *Classical and Quantum Gravity*, 24: 551–+, October 2007. doi: 10.1088/0264-9381/24/19/S18.

[71] National Instruments. Windowing: Optimizing ffts using window functions, 2009. URL `http://zone.ni.com/devzone/cda/tut/p/id/4844`.

[72] Thibault Damour, Bala R. Iyer, and B. S. Sathyaprakash. Frequency-domain P-approximant filters for time-truncated inspiral gravitational wave signals from compact binaries. *Phys. Rev.*, D62:084036, 2000. doi: 10.1103/PhysRevD.62.084036.

[73] F. J. Harris. On the use of windows for harmonic analysis with the discrete fourier transform. *Proceedings of the IEEE*, 66:51–83, January 1978.

[74] C. Röver, R. Meyer, and N. Christensen. Coherent bayesian inference on compact binary inspirals using a network of interferometric gravitational wave detectors. *Phys. Rev. D*, 75(6):062004, March 2007. doi: 10.1103/PhysRevD.75.062004.

[75] B S Sathyaprakash and S V Dhurandhar. *Phys. Rev D*, 44:3819, 1991.

[76] Stas Babak, Balasubramanian, David Churches, Thomas Cokelaer, and B.S. Sathyaprakash. A template bank to search for gravitational waves from inspiralling compact binaries i: physical models. *Class. Quant. Grav.*, 23:5477–5504, 2006.

[77] Alessandra Buonanno and Thibault Damour. Effective one-body approach to general relativistic two-body dynamics. *Phys. Rev. D*, 59:084006, 1999.

[78] Alessandra Buonanno and Thibault Damour. Transition from inspiral to plunge in binary black hole coalescences. *Phys. Rev. D*, 62:064015, 2000.

[79] F. Acernese et al. The status of coalescing binaries search code in Virgo, and the analysis of C5 data. *Class. Quant. Grav.*, 23:S187–S196, 2006. doi: 10.1088/0264-9381/23/8/S24.

[80] B. Abbott et al. Beating the spin-down limit on gravitational wave emission from the Crab pulsar. *Astrophys. J.*, 683:L45–L50, 2008. doi: 10.1086/591526.

[81] LIGO Scientific Collaboration and K Hurley. Implications for the origin of grb 070201 from ligo observations. *Astroph. Journal*, 681:1419–1430, 2008.

[82] M. Cavaglia, M. Hendry, D. Ingram, S. Milde, S. R. Pandian, D. Reitze, K. Riles, B. Schutz, A. L. Stuver, T. Summerscales, D. Ugolini, J. Thacker, M. Vallisneri, and A. Zermeno. Gravitational Wave Astronomy: Opening a New Window on the Universe for Students, Educators and the Public. In *Bulletin of the American Astronomical Society*, volume 40 of *Bulletin of the American Astronomical Society*, page 231, May 2008.

[83] M. Cavaglia, M. Hendry, S. Marka, D. Reitze, and K. Riles. Astronomy's New Messengers: A traveling exhibit to reach out to a young adult audience.

[84] Royal society summer science exhibition website. URL `www.summerscience.org.uk`.

[85] Einstein@home website. URL `einstein.phys.uwm.edu`.

[86] Cubase advanced music production system. URL `www.steinberg.net/en/products/musicproduction/cubase5`.

[87] Linux multimedia studio. URL `lmms.sourceforge.net`.

[88] Audacity. URL `audacity.sourceforge.net/download/linux`.

[89] Hazel Muir. Online game makes anyone a 'black hole hunter'. *New Scientist Blog*, 2008. URL `www.newscientist.com/blog/space/2008/06/online-game-makes-anyone-black-hole_30.html`.